Project 059(B) Jet Noise Modeling and Measurements to Support Reduced LTO Noise of Supersonic Aircraft Technology Development

Georgia Institute of Technology/Gulfstream Aerospace Corporation

Project Lead Investigator

Krishan K. Ahuja
Regents Professor
School of Aerospace Engineering
Georgia Institute of Technology
Atlanta, GA 30342
404-290-9873
Krish.Ahuja@ae.gatech.edu

University Participants

Georgia Institute of Technology (Georgia Tech)

- PI: Krishan K. Ahuja, Regents Professor
- FAA Award Number: 13-C-AJFE-GIT-060
- Period of Performance: June 5, 2020, to September 30, 2025
- Tasks:
  1. Consult with the Advisory Panel
  2. Define Nozzle Requirements and Design Tests
  3. Design and Fabricate a Baseline Nozzle
  4. Test Setup and Experimental Data Acquisition
  5. Data Dissemination
  6. Proposal for a Follow-on Efforts
  7. Reporting and Data Dissemination

Project Funding Level

This project received $750,000 from the Federal Aviation Administration (FAA) and $750,000 cost-sharing from Gulfstream Aerospace Corporation (GAC) for each of the three phases of this project. Total combined funding to date is $1.5M.

Investigation Team

Georgia Institute of Technology

Dr. Krishan Ahuja, PI, Georgia Tech
Dr. Jimmy Tai (Co-PI), Georgia Tech
Dr. Nicholas Breen, Co-Investigator and Lead Experimentalist, Georgia Tech Research Institute (GTRI)
Dr. Robert Funk, Experimentalist, GTRI
Jackson Larisch, Graduate Research Assistant, GTRI
David N. Ramsey, Graduate Research Assistant for portion of the program and subsequently a NSF Fellow working on fundamental issues related to the current project, Georgia Tech and since graduated, GTRI
Reagan Mayo, Graduate Research Assistant for portion of the program and since graduated, GTRI

Gulfstream Aerospace Corporation

Brian Cook (Gulfstream)

- Dr. Joseph Gavin (Gulfstream)

Project Overview

The overall goal of this project is to perform cost-effective supersonic transport (SST) jet noise research/technology experiments to enable low-, medium-, and high-fidelity jet noise prediction methods. The specific objective is to design the experiments in collaboration with industry, the National Aeronautics and Space Administration (NASA), Department of Defense (DOD), FAA, and modelers funded by the FAA to help develop improved jet noise prediction methods with reduced uncertainty and enable industry to design quieter supersonic jet engines with higher confidence regarding the noise that will be generated. In collaboration with GAC, Georgia Tech's industry partner on this project, a representative baseline nozzle design was selected for experiments at Georgia Tech. The data acquired consisted of far-field noise, high-speed flow visualization, source location, and detailed mean and unsteady flow measurements.

The experimental data acquired by Georgia Tech was provided to key stakeholders and other computational teams funded by FAA to validate their computational simulations to confirm that jet noise predictions using semi-empirical and computational modeling approaches can be reliably used for jet noise evaluation.

Task Objectives

This project had seven tasks, as listed below. These task titles are self-descriptive; however, a short objective statement and/or a summary of accomplishments are also provided for each task.

Task 1: Consult with the Advisory Panel
The objective of this task was to receive regular feedback from industry and NASA subject-matter experts (SME) in supersonic jet noise.

Task 2: Define Nozzle Requirements and Design Tests
The objective of this task was to define the nozzle requirements and design the experiments.

Task 3: Design and Fabricate a Baseline Nozzle
The objective of this task was to design and fabricate a baseline nozzle that meets the requirements defined in Task 2 above and is also suitable for the tests needed to meet the objectives of the overall program.

Task 4: Test Setup and Experimental Data Acquisition
The objective of this task was to get ready to conduct the tests and acquire and analyze the data

Task 5: Data Dissemination
The objective of this task is to stay in touch with the modelers being funded by FAA under ASCENT Project 059 and provide the project stakeholders with the nozzle design and both acoustic and flow data from the current project. The final model design has been shared with the modeling teams since November 2021. All Year 1 and 2 acoustic and particle imaging velocimetry (PIV) data, both for the unheated and heated-core conditions, have been shared with the modelers. Likewise, the flow visualization has been made available to the modelers.

Task 6: Proposal for a Follow-on Efforts
Each year a proposal for the following year was submitted and approved.

Task 7: Reporting and Data Dissemination
All Year 1-3 reports (annual and quarterly) were submitted on time.

Research Approach and Accomplishments

This project can be divided into two main parts: Years 1 & 2 were dedicated to studying the so-called Academic Nozzle (described below) and Year 3 was devoted to investigating the so-called Gulfstream® nozzle. The academic nozzle is a design created by the Georgia Tech Aerospace Systems Design Lab (ASDL) and the Gulfstream nozzle, like its namesake, is a design created by GAC. For both of these nozzles, various types of data were collected at a wide range of operating

® Gulfstream is a registered trademark of Gulfstream Aerospace Corporation, Savannah, Georgia

conditions and extraction ratios: acoustic spectra, flow data, PIV, flow visualization, and acoustic source locations. All of this data has been provided to aeroacoustics modelers for additional analysis and model development.

This report is divided into two large sections, each detailing the results for each of the two main parts of the effort described above.

Years 1 & 2 - the Academic Nozzle

Georgia Institute of Technology

Nozzle Design

The design of the baseline nozzle is shown in Figure 1. The baseline nozzle and tests were based on a paper engine design created by the Georgia Tech ASDL guided by ASCENT Project 010 on engine cycle selection for the Georgia Tech Medium SST jet (55 passenger class). For simplicity, it was decided that the Georgia Tech nozzle model tested under this project would not have a plug. For the purpose of calculating the area of the outer (secondary flow) duct, the annular areas of the paper engine were used to calculate the area of the secondary flow duct in GTRI's model nozzle facility. The GTRI model is a 0.045 scale of the paper engine. The model consists of the following parts: (1) the primary nozzle with the collar to avoid any anomalous flow effects due to any geometrical protrusions/recesses; (2) the secondary nozzle; (3) mixer ducts; and (4) the exhaust nozzle. A total of three mixer ducts were fabricated to allow for different mixing-duct length-to-nozzle-exit diameter ratios (L/D). The test model utilizes the coannular flow capabilities of the GTRI jet facilities. The primary and secondary flow streams converge into the mixer-duct and exhaust nozzle combination. The mixer-duct and exhaust nozzle combinations allow for four values of L/Ds, namely, 0.7 (exhaust nozzle mounted directly to the secondary nozzle), 1, 2, and 3. The jet stream is ultimately formed by the exhaust nozzle, which is a converging nozzle with geometry based on the converging section of the converging-diverging nozzle from the ASDL engine design.

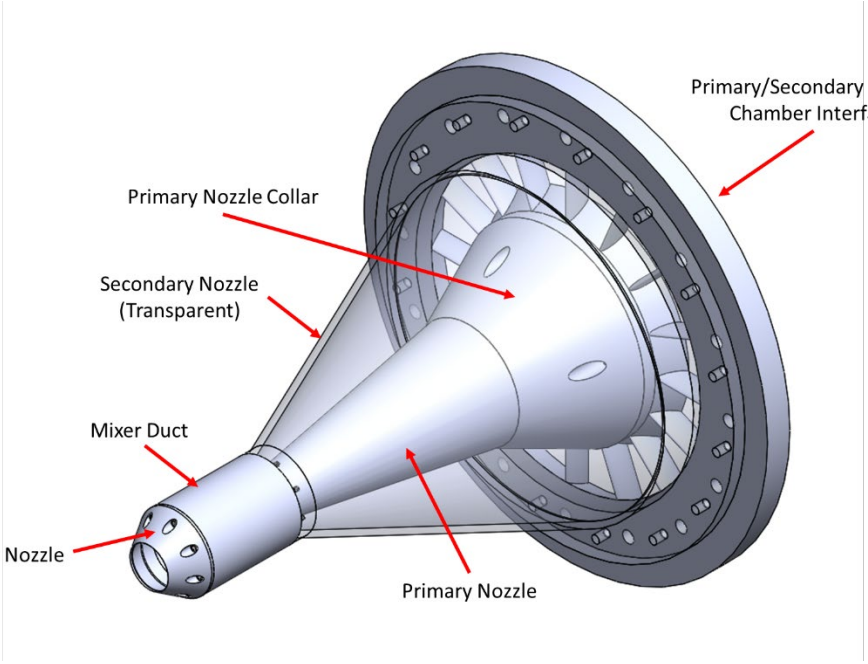

Figure 1. Year-1 experimental model design.

Acoustic Measurements

Facility Set-up and Testing Description

The test model was mounted in the GTRI Anechoic Jet-Facility for the acoustic data acquisition as seen in Figure 2. This facility is described in detail in Burrin et al. (1974), Burrin and Tanna (1979), and Ahuja (2003). Farfield microphones were

mounted on a polar arc at angles between 30° and 120° with respect to the jet axis in 10° increments. The upstream jet operating conditions were set by controlling the ratio of the total pressure to the ambient pressure (PR = p_t/p_a) for both the primary and secondary streams. The pressure ratios of both the primary and secondary streams varied between 1.12 and 1.89. The extraction ratio (ER = p_{t2}/p_{t1}) was also used as another parameter to define the secondary pressure ratio for a given primary stream pressure. This parameter was brought to our attention by the program partners and is of practical importance. Per insight from GAC and FAA, ERs between 1.00 and 1.07 are the most realistic conditions for a given PR_1. Additionally, the primary jet was operated under both unheated and heated conditions. In the unheated tests, the jet total temperature varied between 60°F and 70°F. For the heated testing, it was set nominally to 500°F. As a note, for the remainder of this program the pressure ratio, PR, will refer to the ratio between upstream total and ambient pressures. In addition to the acoustic measurements, the primary and secondary total pressure and temperature, the primary and secondary mass flow rates (measured at the control valve), and the ambient pressure, temperature, and relative humidity were measured.

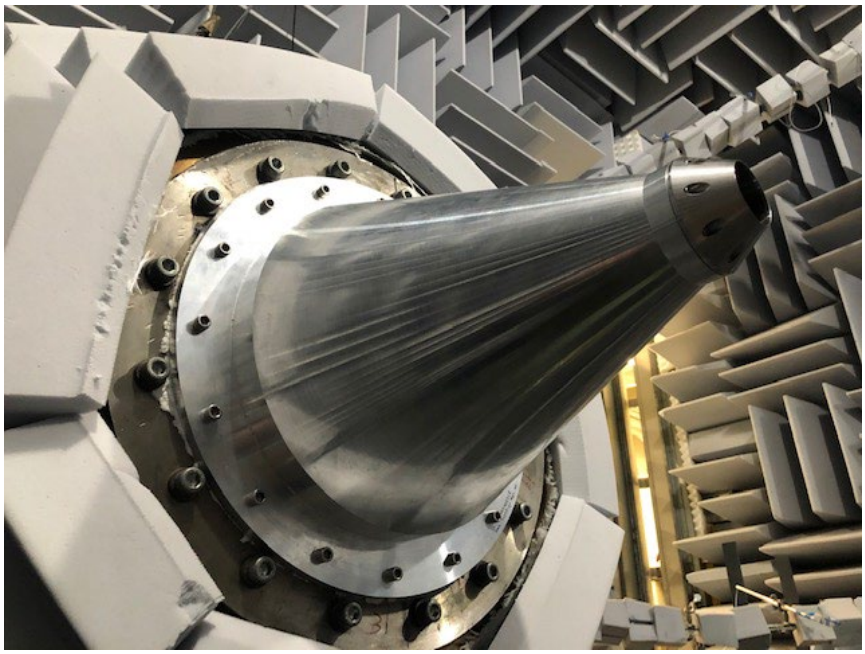

Figure 2. Project model set up in the GTRI Anechoic Jet Facility.

The microphones used for these measurements were Bruel and Kjaer (B&K) 4939 ¼-in. free-field microphones and were attached to B&K 2669 preamplifiers. The microphone-preamplifier combinations were connected to B&K 2960-A-0S4 Nexus conditioning amplifiers that, in addition to amplifying the signal, acted as the microphones' 200 mV power supply. The microphone signals were sampled at 204.8 kHz using National Instruments® PXIe-4499 modules. The acoustic pressure time histories were then processed into averaged sound pressure level (SPL) spectra using a window size of 6400 samples, 50% overlap, and a Hanning window. To render the data to lossless form for use by the modelers, the following corrections were applied to these SPL spectra: free-field response correction, windsock correction (if necessary), atmospheric attenuation, and distance. These corrections are described in detail in Karon and Ahuja (2016).

Acoustic Analysis

The following subsections detail the results acquired from acoustic measurements obtained using the baseline nozzle across a variety of operating conditions (including heated and unheated core flow) and mixing duct lengths. This analysis is categorized by the effects of extraction ratio, mixing-duct length, and core temperature. An additional analysis of noise produced by the dual-stream nozzle at extraction ratios of unity and just above unity – which are of most interest to the FAA and GAC – is provided. Much of the discussion here is expanded upon by Ramsey et. al. (2022a). The howling

® National Instruments is a registered trademark of National Instruments Corporation, Austin, Texas.

produced by this nozzle geometry at certain operating conditions is briefly discussed with references to more detailed published work.

Effect of changing the Extraction Ratio: Figure 3 shows the jet noise measurements for jet condition of ER = 1.1, 1.0, and 0.92 for the L_e/D_e = 0.7 configuration. It is noted that the ER = 1.1 and 0.92 are outside of the ER range advised to be of greater practical interest by the program partners, but the data is shown here because it was acquired as part of this program and validating the predictions by the modelers for these conditions would provide added confidence in their fidelity. As can be seen in Figure 3, the noise increases with increasing secondary pressure ratio. At lower frequencies (below ~3 kHz), the noise increased by about 1 dB as the secondary pressure ratio increases from 1.28 to 1.39 and from 1.39 to 1.52. At the higher frequencies, the noise increase is larger. As the secondary pressure ratio is increased from 1.28 to 1.39, the noise increases by as much as 3 dB, and when the secondary pressure ratio is increased from 1.39 to 1.52, the noise increases by as much as 5 dB. It will be shown later that if the extraction ratios are maintained close to unity, say up to 1.07, there is no noticeable change in SPLs at low frequencies and there is very little change at high frequencies.

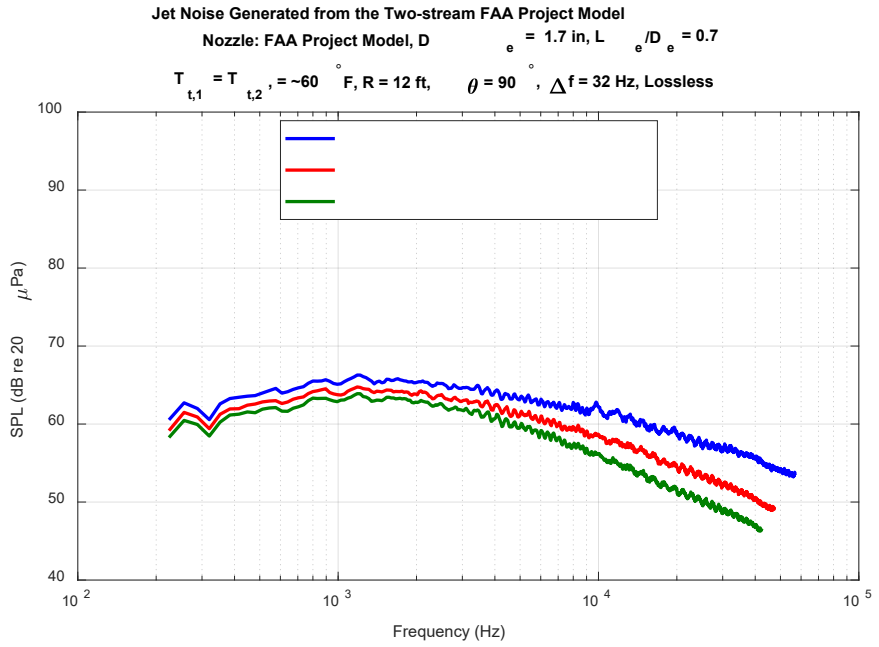

Figure 3. Typical jet noise spectra at extraction ratios of 1 and above and below 1 for the Le/De = 0.7 configuration. FAA: Federal Aviation Administration, SPL: sound pressure level.

Effect of increasing the mixing-duct length: Figure 4 shows the jet noise generated from the test model with primary and secondary pressure ratios both equal to 1.39 (ER = 1.0) with L_e/D_e varied between 0.7 and 3.0. As seen in the Figure 4, at frequencies below 7 kHz, the noise for the three conditions is the same. Above 7 kHz, there is a minor reduction in jet noise, of 1 dB at most. This indicates that increase in mixing-duct length does increase the mixing to a small degree, leading to reduced noise at high-frequencies.

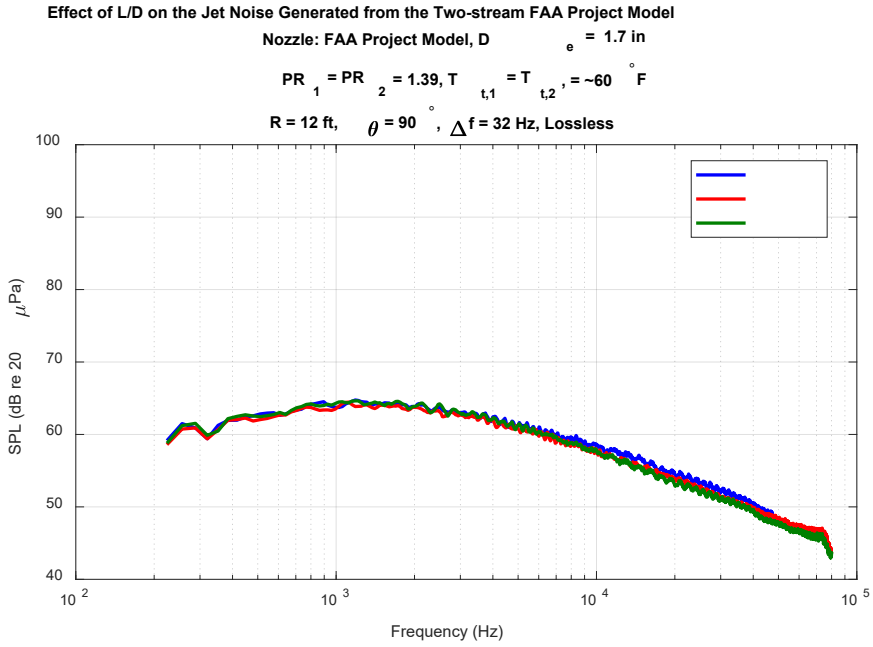

Figure 4. The effect of mixing-duct length on the jet noise produced by the test model. FAA: Federal Aviation Administration, SPL: sound pressure level.

Effect of increasing the primary jet temperature: Figure 5 shows the effect of increasing the primary nozzle total temperature for L_e/D_e of 0.7. The corresponding data for L_e/D_e of 3 appears in Figure 6. The unheated spectrum in both cases seems unaltered, but the spectrum for the larger L_e/D_e with the heated primary stream has somewhat lower SPLs at higher frequencies. For example, at a frequency of 50,000 Hz, the SPL for L_e/D_e = 0.7 is 51 dB and for L_e/D_e = 3, it is 47.4 dB. It may be an effect of reduced speed of the heated stream via mixing with the unheated secondary jet in the longer duct.

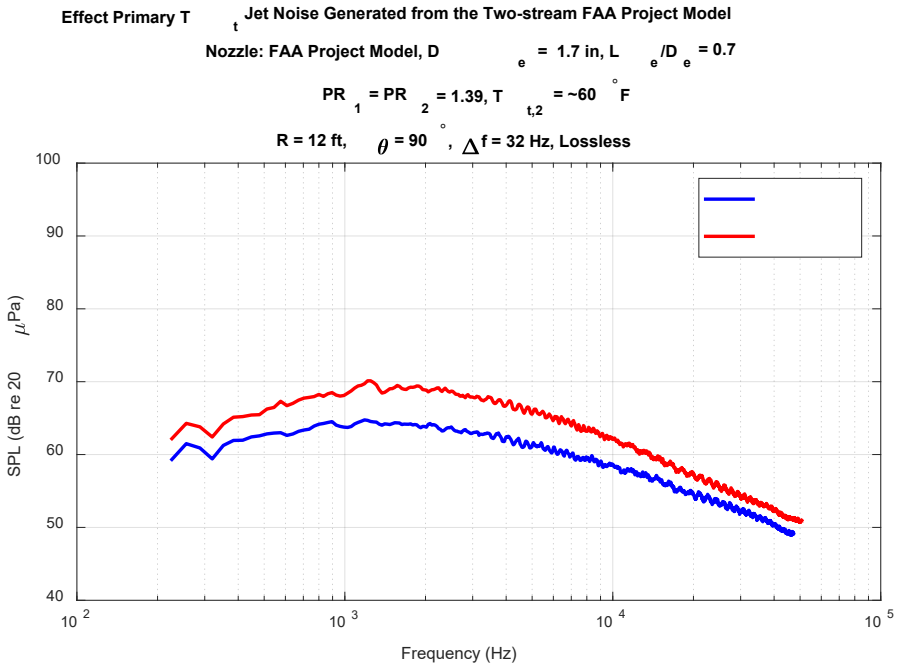

Figure 5. Effect of primary total temperature with the Le/De = 0.7 configuration. FAA: Federal Aviation Administration, SPL: sound pressure level.

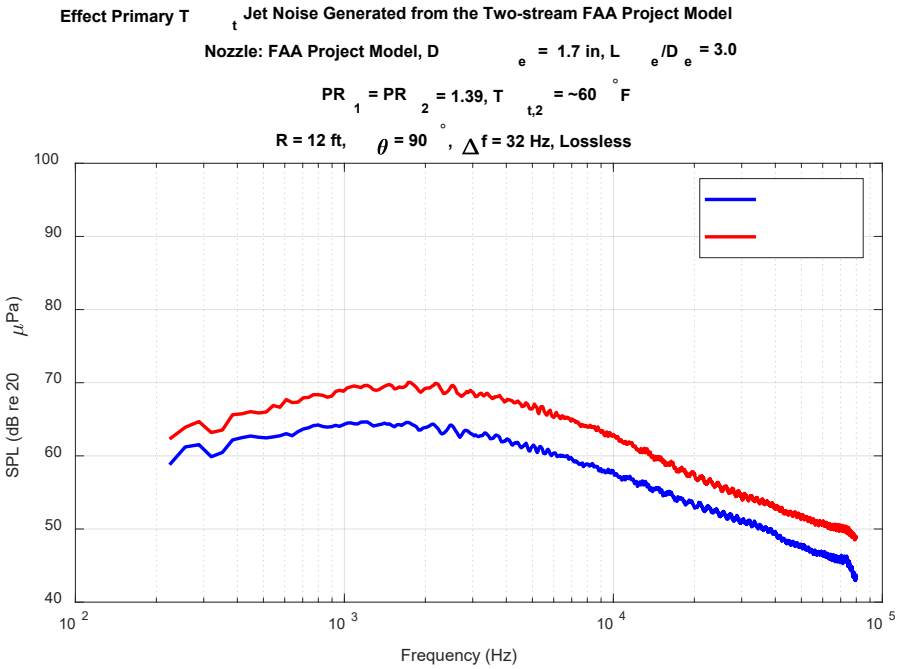

Figure 6. Effect of primary total temperature with the L_e/D_e = 3.0 configuration. FAA: Federal Aviation Administration, SPL: sound pressure level.

Detailed Analysis of Data at Extraction Ratios between 1 and 1.07: As mentioned above, FAA and GAC indicated that for mixed flow engines the extraction ratio between 1.00 and 1.07 are the most realistic. Acoustic measurements that focus on this extraction ratio range are presented here. Figure 7 shows the results of the small variations of extraction ratio for a PR_1 = 1.39. Figure 7 shows the results as the extraction ratio varies in 0.01 steps from 1.00 to 1.07 at a polar angle of 90°. Figure 7 also shows cases of L_e/D_e of 0.7 and 3.0 as well as cases of unheated core flow and the core flow heated to 500°F. Comparing Figures 7a and 7b as well as Figures 7c and 7d gives some insight into the effect of the heating the core flow. There are two main effects of heating the core flow: (1) the overall noise levels increase, which is a result of higher jet velocities in the case of the heated-core flow, and (2) the jet noise spectra show greater collapse across extraction ratios. To illustrate the first effect, for both L_e/D_e = 0.7 and 3.0 cases, as expected, the peak noise increases (by about 5 dB) as the core flow is heated to 500°F. This can be seen on comparing the spectra in Figures 7a and 7b for L_e/D_e = 0.7 and Figures 7c and 7d for L_e/D_e = 3.0. To illustrate the second effect (i.e., the effect of extraction ratio), for both L_e/D_e = 0.7 and 3.0 cases, for the unheated case, the change of extraction ratio has a minimal effect at low-frequencies and is of the order of 1 dB, but this spread increases to 5 dB at high-frequencies. This can be seen on comparing the spectra in Figure 7a and 7c for L_e/D_e = 0.7 for the unheated-core cases and Figure 7b and 7d for the heated-core cases. For the heated-core case, the spectra collapse below 8 kHz, and above 8 kHz all SPLs are within 2 dB. As a note, for the L_e/D_e = 3.0 case, the heated core flow shows very minimal variation in spectral levels. Observing the effect of the mixing duct length, for the unheated case, the spectral levels spread is reduced from a maximum of 5 dB for L_e/D_e = 0.7 to 3 dB for L_e/D_e = 3. For the heated core flow case, the spectral level spread does not change much as L_e/D_e = 0.7 is changed L_e/D_e = 3.0.

Ideally this analysis should be done by normalizing the SPLs and the frequency scales. Unfortunately, the normalizing parameters were not available at the time of this analysis.

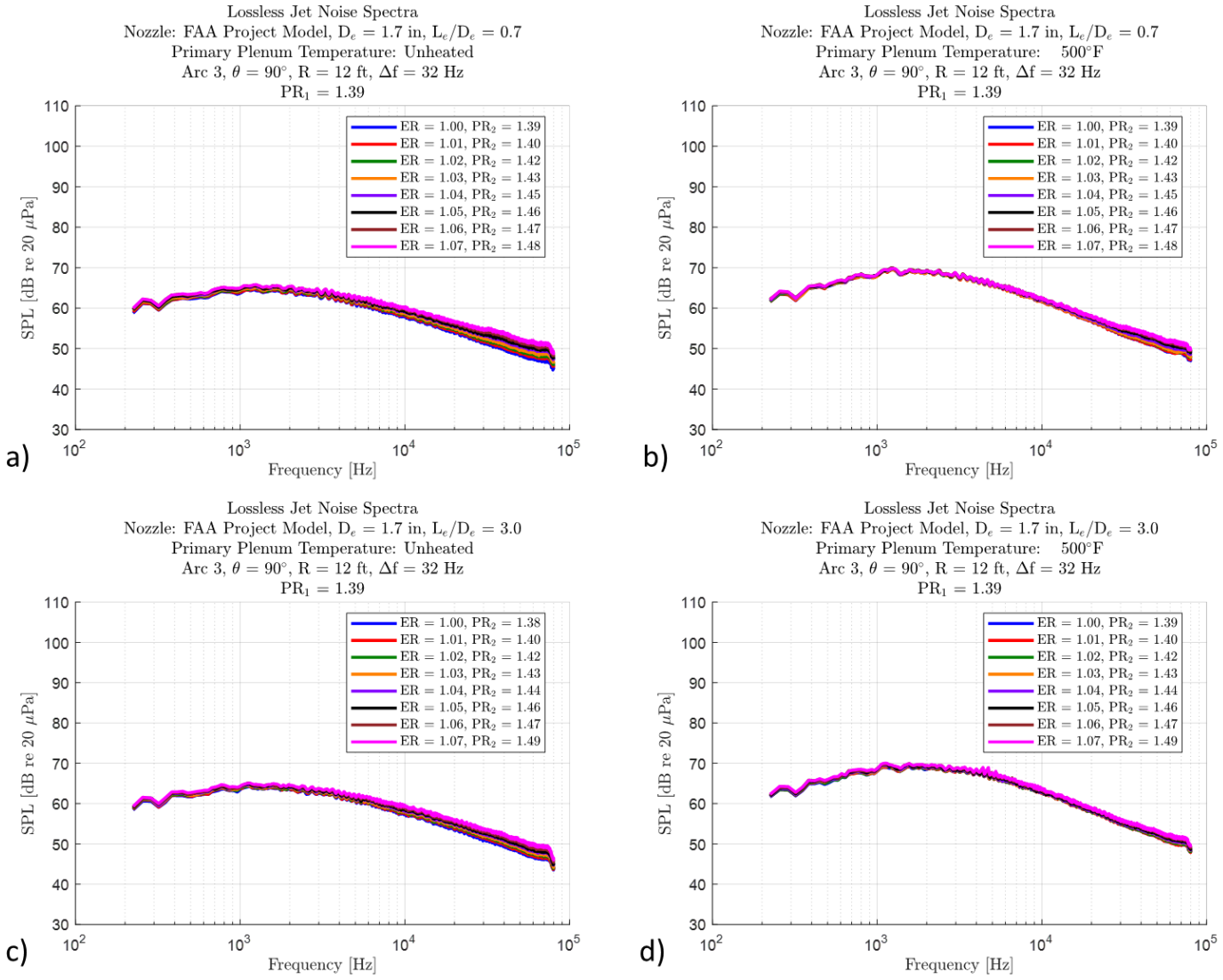

Figure 7. Example acoustic measurements for the small extraction ratio changes for PR1 = 1.39 at θ = 90°. (a) L_e/D_e = 0.7 and core flow unheated, (b) L_e/D_e = 0.7 and core flow heated to 500°F, (c) L_e/D_e = 3.0 and core flow unheated, and (d) L_e/D_e = 3.0 and core flow heated to 500°F. FAA: Federal Aviation Administration, SPL: sound pressure level.

Howling in an Internally Mixed Confluent Nozzle: At certain operating conditions high-intensity tones were observed in the jet noise measurements using the Year 1 baseline nozzle. The first set of operating conditions for which tones were observed were those with very low (well below unity) extraction ratios. The second set of operating conditions were those with high subsonic secondary-stream Mach numbers. Figure 8 shows the resulting tones created at these operating conditions and their effects on noise relative to an unheated, unity extraction ratio dual-stream jet, which is shown in red. It is seen that these tones are as much as 30 dB higher than the broadband jet noise for the same core jet operating pressure ratio (1.39 in this case) irrespective of whether the extraction ratio is below unity (the blue curve) or higher than unity (the green curve).

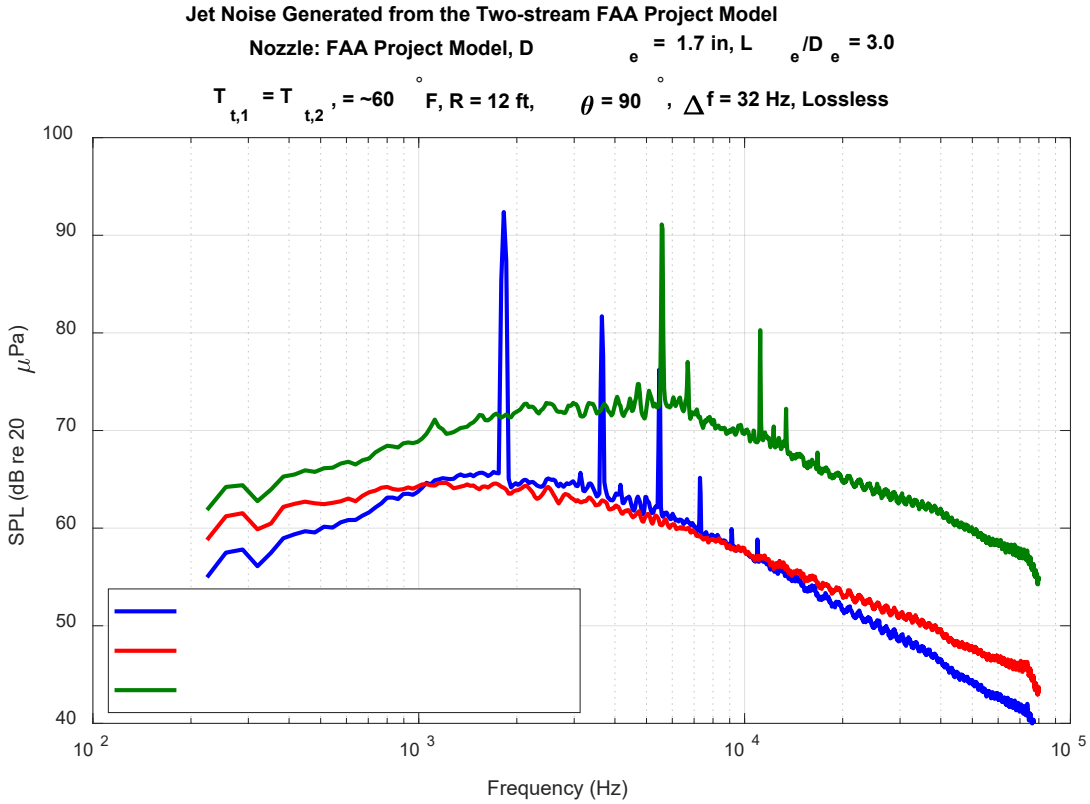

Figure 8. Jet noise measurements with pressure splits far from unity for the L_e/D_e = 3.0 configuration. FAA: Federal Aviation Administration, SPL: sound pressure level.

Extensive work (Ramsey et al., 2022b; Ramsey et al., 2023a; Ramsey et al., 2023b; Ramsey, 2024) has gone into understanding the mechanisms responsible for this howling, its impact on jet noise amplification and other related measurements, and methods to eliminate it. It was found that two distinct mechanisms were responsible for the howling. One of them, which occurs at low extraction ratios, is related to the impingement of the core jet shear layer on the exhaust nozzle lip (Ramsey et al., 2023a). The other, which occurs at high subsonic secondary Mach numbers, is related to periodic separation of the boundary layer near the exhaust nozzle exit as a result of an unsteady shockwave/boundary-layer interaction (Ramsey et al., 2023b). It was found that for either case, the feedback mechanism responsible can be weakened and the howling removed by using a suitably placed boundary layer trip. Figure 9 shows a boundary layer trip fashioned out of lock wire installed just upstream of the lip of the final exhaust nozzle, and the effect of this trip on the howling is demonstrated in Figure 10 showing the elimination of high-intensity tones and any broadband amplification.

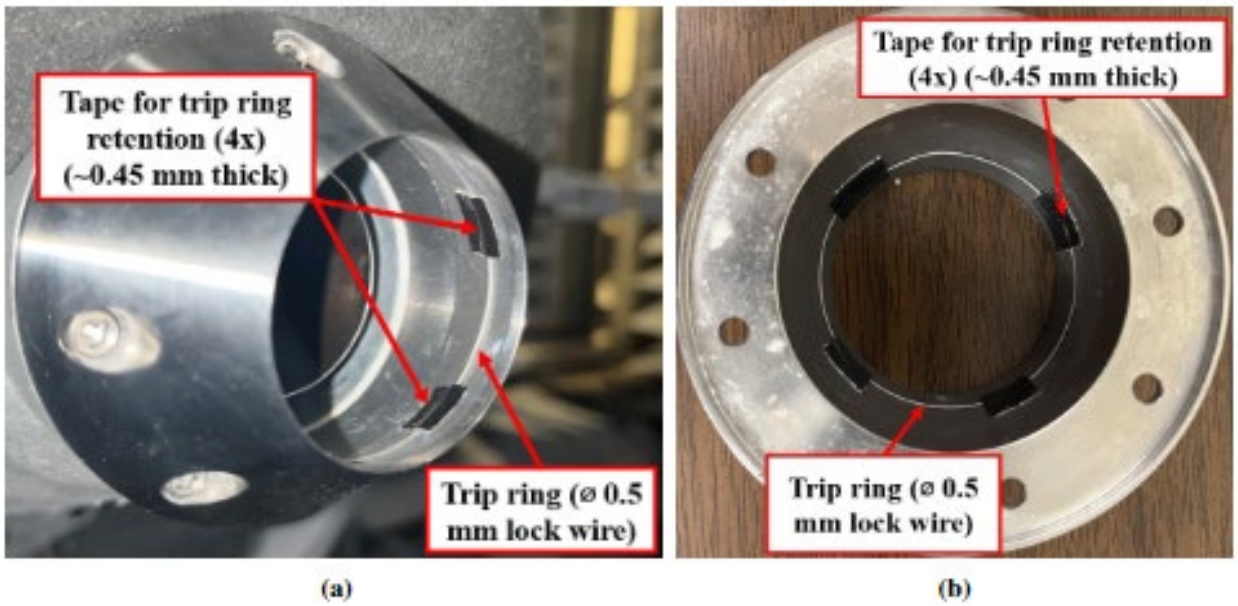

Figure 9. Boundary layer trip configurations: (a) view from exit and (b) view from upstream.

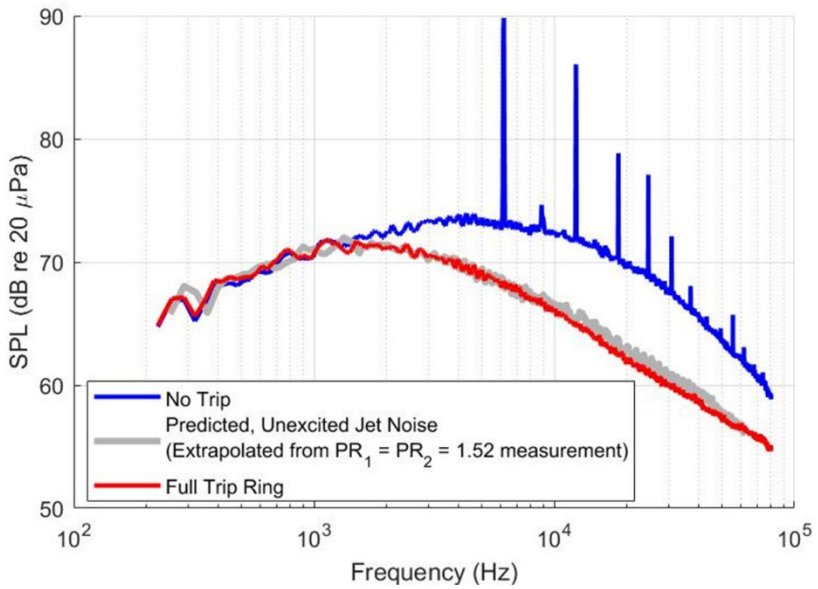

Figure 10. Effect of the boundary layer trip ring on the noise from a confluent nozzle. FAA Project Model, De = 1.7 in. and Le/De = 0.7. PR1 = 1.69, ER = 1.0, unheated, R = 12 ft, θ = 90°, Δf = 32 Hz, lossless. SPL: sound pressure level.

Effect of Tabs on the Noise Produced by the Confluent Nozzle: Before acquisition of more complex, lobed internal mixers from GAC as part of the Year 3 effort, a study was performed to determine the effects of using mechanical tabs, that are known to increase jet mixing, installed within the core nozzle as a simple forced mixer design. For this, two types of tab designs were used: (1) the smaller D-tabs shown in Figure 11a and the larger, and (2) the triangular delta tabs shown in Figure 11b. Figure 12 details how these tabs were installed within the core nozzle. Various configurations of the confluent nozzle equipped with tabs were tested. While a wide range of conditions were tested, the following results are presented

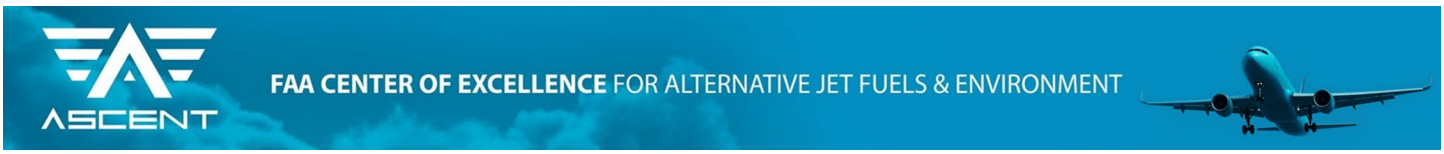

as typical results: PR_1 = 1.39 and ER = 1.0 and PR_1 = 1.39 and ER = 1.07. The tabs were tested with the confluent nozzle in both L_e/D_e = 0.7 and 3.0 configurations. It was observed during testing that the use of mechanical tabs – no matter how many – did not eliminate the howling. However, it is again noted that the howling can be eliminated through use of a simple boundary layer trip.

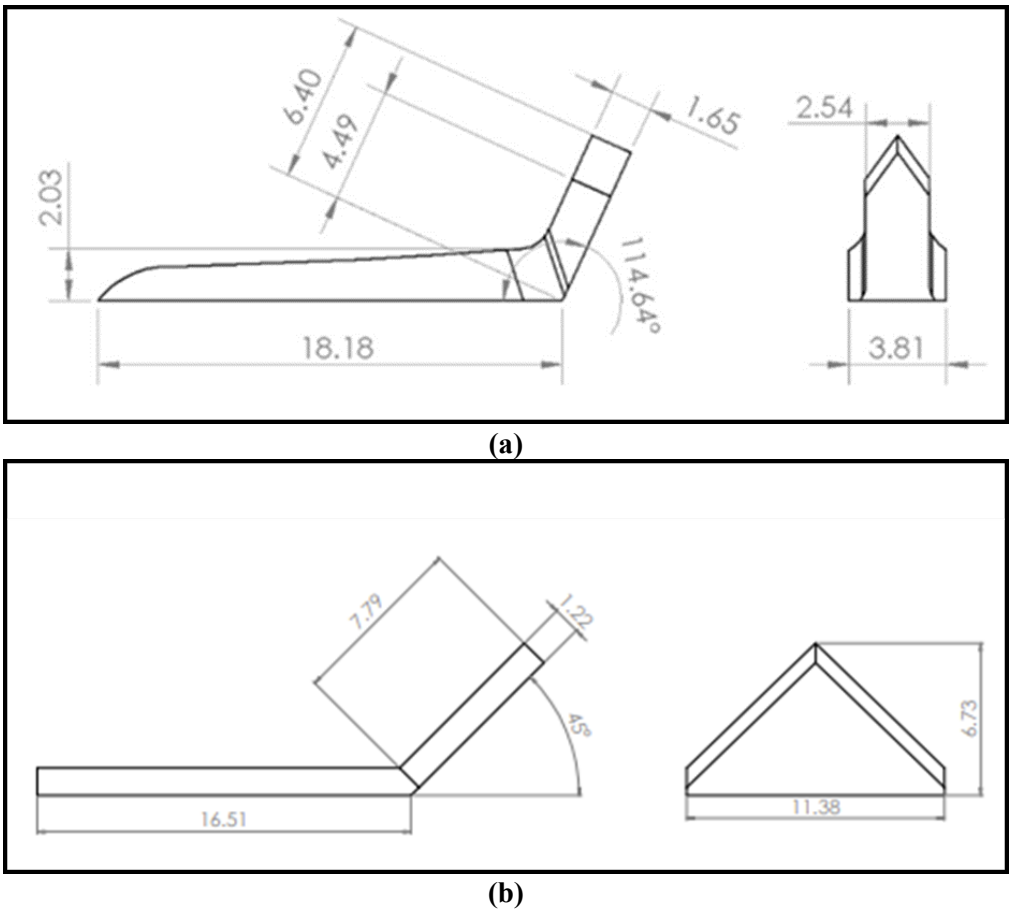

Figure 11. Design of the (a) D-tab and (b) delta tab (dimensions in mm).

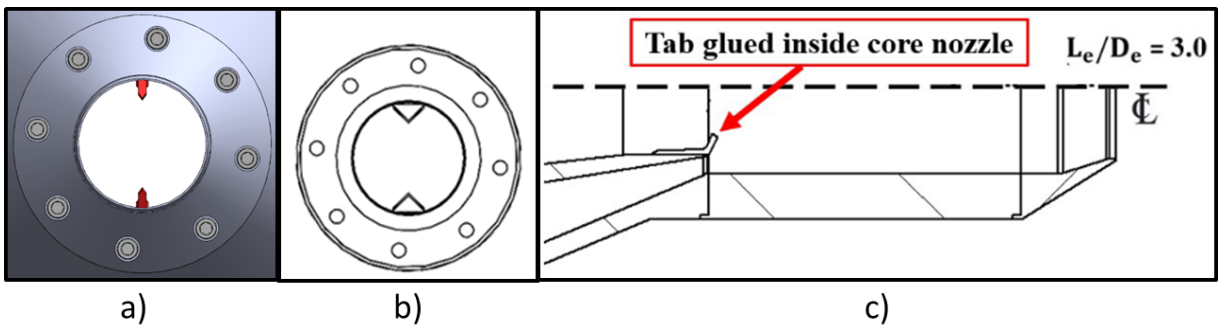

Figure 12. Tabs in the core nozzle: (a) D-tabs, (b) delta tabs, and (c) cross-sectional view of nozzle showing tab position.

Figures 13 and 14 show the effect on the jet noise produced by adding D-tabs to the core nozzle at the PR_1 = 1.39 and ER = 1.0, for mixing-duct lengths L_e/D_e = 0.7 and 3.0, respectively. As shown in Figures 13, the L_e/D_e = 0.7, no tab configuration has no appreciable effect on the noise. Similarly, as shown in Figure 14, for the L_e/D_e = 3.0, tabs irrespective of the number of tabs used, had no appreciable effect at low frequencies (the left of the spectral peak), but increasing the tab number to four and then to eight seems to increase the noise at higher frequencies. In particular, the noise at high frequencies is elevated by a maximum of 2 dB. These level increases begin at 20 kHz for the 4-tab case and at 7 kHz for the 8-tab case.

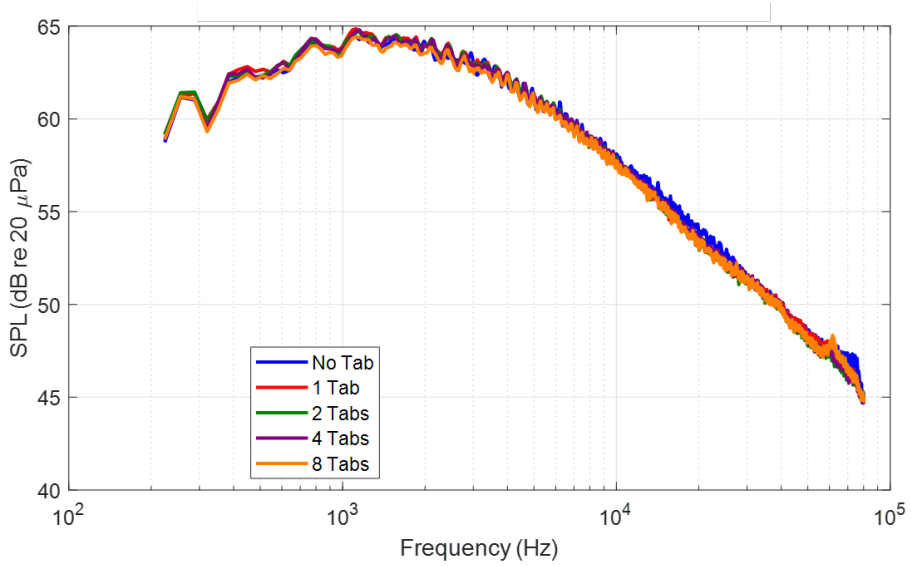

Figure 13. Effect of D-tabs on the noise from a confluent nozzle. FAA Project Model, D_e = 1.7 in. and L_e/D_e = 0.7. PR_1 = 1.39, ER = 1.0, unheated, R = 12 ft, θ = 90°, Δf = 32 Hz, lossless. SPL: sound pressure level.

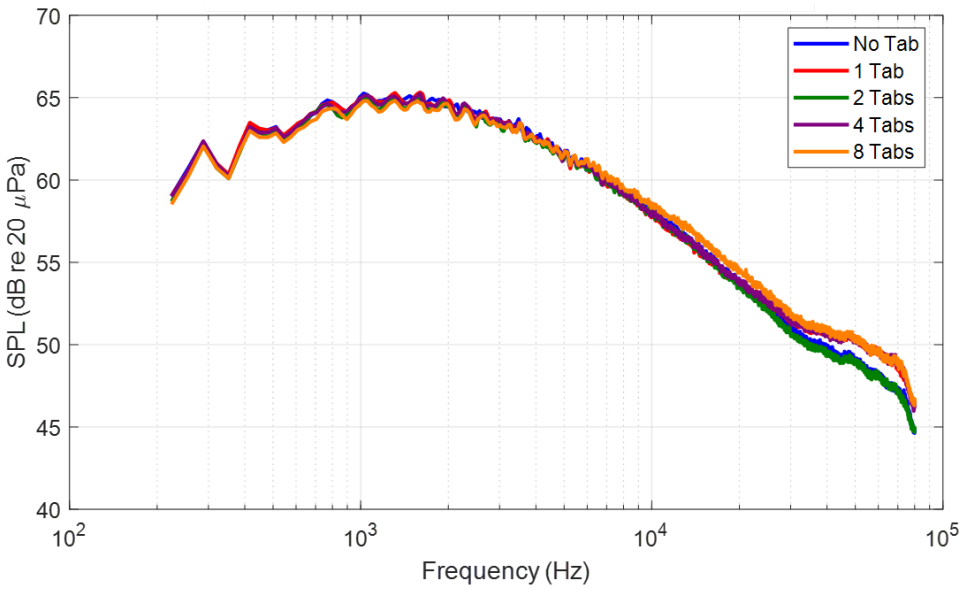

Figure 14. Effect of D-tabs on the noise from a confluent nozzle. FAA Project Model, D_e = 1.7 in. and L_e/D_e = 3.0. PR_1 = 1.39, ER = 1.0, unheated, R = 12 ft, θ = 90°, Δf = 32 Hz, lossless. SPL: sound pressure level.

The results shown in the last two figures were for an extraction ratio of unity. Figures 15 and 16 show the effect of the D-tabs on the noise produced by the confluent nozzle for PR_1 = 1.39 and ER =1.07 for L_e/D_e = 0.7 and 3.0 respectively. For both mixing duct lengths, the tabs do not seem to make substantial difference. The exception to this is the 1- and 2-tab configurations which generate a high-frequency tone for L_e/D_e = 0.7.

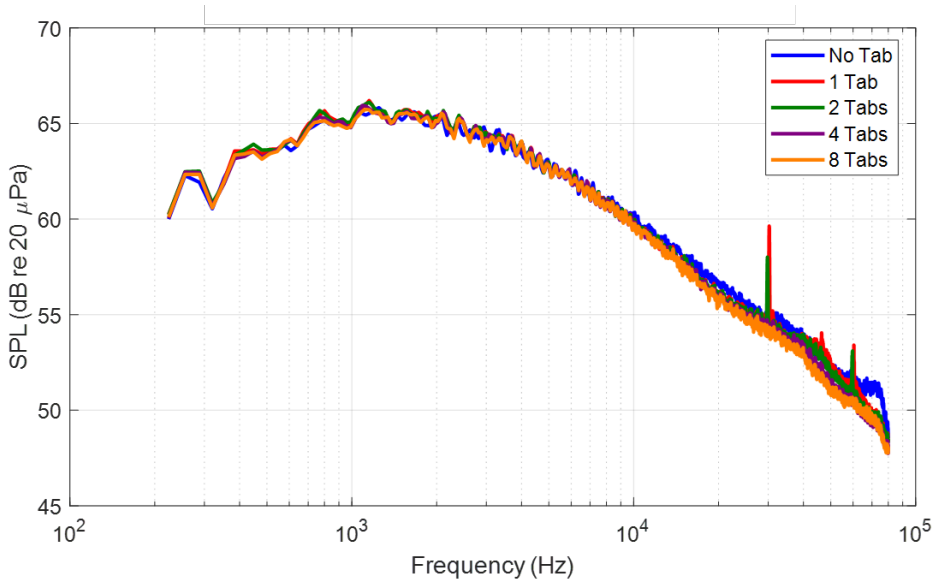

Figure 15. Effect of D-tabs on the noise from a confluent nozzle. FAA Project Model, De = 1.7 in. and Le/De = 0.7. PR1 = 1.39, ER = 1.07, unheated, R = 12 ft, θ = 90°, Δf = 32 Hz, lossless. SPL: sound pressure level.

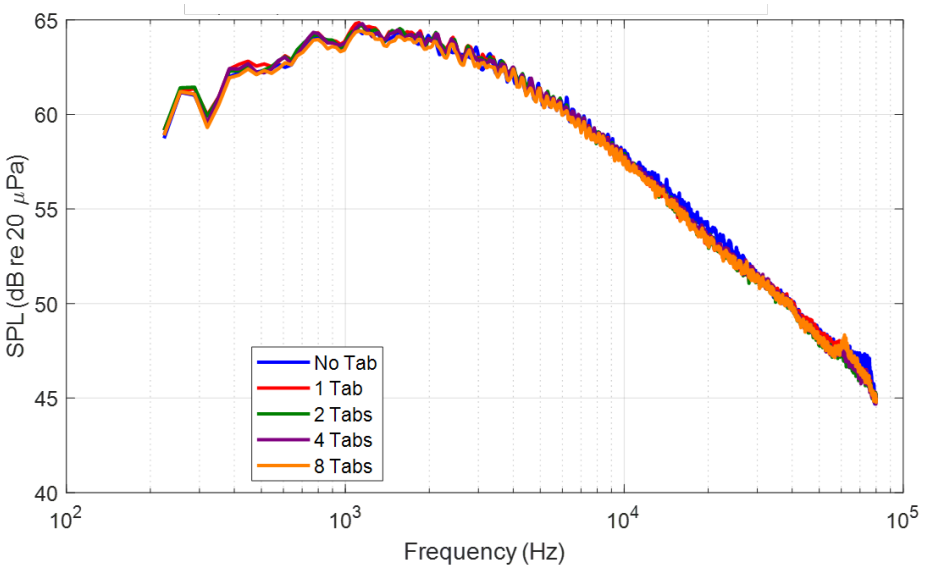

Figure 16. Effect of D-tabs on the noise from a confluent nozzle. FAA Project Model, De = 1.7 in. and Le/De = 3.0. PR1 = 1.39, ER = 1.07, unheated, R = 12 ft, θ = 90°, Δf = 32 Hz, lossless. SPL: sound pressure level.

The results shown indicate that for an internally mixed, dual-stream jet with an unheated core stream and near-unity extraction ratio, the use of tabs has little to no appreciable effect on the farfield noise. This same lack of effect is observed for the larger delta tabs as well and is also true even when using a lobed mixer nozzle as will be demonstrated later. When operating near unity extraction ratio with an unheated core stream, the core and bypass streams are nearly uniform, and there is little to no opportunity for any internal mixing which would otherwise change the farfield noise. In order for the tabs to create any appreciable change in the noise there must be a substantial difference in the two streams, either by operating at highly unrealistic extraction ratios or by heating the core stream. Figures 17 and Figure 18 show the effect of using two delta tabs on the jet noise spectra at PR_1 = 1.39, ER = 1.0, with a heated core flow ($T_{t,1} \approx 500°F$) at polar angles of 30° and 90°, respectively. The different colored curves denote acoustic measurements taken along polar arcs at different azimuths with respect to the installation of the tabs. As shown in Figures 17, at low polar observation angles the tabs reduce the level of peak jet noise by about 3 dB. Above about 6 kHz the tabs increase the noise by as much as 4 dB. A decrease in the level of peak jet noise at lower frequencies with an associated increase in higher frequency noise is typical of enhanced-mixing devices including lobed mixers (Mengle et al., 1997). Figure 19 shows the effect of the delta tabs across all polar angles and azimuths by showing the overall sound pressure level (OASPL). The dashed black line indicates noise measurements taken without the use of tabs to serve as a baseline. It is observed that the OASPLs decrease at lower polar observation angles where lower frequency noise is dominant and they increase at greater observation angles where lower frequency noise is less dominant.

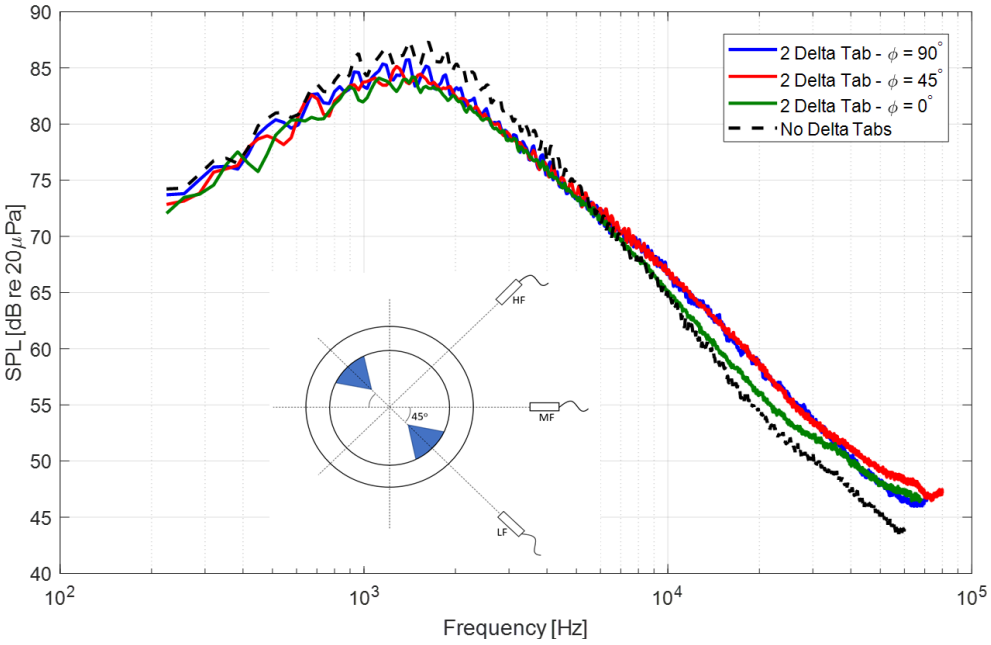

Figure 17. Effect of delta tabs on the noise from the confluent nozzle. De =1.7 in, Le/De = 0.7. PR1 = 1.39, ER = 1.00, Tt,1 = 500°F, Tt,2 = 60°F, R = 12 ft, θ = 30°, Δf = 32 Hz, lossless. SPL: sound pressure level.

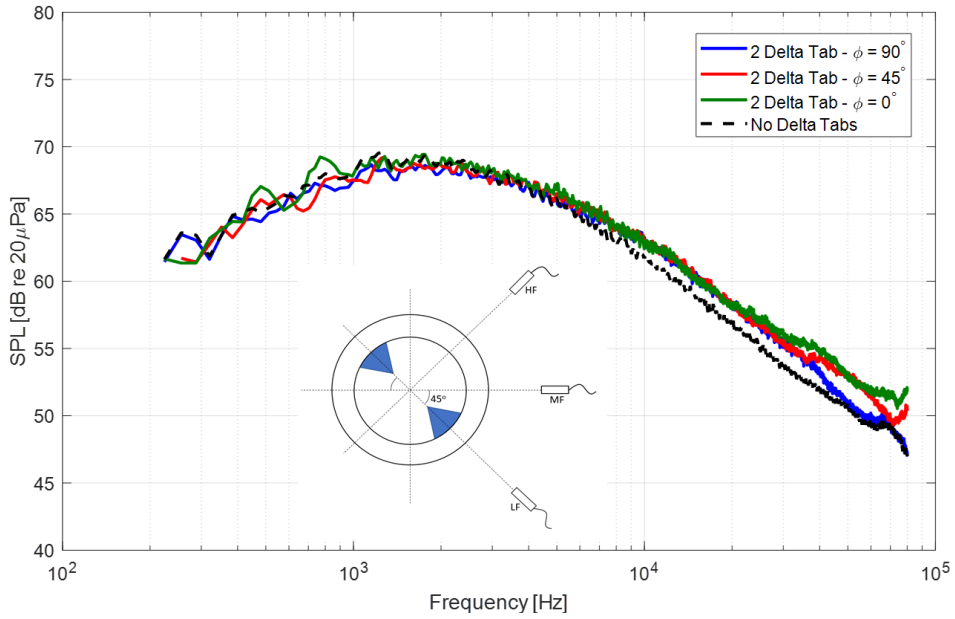

Figure 18. Effect of delta tabs on the noise from the confluent nozzle. De =1.7 in, Le/De = 0.7. PR1 = 1.39, ER = 1.00, Tt,1 = 500°F, Tt,2 = 60°F, R = 12 ft, θ = 90°, Δf = 32 Hz, lossless. SPL: sound pressure level.

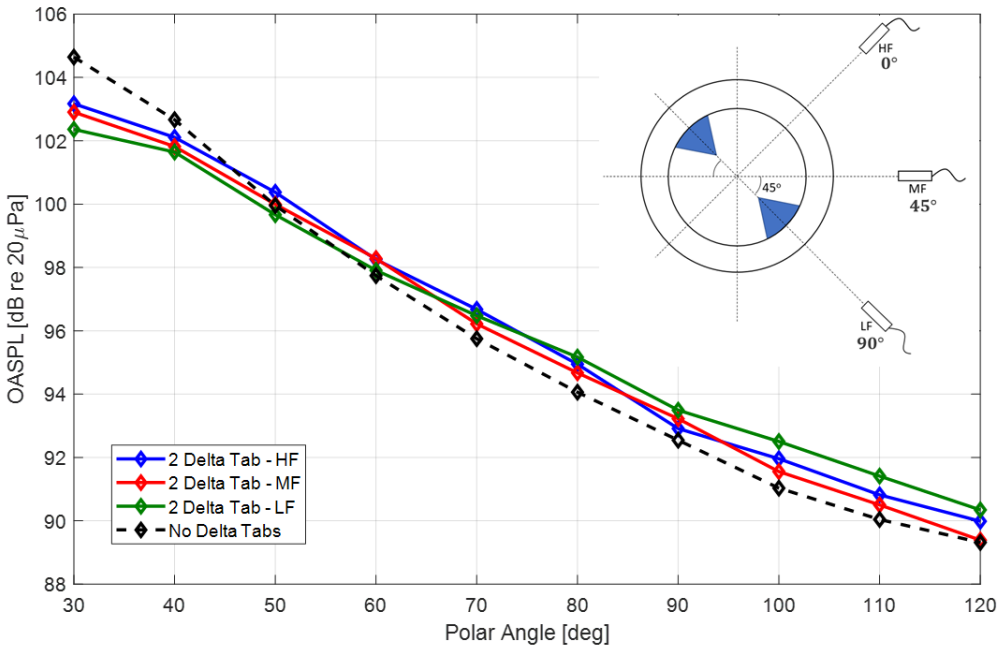

Figure 19. Effect of delta tabs on the noise from the confluent nozzle. De =1.7 in, Le/De = 0.7. PR1 = 1.39, ER = 1.00, Tt,1 = 500°F, Tt,2 = 60°F, R = 12 ft, Δf = 32 Hz, lossless. SPL: sound pressure level.

Particle Image Velocimetry Measurements

Facility Set-up and Testing Description

The PIV data was acquired in GTRI's Flow-Diagnostics Facility using a double-pulsed, two-dimensional (2D) PIV system. The details of GTRI's Flow-Diagnostics Facility were reported by Burrin et al. (1979), with salient details repeated here for completeness. The Flow-Diagnostics Facility is a sister facility to GTRI's Anechoic Jet Facility having identical plenum interfaces and identical plenum-to-nozzle area contraction ratios.

The PIV system is shown schematically in Figure 20. Figure 20a and Figure 20b show side-view and top-down-view schematics of this system, respectively. Figure 20c illustrates the camera's nominal field-of-view at each of the stations along the traverse. In selecting the time delay between image pairs, an optimization routine built into the DaVis software was used. The DaVis software is the LaVision™ proprietary PIV software that is used for the data acquisition and post-processing. This routine recommends a time delay between image pairs based in part on the peak Q-ratio (the ratio of highest and second highest correlation peak values) for several different time delays. A low Q-ratio indicates that a particle displacement cannot be accurately predicted from the correlation plane of a given image pair in a given interrogation window.

The measured instantaneous velocity fields may contain spurious velocity vectors. Spurious vectors are characterized by exceedingly large or small magnitudes and/or erroneous directions relative to the expected velocity vector field. Of course, as the expected vector field is not known a priori, criteria for identifying spurious vectors must be employed. In this work, spurious vectors are detected and rejected at two different stages of the data processing routine. First, the instantaneous velocity fields are screened in a processing stage referred to as vector post-processing. A filtering operation is used to detect and replace vectors that have a large deviation from their neighbors. This filtering operation is based on the framework of a dynamic mean value operator (Raffel et al., 2018). In particular, the filter was set to “strongly remove and iteratively replace" in the DaVis software – removing vectors that had a difference to the local mean outside of one standard deviation of the neighboring vectors before re-inserting vectors whose difference to the local mean is within two standard deviations of the neighboring vectors once the filter was applied. For vectors that failed to satisfy the criterion, the median of the neighbors was used to replace the vector. This filter was executed twice on each instantaneous velocity field. Further, a range of acceptable particle displacements was specified. Finally, any instantaneous vectors whose associated Q-ratio was less than 2.0 were deleted. The success of these vector post-processing operations in removing outliers without modifying the remainder of the velocity field is shown to be successful on a single, instantaneous velocity field in Figure 21. The top frame shows the result without the vector post-processing routine, and the bottom frame shows the same field with the vector post-processing routine executed – both of which use the same color scaling shown on the far right. This vector field is a measurement across the shear layer of the jet from the core nozzle in isolation operated at $\boldsymbol{M}_j$ = 0.58, unheated – with the jet flowing from left to right in the figure.

™ LaVision is a trademark of LaVision GmbH, Germany.

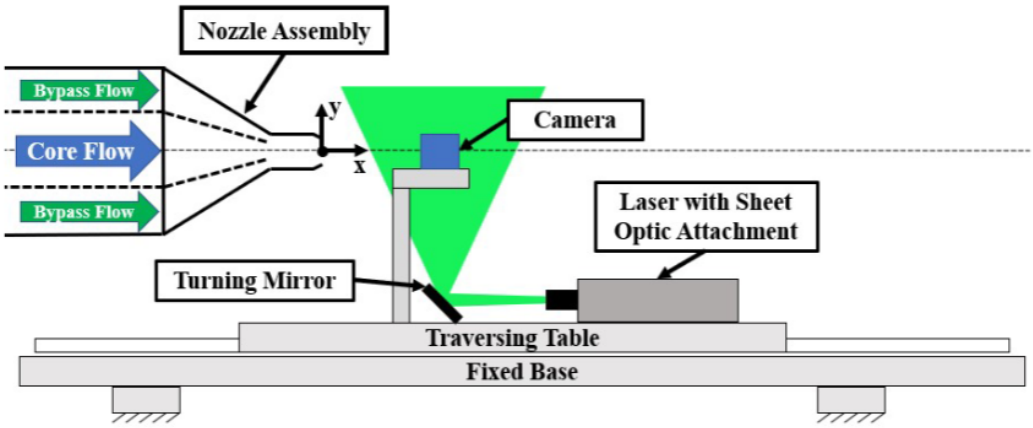

(a)

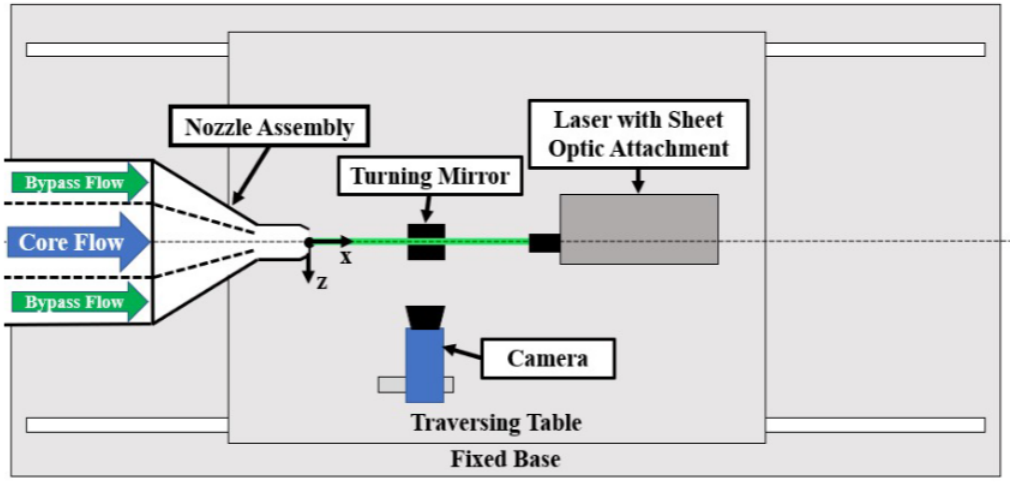

(b)

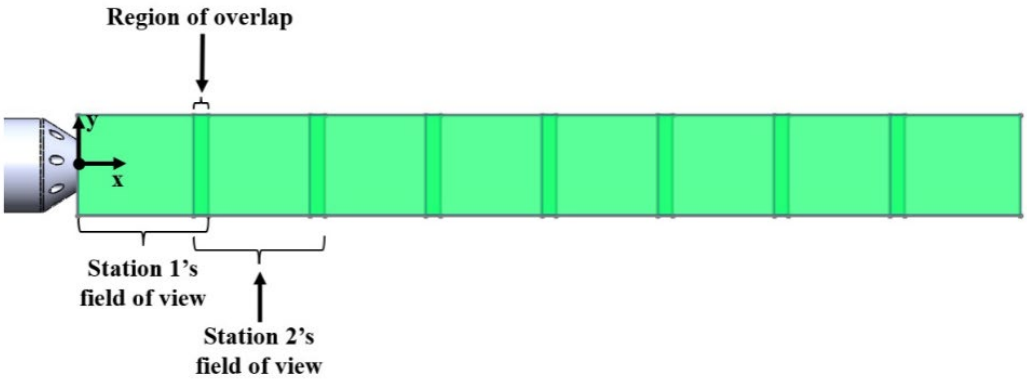

(c)

Figure 20. PIV system: (a) side view, (b), top-down view, and (c) multi-station acquisition scheme.

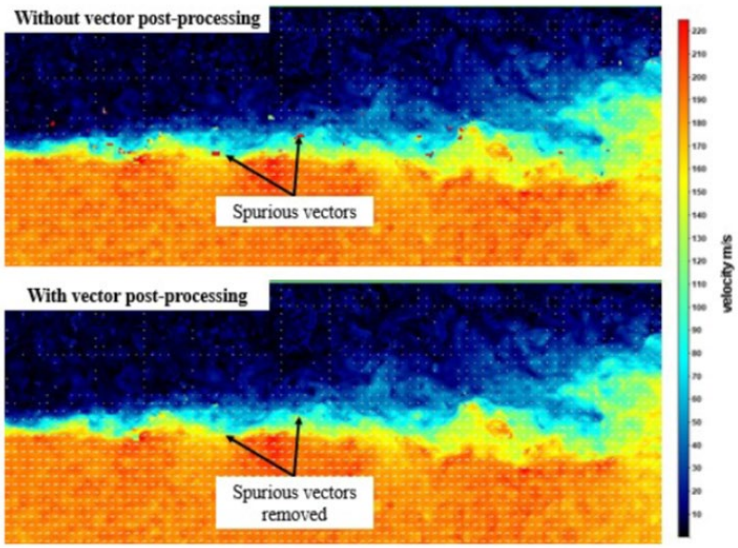

Figure 21. Success of vector post-processing in replacing spurious vectors. Both frames show same region of shear layer of jet from single nozzle in isolation, $M_j = 0.58$, unheated.

The ensemble averaging of the PIV measurements also includes applying Chauvenet's criterion for spurious vector (i.e., outlier) rejection. This only has an appreciable impact on the measurements of velocity fluctuation (i.e., turbulence intensity), with relatively small changes to the mean velocity measurements. Chauvenet's criterion was reported to be used by Bridges and Wernet (2011) and is a sample-size-dependent criterion that suggests thresholds outside of which values are unlikely to be sampled. If values are measured outside of these thresholds, the data are considered outliers. In each PIV interrogation window across all instantaneous velocity fields being ensemble averaged, Chauvenet's criterion is applied to each component of the measured velocity vectors. This criterion assumes that the measured velocities within each interrogation window are sampled from a Gaussian parent distribution. The reader astute in turbulent flows would likely dispute this assumption, and rightfully so. It is known that the turbulent velocities in a free shear layer are not always Gaussian distributed (as discussed in greater detail by Pope [2000]). In particular, the probability density function (PDF) of velocity at a point may have non-zero skewness – whereas a Gaussian distribution would have zero skewness. This potential criticism is acknowledged; however, a Gaussian PDF of velocities is not assumed aside from computing outlier rejection thresholds. Histograms of displacement in units of pixels as acquired using the PIV measurement system are presented in Figure 22. Figure 22 shows that the use of Chauvenet's criterion correctly flags obviously spurious vectors (at the tips of the red arrows) without wrongly flagging seemingly trustworthy vectors (based on their presence in a larger distribution of data). Displaying the displacement histogram with units of pixels serves the secondary purpose of providing evidence that the PIV measurements are not impacted by peak-locking effects. Were peak-locking present in the data, the displacement vectors would be biased toward integer displacement values (Raffel et al., 2018). Demonstrating this fact is vital to the integrity of the fluctuating velocity measurements produced, as Christensen (2004) showed that peak-locking may strongly impact second-order velocity statistics (i.e., the standard deviation of velocity reported in the present work).

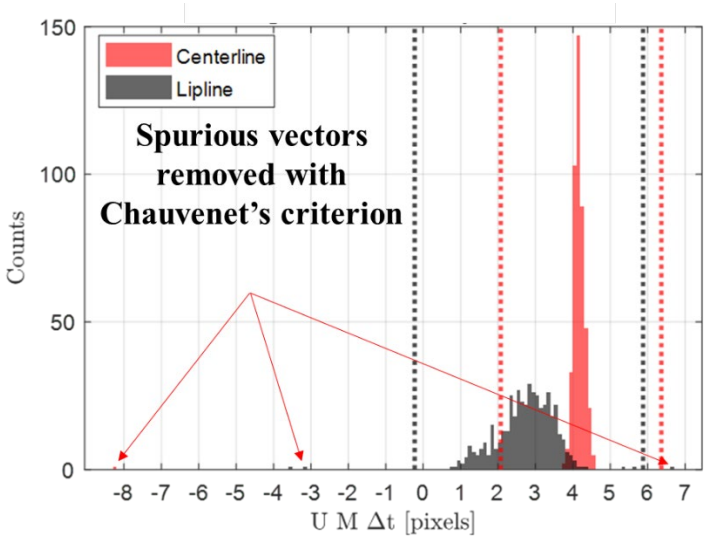

Figure 22. Histogram of axial displacement along lipline (x/D_e= 0.7, y/D_e=0.5, N=1500 image pairs) of jet from single nozzle (M_j = 0.58, unheated). Vertical lines show Chauvenet criterion boundaries.

Extensive care was taken to ensure that the measured PIV data were accurate and precise, including validating measurements against well-trusted, existing data provided in literature. Ahuja et al. (1982) acquired mean and unsteady velocity measurements of a jet produced by a convergent nozzle with an exit diameter of 2 in. (5.08 cm) in the GTRI Flow Diagnostics Facility using a laser doppler velocimetry (LDV) system. As shown by Bridges and Wernet (2011), the LDV data of Ahuja et al. (1982) and several other sources of published jet flow field measurements agree reasonably well when normalized. Thus, in the present work, agreement between flow-field measurements reported by Ahuja, et al. (1982) and a validation dataset acquired using the present work's PIV system (when both are presented in normalized form) is taken to provide a high degree of confidence in the PIV measurements. This relies, of course, on the accuracy of historical datasets. The 1.6-in. nozzle used here is shown in Figure 23a and the agreement between the validation dataset is shown in Figure 23b. This agreement is even better than before Chauvenet's criteria were implemented in the data processing routine.

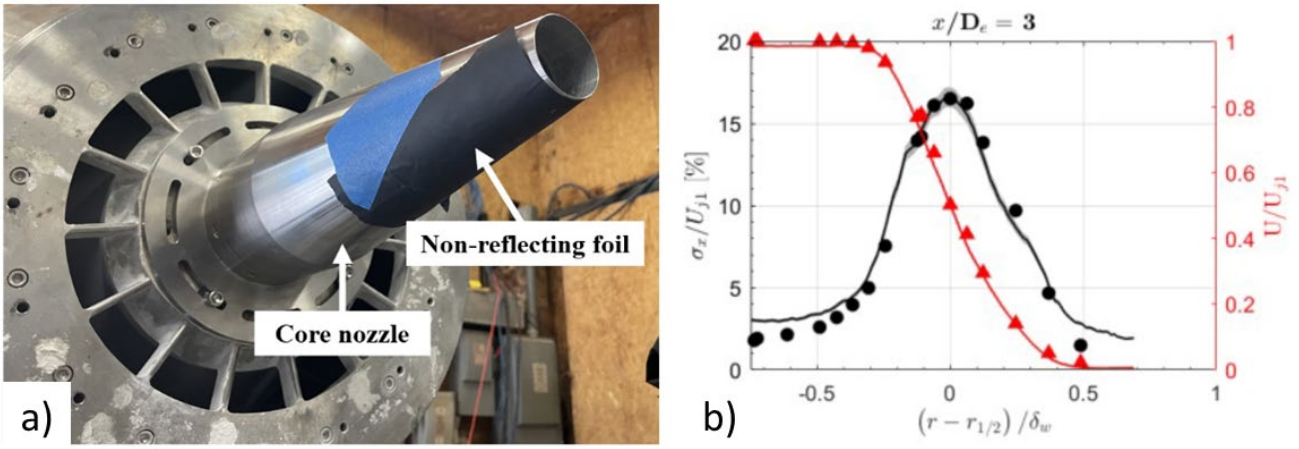

Figure 23. Validation dataset: (a) nozzle used and (b) agreement with dataset from Ahuja et al. (1982) (curves are PIV data, symbols are historical laser doppler velocimetry (LDV) data from Ahuja et al. [1982]).

Witze (1974) provided a model for the centerline velocity distribution of a compressible free jet, which was shown to agree well with experimental data. Bridges and Wernet (2011) used the potential core length obtained by the theory reported by Witze (1974) as a means to collapse PIV measurements acquired at different conditions. The "Witze model" (as it will be referred to hereafter) may be expressed as:

$$\bar{u}_c\left(\frac{x}{D_e}\right) = 1 - \exp\left(\frac{-1}{2\kappa\left(\frac{x}{D_e}\right)(\bar{\rho}_e)^{0.5} - X_c}\right) \quad \text{(Eq. 1)}$$

$$\kappa = 0.08\left(1 - 0.16M_j\right)(\bar{\rho}_e)^{-0.22} \quad \text{(Eq. 2)}$$

Here, $X_c = 0.70$, and the remaining parameters are defined in Witze's report.

PIV Analysis

Figure 24 shows typical jet flow fields at a lower pressure ratio ($PR_1 = PR_2 = 1.39$, unheated) where howling does not occur. The centerline mean velocity distribution of three different mixing-duct lengths with unity extraction ratio at $PR_1 = 1.39$ are shown in Figure 25 along with Witze's model. It can be seen that all curves agree reasonably well with Witze's model for the lower pressure ratio, regardless of mixing-duct length.

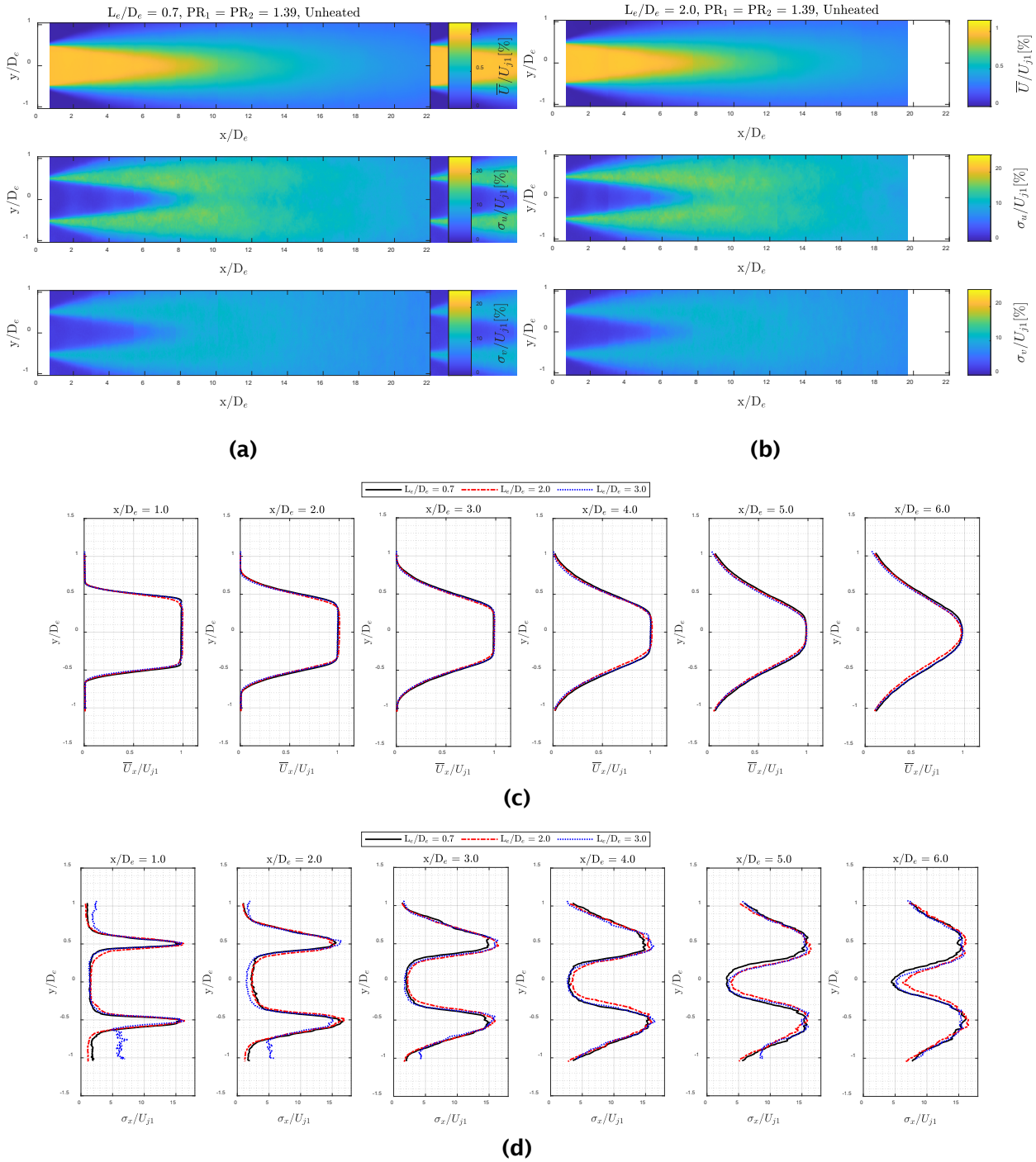

Figure 24. Typical flow field of jet from confluent nozzle ($PR_1 = PR_2 = 1.39$, unheated) : (a) mean velocity, axial fluctuation intensity, and radial fluctuation intensity for $L_e/D_e = 0.7$, (b) mean velocity, axial fluctuation intensity, and radial fluctuation intensity for $L_e/D_e = 2.0$, (c) radial profiles of mean velocity near the nozzle exit for several mixing-duct lengths, and (d) radial profiles of axial fluctuation intensity near the nozzle exit for three mixing-duct lengths. N = 750 image pairs.

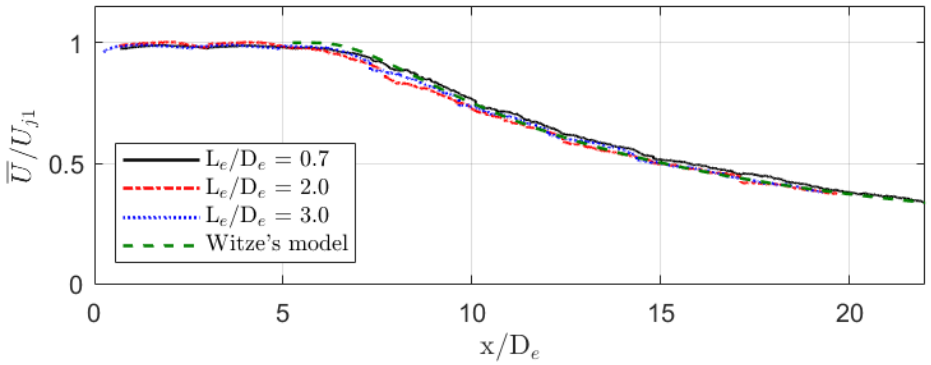

Figure 25. Centerline mean velocity distributions of typical flow field including Witze's model for single jet ($\boldsymbol{PR_1 = PR_2 = 1.39}$, unheated). N = 750 image pairs.

It is noted that there exists a mean axial velocity gradient close to the nozzle exit plane in Figure 25, and some explanations for this are offered. This phenomenon is believed to be a result of the contraction of the exhaust nozzle proximate to its exit plane. The contraction requires the fluid to turn radially inward near the upstream side of the exhaust nozzle and then to straighten out in a similar fashion near the exhaust nozzle exit plane. At these two locations, a force is required for the fluid to turn. Near the upstream side of the exhaust nozzle, the required force is supplied by the solid body of the nozzle. Near the exhaust nozzle exit plane, no solid body exists to supply the required force – it must instead come from the fluid itself in the form of a pressure gradient if the flow is to become approximately parallel as it exits the nozzle. The fluid near the center of the exhaust nozzle may supply the required pressure gradient if the fluid is at an elevated static pressure and thus has not yet reached its fully expanded velocity. Morris et al. (2010) measured a similar effect in the flow field produced by a single nozzle and also attributed this effect to the nozzle's convergence at the nozzle exit plane.

Six heated core conditions were selected for the confluent nozzle with both the shortest mixing-duct length ($L/D_e = 0.7$), and the longest mixing-duct length ($L/D_e = 3.0$). Only non-resonating conditions were chosen, as they are most useful to the modelers; these conditions are shown in Figure 26. Two conditions for each mixing-duct length are acquired with a high number of samples (750 samples) to allow for accurate turbulence measurements. These conditions are $PR_1 = PR_2 = 1.39$ and $PR_1 = 1.39, ER = 1.07$. For mean flow measurements, all other conditions are acquired at a lower number of samples (200), sufficient for capturing mean statistics of the flow.

Tt1 = 500 deg F		Primary Pressure Ratio, PR1			
		1.39 (M_{j1}=0.7)	1.52 (M_{j1}=0.8)	1.69 (M_{j1}=0.9)	1.89 (M_{j1}=1.0)
PR2	1.39 (M_{j2}=0.7)	ER = 1.00	ER = 0.91	ER = 0.82	ER = 0.73
	1.52 (M_{j2}=0.8)	ER = 1.10	ER = 1.00	ER = 0.90	ER = 0.91
	1.69 (M_{j2}=0.9)	ER = 1.22	ER = 1.11	ER = 1.00	ER = 1.89
	1.89 (M_{j2}=1.0)	ER = 1.36	ER = 1.24	ER = 1.12	ER = 1.00
ER	1.04	PR2 = 1.44			
	1.07	PR2 = 1.48			

Figure 26. Data matrix for heated core PIV conditions. ER: extraction ratio, PR: pressure ratio.

Although data for a total of twelve flow conditions were gathered using PIV, results of only one condition for each mixing-duct length will be treated in detail below for the sake of brevity. In particular, the plots of the $PR_1 = PR_2 = 1.39$ heated condition will be discussed for the confluent nozzle with L_e/D_e = 0.7 and 3.0 mixing-duct lengths, since both mean and turbulent statistics are gathered for this condition. The 2D mean and turbulence intensity plots are shown in Figure 27. Note that a thin region near the nozzle exit has been masked off from the final PIV data to reject the effects of laser reflections off the nozzle. The length of this mask is from x/D_e = 0 to about 0.3-0.5 depending on the intensity of the reflections. Figure 28 shows comparisons of mean axial velocity and axial and radial turbulence intensities along the jet centerline for each mixing-duct length. Similarly, Figure 29 compares profiles of axial velocity and axial and radial turbulence intensities at various slices near the exhaust nozzle exit. Data for the L_e/D_e = 0.7 configuration are shown as solid black curves while those for L_e/D_e = 3.0 are shown as dashed blue curves.

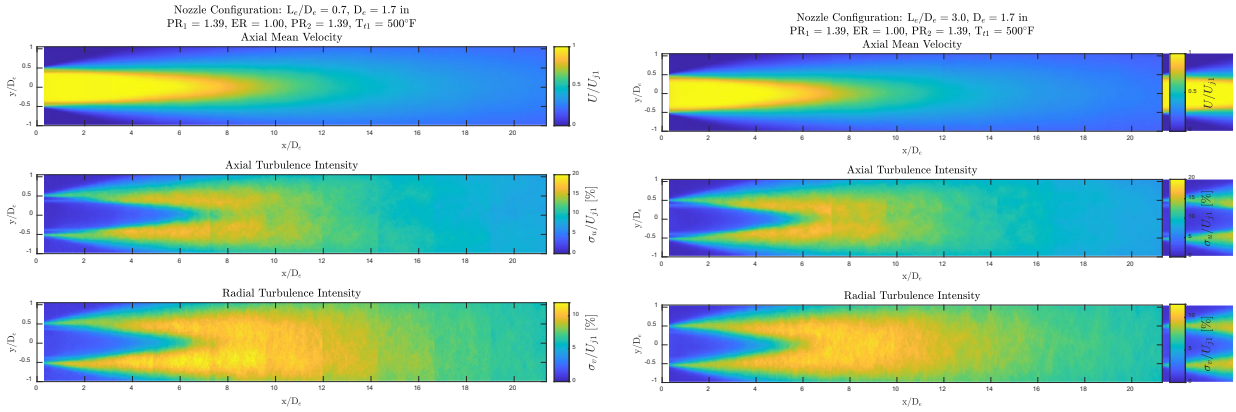

(a) **(b)**

Figure 27. Two-dimensional mean and turbulence intensity plots. PR_1 = 1.39, PR_2 = 1.39, T_{t1} = 500°F, where (a) L_e/D_e = 0.7 and (b) L_e/D_e = 3.0, N = 750 image pairs.

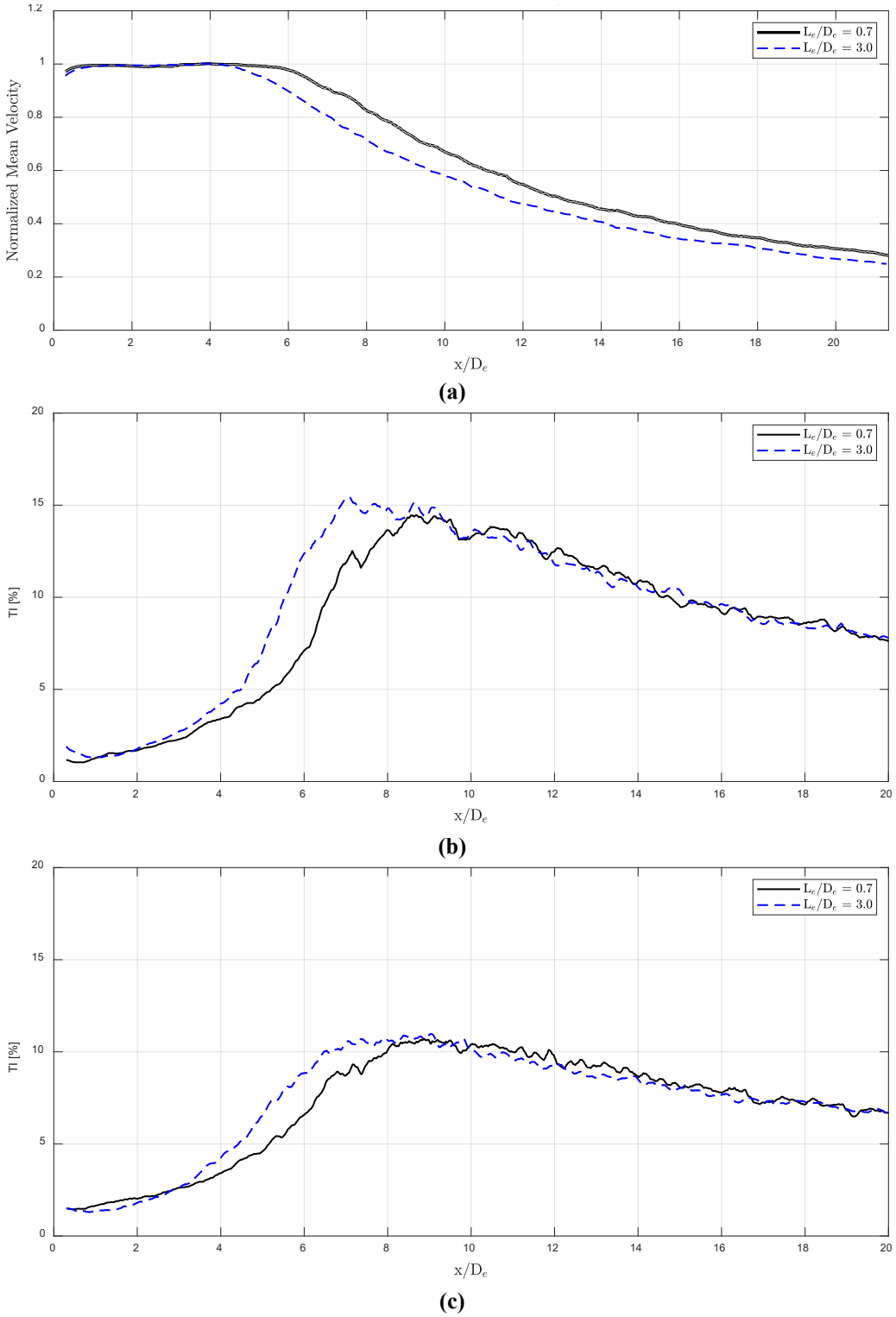

Figure 28. Comparisons of centerline (a) mean axial velocity and (b) axial and c) radial turbulence intensities (TI) between mixing-duct lengths. PR_1 = 1.39, PR_2 = 1.39, T_{t1} = 500°F, L_e/D_e = 0.7 and L_e/D_e = 3.0, N = 750 image pairs.

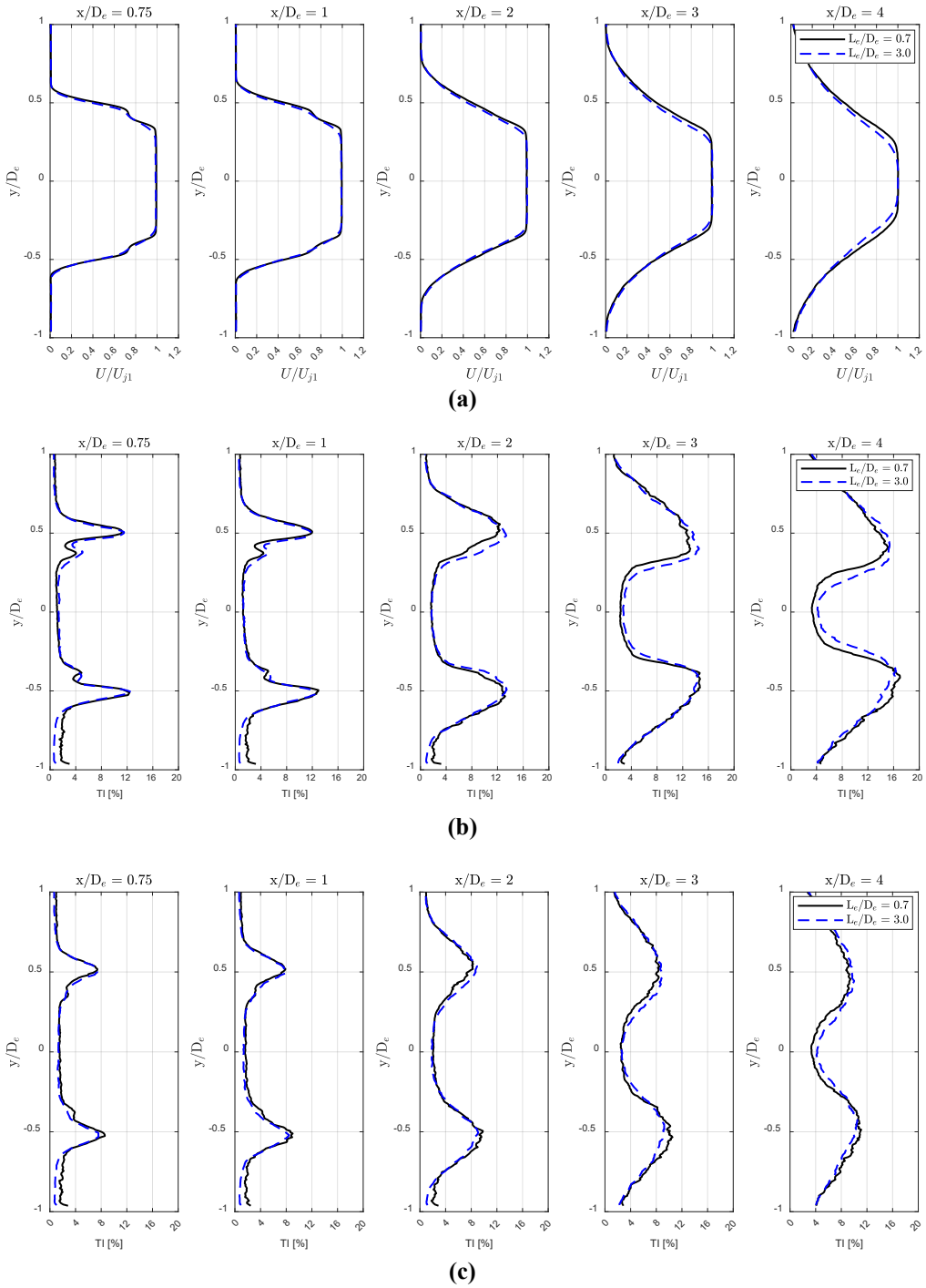

Figure 29. Comparisons of a) mean axial velocity and b) axial and c) radial turbulence intensity profiles between mixing-duct lengths at various x/D_e. PR_1 = 1.39, PR_2 = 1.39, T_{t1} = 500°F, L_e/D_e = 0.7 and L_e/D_e = 3.0, N = 750 image pairs.

With a heated core stream, there are observable differences in the flowfield from the internally mixed jet between the two mixing-duct lengths. The centerline velocity distribution in Figure 28a shows a decrease in the length of the potential core

of about one diameter when increasing the mixing-duct length from its shortest value of L_e/D_e = 0.7 to L_e/D_e = 3.0. This effect is also captured in the velocity profiles shown in Figure 29a as the profiles for the longer mixing-duct length seem to smoothen out slightly sooner as one traverses downstream.

High-Speed Schlieren Flow Visualization

Facility Set-up and Testing Description

GTRI's schlieren setup is shown in Figure 30. An arc lamp light source emits light that follows a z-shaped path along a series of mirrors and lenses. The light source is positioned at the focal point of the first parabolic mirror, sending collimated light into the test section (the horizontal region between the two parabolic mirrors). The second parabolic mirror focuses the light rays (now refracted by density gradients within the test section) to a focal point. At the appropriate focal point, a knife edge cutoff is positioned in one of two orientations: vertical (knife edge normal to jet axis) or horizontal (knife edge parallel to jet axis). These two knife edge orientations reveal axial and transverse density gradients in the test section, respectively. The light is then passed through a pair of refocusing lenses that allow the camera to be placed far from the jet, which may be heated, in order to protect the camera. The schlieren images are captured on a Vision Research Phantom® V2512 monochrome ultrahigh-speed camera, with a resolution of 1,280 x 800 pixels at 25,000 frames per second and with a 1 μs exposure time. The video files being released to modeling teams will be in the .AVI format, with 100 frames total at 20 frames per second. While only short, 100-frame videos are being released, 2,500 images were recorded at each condition and the longer duration measurements are available upon request.

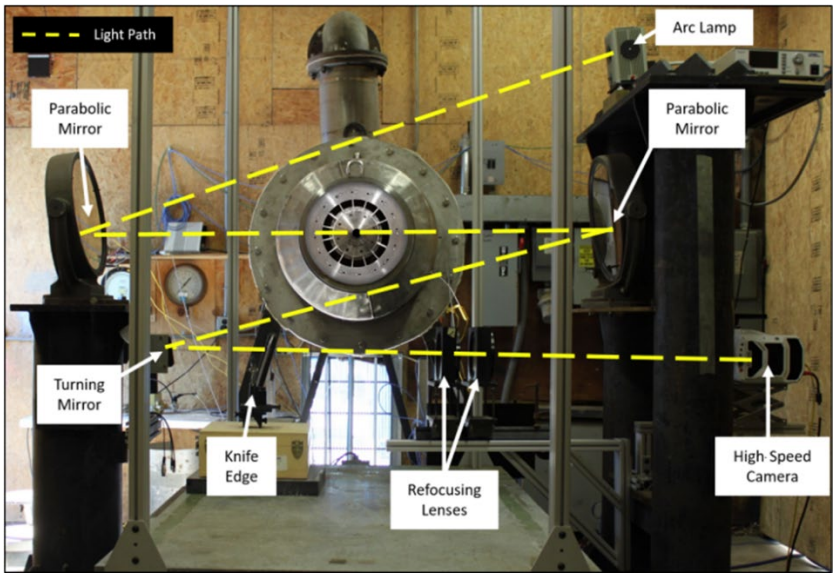

Figure 30. GTRI's Z-shaped schlieren setup (Ramsey et al., 2022b).

Schlieren Visualizations

Representative schlieren snapshots are shown for the shortest mixing-duct length (L_e/D_e = 0.7) and ER = 1.00 in Figures 31 through 33, each of which shows both transverse and axial density gradients. As the pressure ratio (and thus its Reynolds number) is increased, the turbulent density gradients become more and more well-defined. This is expected for two reasons. First, turbulent velocity fluctuations and their associated stresses on the fluid increase with Mach number. Secondly, the smallest scales of turbulence decrease with increasing Reynolds number ($Re = U_j D_e/\nu$). Relatively small changes are caused to the apparent density gradients by increasing ER from 1.00 to 1.07 at the PR_1 = 1.39 condition, as shown in Figure 34. Similarly, little change is seen as ER is set to 1.10 (Figure 35). For the most part, the flow field at all of these conditions remains typical of turbulent jets.

® Phantom is a registered trademark of Vision Research, Inc., Wayne, New Jersey.

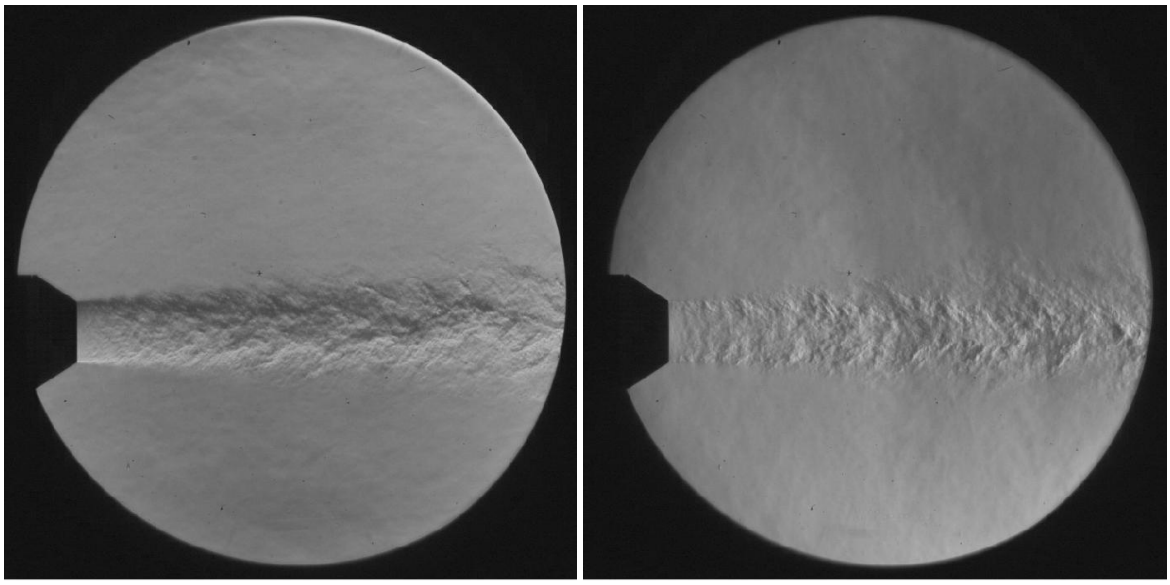

(a) (b)

Figure 31. Schlieren flow visualization of $L_e/D_e = 0.7$ at $PR_1 = 1.39$, $ER = 1.00$, $PR_2 = 1.39$, unheated configuration: (a) transverse density gradients and (b) axial density gradients.

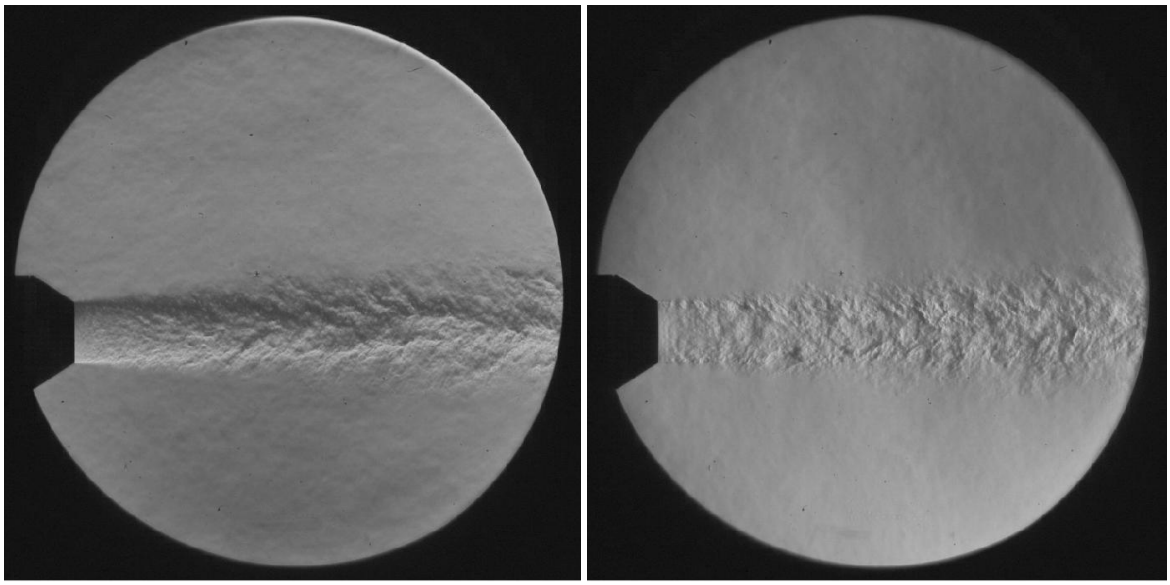

(a) (b)

Figure 32. Schlieren flow visualization of L_e/D_e = 0.7 at $PR_1 = 1.52$, $ER = 1.00$, $PR_2 = 1.52$ unheated configuration: (a) transverse density gradients and (b) axial density gradients.

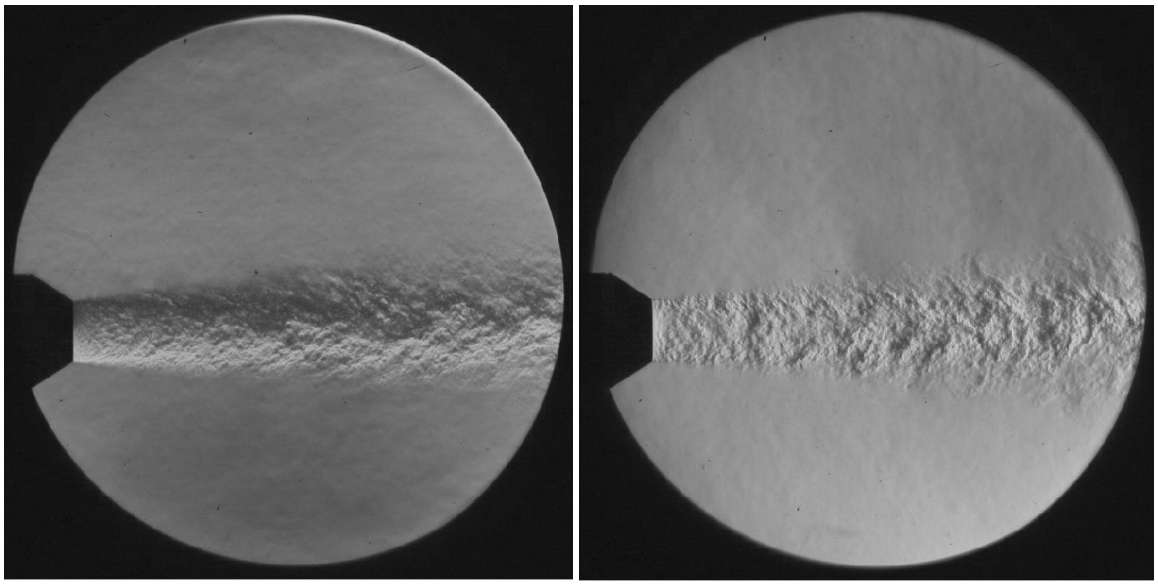

(a) (b)

Figure 33. Schlieren flow visualization of L_e/D_e = 0.7 at $PR_1 = 1.89, ER = 1.00, PR_2 = 1.89$, unheated configuration: (a) transverse density gradients and (b) axial density gradients.

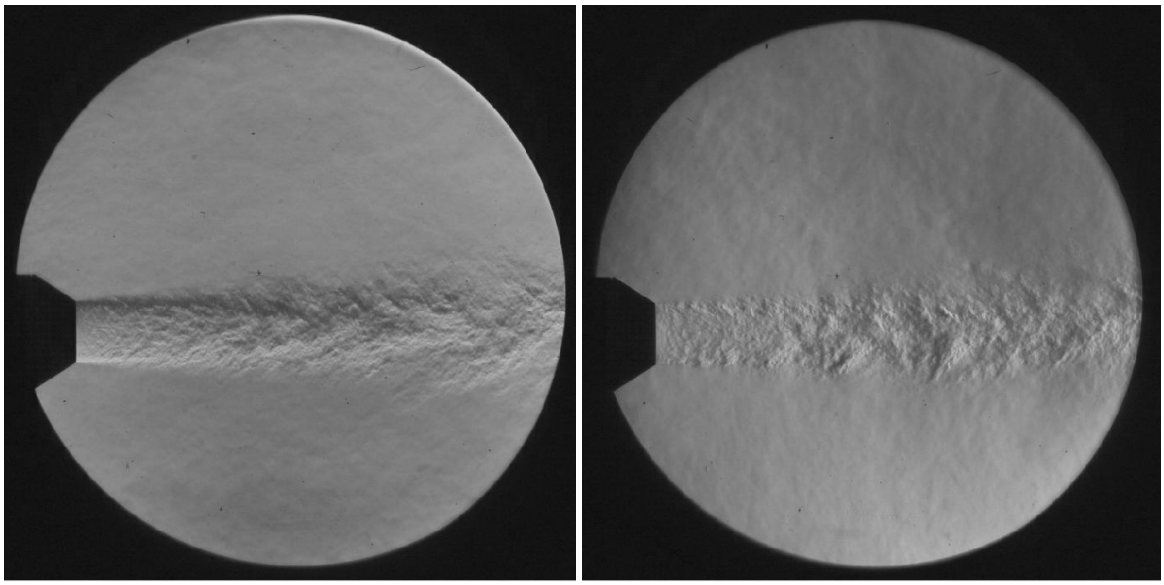

(a) (b)

Figure 34. Schlieren flow visualization of L_e/D_e = 0.7 at $PR_1 = 1.39$, $ER = 1.07$, $PR_2 = 1.49$, unheated configuration: (a) transverse density gradients and (b) axial density gradients.

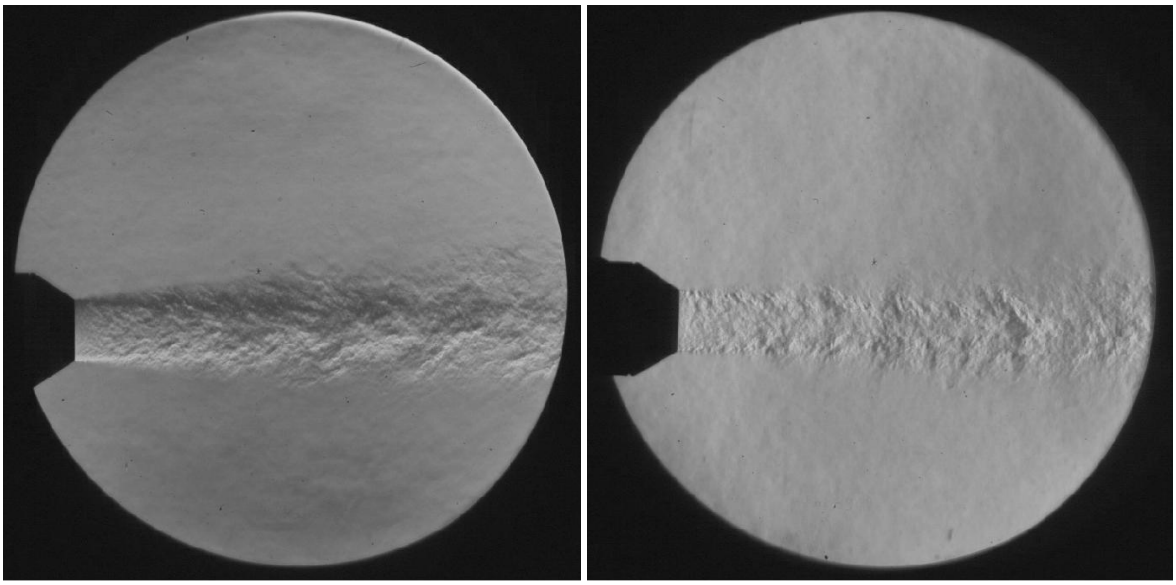

(a) **(b)**

Figure 35. Schlieren flow visualization of $\boldsymbol{L_e/D_e = 0.7}$ at $\boldsymbol{PR_1 = 1.39}$, ER = 1.10, PR_2=1.52 unheated configuration: (a) transverse density gradients and (b) axial density gradients.

Time-resolved schlieren visualizations were recorded for each of the six heated core conditions identified in Figure 26 for both the shortest L_e/D_e = 0.7 and longest L_e/D_e = 3.0 mixing-duct lengths. The resulting visualizations acquired using both mixing-duct lengths are remarkably similar as seen by comparing Figures 36 and 37. This indicates that the noise of the two mixing-duct lengths will also remain largely unchanged as indeed noted in previous sections.

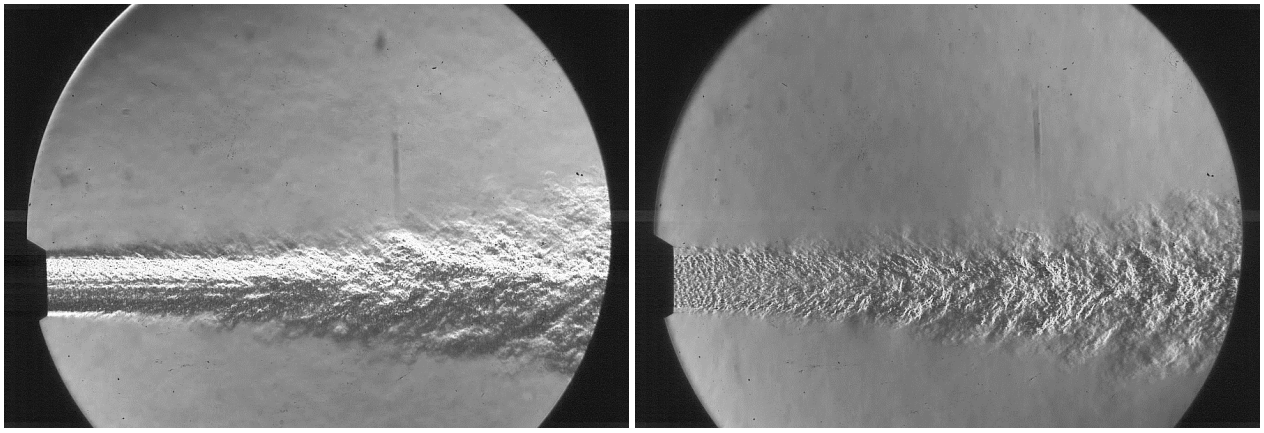

(a) **(b)**

Figure 36. Schlieren flow visualization of $\boldsymbol{L_e/D_e = 0.7}$ at $\boldsymbol{PR_1 = 1.39}$, $\boldsymbol{ER = 1.07}$, T_{t1} = 500°F configuration: (a) transverse density gradients and (b) axial density gradients. 1.5 μs exposure, f_s = 44 kHz

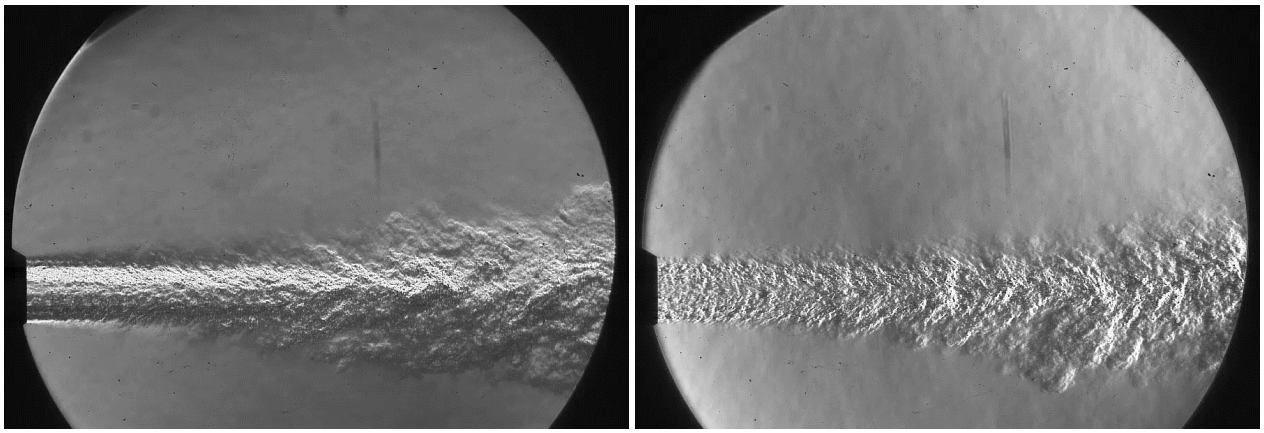

(a) (b)

Figure 37. Schlieren flow visualization of $\boldsymbol{L_e/D_e = 3.0}$ at $\boldsymbol{PR_1 = 1.39}$, $\boldsymbol{ER = 1.07}$, T_{t1} = 500°F configuration: (a) transverse density gradients and (b) axial density gradients. 1.5 µs exposure, f_s = 44 kHz.

These results are in agreement with the trends in the measured farfield noise of axisymmetric confluent nozzles reported by Ramsey et al. (2022a) – that is, the mixing-duct length of the nozzle has little effect on the noise and as such, there is little mixing accomplished upstream of the baseline exhaust nozzle exit in either case. For the sake of brevity, representative frames from only a single operating condition are shown. These visualizations look remarkably different when compared to those acquired with an unheated core stream. With an elevated core temperature, density gradients become more extreme, especially in the core-bypass shear layer as captured in Figures 36a and 37a. Additionally, compared to the unheated case, the plume width of the heated jets are broader, a commonly observed phenomenon reported in the literature.

Acoustic Source Location

Facility Set-up and Testing Description

Figure 38 shows the beamformer array mounted in the GTRI Flow Diagnostics Facility. The beamformer, developed by OptiNav™ for GTRI, consists of an array of 48 Earthworks Audio™ M30 microphones arranged in a spiral pattern emanating from the center of the beamformer resulting in an array approximately 3 ft across. It is an assembly of ¼-in. omnidirectional microphones with a flat free-field response from 5 Hz to 30 kHz with a peak input sound pressure level of 142 dB. The signals from the array of microphones are fed into three separate MOTU® Stage B16 digital mixers. They are then routed from each of these B16s to an Audio Video Bridging switch, which feeds the data to a MOTU timing unit. Analysis is performed using a Beamforming Interactive software package designed by OptiNav, primarily by using the "frequency sweep" option, which beamforms each band of the recorded one-twelfth octave spectra individually and records the resulting location for each frequency band. In some cases, multiple sources of comparable strength can exist, in which case multiple peak source locations are recorded and arranged in order of relative intensity. The choice of one-twelfth octave acts as a compromise between narrowband which results in an overwhelming number of data points leading to difficulties in comparing data and one-third octave which results in too few data points to accurately resolve trends in the data. For a more in-depth description of the beamformer and its uses at GTRI, the reader is directed to the works of Breen and Ahuja (2019, 2020) and Breen (2019).

™ OptiNav is a trademark of OptiNav, Inc., Bellevue, Washington.
™ Earthworks Audio is a trademark of Earthworks, Inc., Milford, New Hampshire.
® MOTU is a registered trademark of Mark of the Unicorn, Inc., Cambridge, Massachusetts.

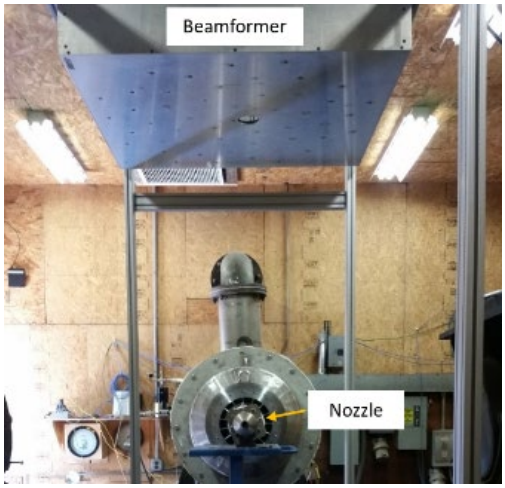

Figure 38. GTRI's acoustic beamforming setup (Breen & Ahuja, 2020).

Source Location Analysis

Acoustic source location data was acquired for the same six heated core conditions that were outlined in the text matrix shown in Figure 26 with both the shortest L_e/D_e = 0.7 and longest L_e/D_e = 3.0 mixing-duct lengths. Figure 39 shows an example of acoustic source-location data. In this plot, the streamwise location as measured from the exit of the final exhaust nozzle of the strongest source at a given frequency is plotted. This is done by computing a noise level contour for each frequency band and isolating the contour peak as the loudest source occurring in that band. The color of each data marker shows the strength of the source with bright yellow corresponding to peak jet noise. Note that the resolution of the array at low frequencies (below approximately 300 – 400 Hz) is rather poor. This is evidenced in the data as low-frequency sources suddenly move back upstream toward the nozzle exit. At higher frequencies where the beam width is very narrow, the beamformer is accurately able to discern the location of the contour peak versus its centroid. At lower frequencies the beam width is much wider, and as shown in Breen and Ahuja (2020) this results in an averaging of the source strength for the given frequency, shifting the peak location to the centroid of the contour. Frequencies in this range are, therefore, not shown in any subsequent source location plots in this report. All source location data is one-twelfth octave. Without a clear characteristic diameter and velocity needed to normalize the location and frequency, the data displayed here are not plotted against a non-dimensional frequency as typically found in the round-jet noise literature. In later sections when discussing source location results using the lobed internal mixer nozzles obtained from GAC, some attempts to collapse and compare data using a Strouhal number based both on the core-jet velocity U_{j1} and the theoretically fully-mixed velocity, U_{mix}, will be made.

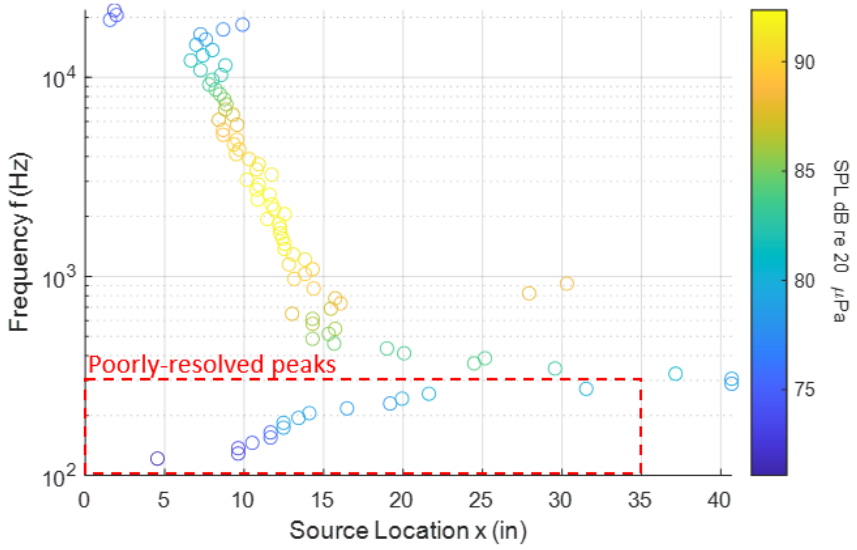

Figure 39. Source location of the Y1 GT dual-stream jet, L_e/D_e = 0.7. PR_1 = 1.39, ER = 1.07, T_{t1} = 500°F, one-twelfth octave band data. SPL: sound pressure level.

Higher-frequency noise sources are typically associated with the portion of the jet's shear layer closer to the nozzle exit where turbulent length scales are small. Enhanced levels of internal mixing would be characterized by movement of noise sources closer to the nozzle exit. For a rapidly-mixed, dual-stream jet (such as one produced through the use of a forced mixer), one might expect the source distribution to follow a steeper curve. This would be due to a more thoroughly mixed jet expanding faster once it has exited the nozzle, resulting in noise sources at all frequencies being measured as emanating from closer to the nozzle exit. A direct comparison between the results from the shortest and longest mixing-duct lengths shows a slight upstream shift of noise sources for the longer mixing-duct length: potentially evidence of enhanced mixing due to the longer mixing-duct length. Figures 40 through 42 below show the source locations for the shortest and longest mixing-duct lengths for three different heated conditions: one at unity extraction ratio and two slightly above unity (ER = 1.04 and 1.07). For all conditions, the noise sources move slightly closer to the nozzle exit as the mixing-duct length is increased, which would be expected of noise generated upstream of the nozzle exit associated with internal mixing. This effect is more pronounced for the unity extraction ratio case but is less pronounced as the secondary stream pressure ratio is increased. For the frequency range between 1 and 10 kHz, the sources move approximately 0.82 diameters upstream for the unity extraction ratio case, 0.27 diameters upstream for ER = 1.04, and 0.25 diameters upstream for ER = 1.07. The results shown in Figure 40 comparing the source distributions between the shortest and longest mixing-duct lengths at PR_1 = 1.39, PR_2 = 1.39, T_{t1} = 500°F are corroborated by the results obtained from PIV at the same condition shown in Figure 28a. That is, the nearly one-diameter upstream shift of noise sources when using the longest exhaust mixing-duct length is in part explained by the nearly one-diameter decrease in the length of the potential core.

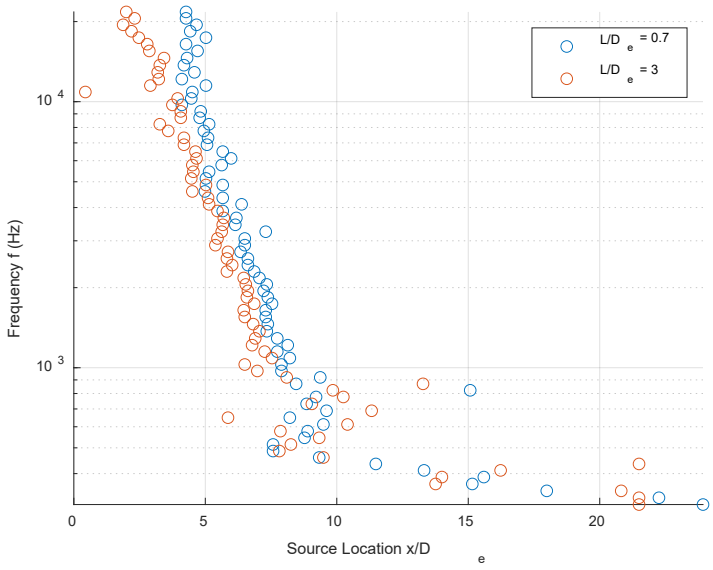

Figure 40. Comparison of source locations between L_e/D_e = 0.7 and 3.0. PR_1 = 1.39, PR_2 = 1.39, T_{t1} = 500°F,

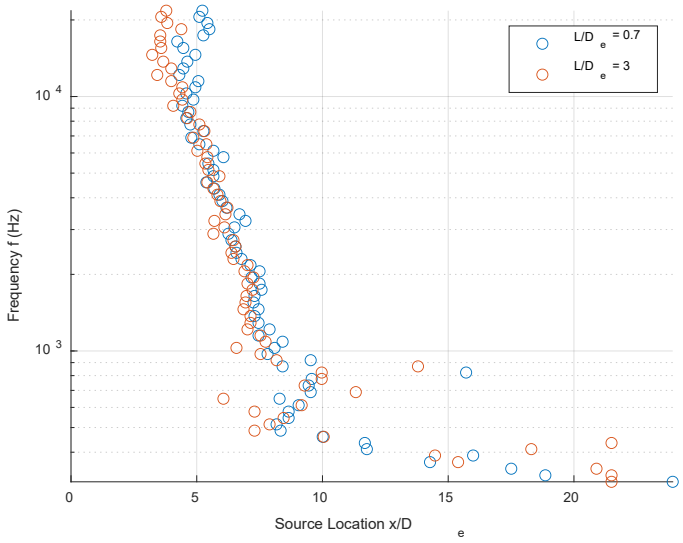

Figure 41. Comparison of source locations between L_e/D_e = 0.7 and 3.0. PR_1 = 1.39, ER = 1.04, T_{t1} = 500°F, one-twelfth octave band data.

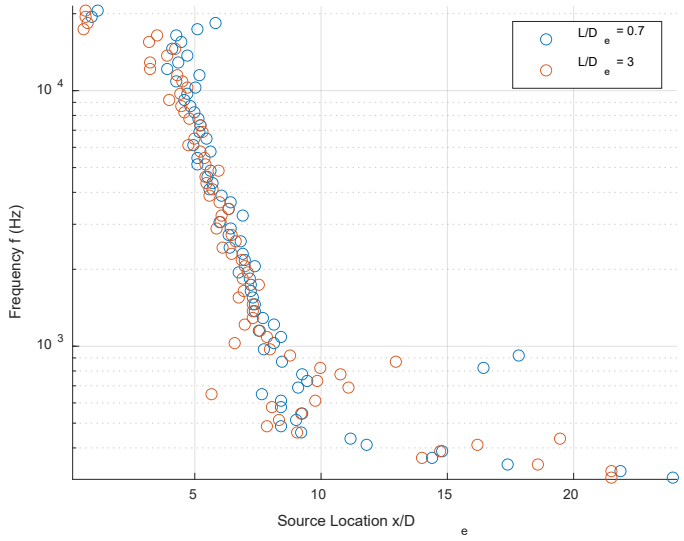

Figure 42. Comparison of source locations between L_e/D_e = 0.7 and 3.0. PR_1 = 1.39, ER = 1.07, T_{t1} = 500°F, one-twelfth octave band data.

Year – 3, the Gulfstream Nozzle

Nozzle Design

The third year of this project was devoted to designing, fabricating, installing and testing a set of nozzles that were physically different from those tested to date. They included a symmetrical nozzle and two forced mixers all of the same equivalent diameter and somewhat larger than those tested to date. The design of the dual-stream nozzles, assembly, and equivalent-diameter internal mixers are described in a recent paper by Clemens and Gavin (2024) of GAC. For a complete overview of the nozzle design and associated details, the reader is referred to this paper, though salient details will be reported here. The dual stream model obtained from GAC in April 2023 is designed for a bypass ratio of about 3.0, notably larger than that of the previous Year-1 academic nozzle designed by the ASDL. The assembly consists of a core duct, bypass duct, core nozzle, exhaust nozzle, and optional mixing-duct length spacers. The complete set of model parts is displayed in Figure 43.

The diameter or equivalent diameter of each primary nozzle is approximately D = 1.54 in., and the diameter of the final exhaust nozzle is D_e = 2.20 in. The diameter at the inlet of the mixing duct is D_{mix} = 2.80 in.

Figure 43. Model parts obtained from Gulfstream (Clemens & Gavin, 2024).

It is worth noting that unlike previously in which a single exhaust nozzle with length L_e/D_e = 0.7 was provided with spacers to increase the mixing-duct length to L_e/D_e = 1.0, 2.0, and 3.0, two distinct exhaust nozzles were designed For this study, the shorter L_e/D_e = 0.7 exhaust nozzle has a more rapidly convergent geometry than the L_e/D_e = 1.0 nozzle. In order to maintain uniform convergent geometry across nozzle configurations to isolate the effect of mixing-duct length alone, the L_e/D_e = 1.0 exhaust nozzle was used first in isolation to provide an L_e/D_e = 1.0. The exhaust mixing-duct length was then increased by attaching this nozzle to the end of one of two spacer ducts attached to the exit of the bypass duct. The nozzle at the end of the core duct is interchangeable, and Figure 43 shows the core duct and nozzle assembly using one of the two-lobed mixer nozzles provided.

All of the three core nozzles had the same exit area. Three-view diagrams of these nozzles taken from Clemens and Gavin (2024) are shown in Figure 44. The nozzle geometries consist of one baseline, axisymmetric nozzle and two lobed mixer nozzles, each with 10 lobes and 10 gullies. In all datasets corresponding to configurations using the axisymmetric mixer, the handle GAC23-AXI is used. The less aggressive of the two lobed mixers as shown in the center of Figure 44 is referred to as GAC23-SUN; while the more aggressive mixer with deeper lobes and gullies is referred to as GAC23-DAISY. For use in dual stream configurations a two-digit tag is included at the end of the configuration name to denote the mixing-duct length in tenths of L_e/D_e. For example, the handle GAC23-AXI-10 denotes a dual stream configuration using the baseline, axisymmetric core nozzle with an exhaust mixing-duct length of L_e/D_e = 1.0. The handle GAC23-SUN-00 would denote a dual stream configuration using the less aggressive SUN mixer with no exhaust nozzle but bypass flow still present. A single stream configuration using just the DAISY mixer nozzle alone with no bypass nozzle or secondary flow would be denoted as GAC23-DAISY. Figures 45 and 46 show various stages of the nozzle assembly installed in the GTRI anechoic chamber.

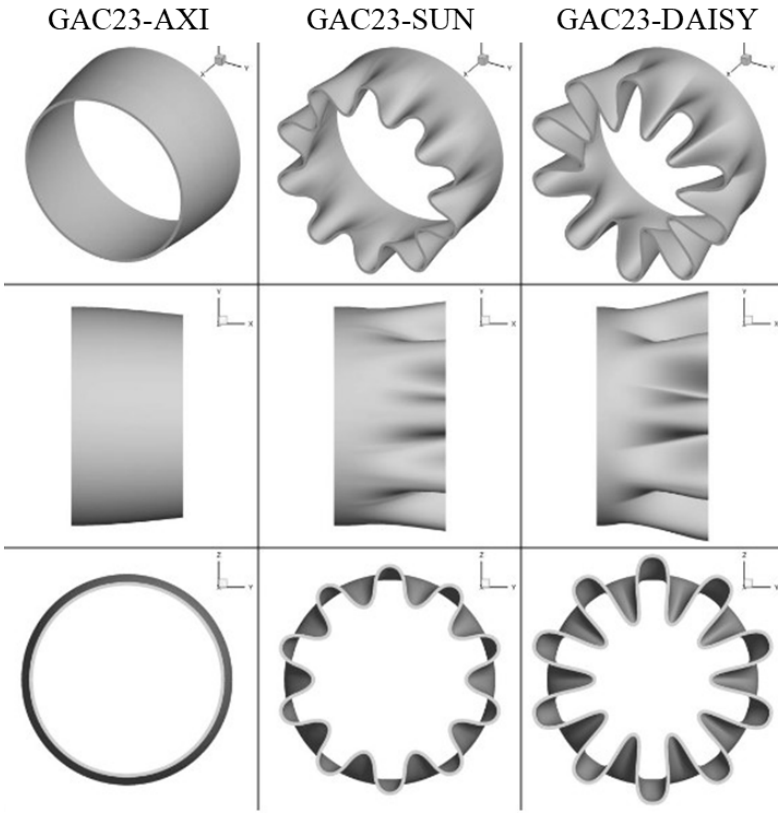

Figure 44. Three-view diagrams of core nozzles (Clemens & Gavin, 2024).

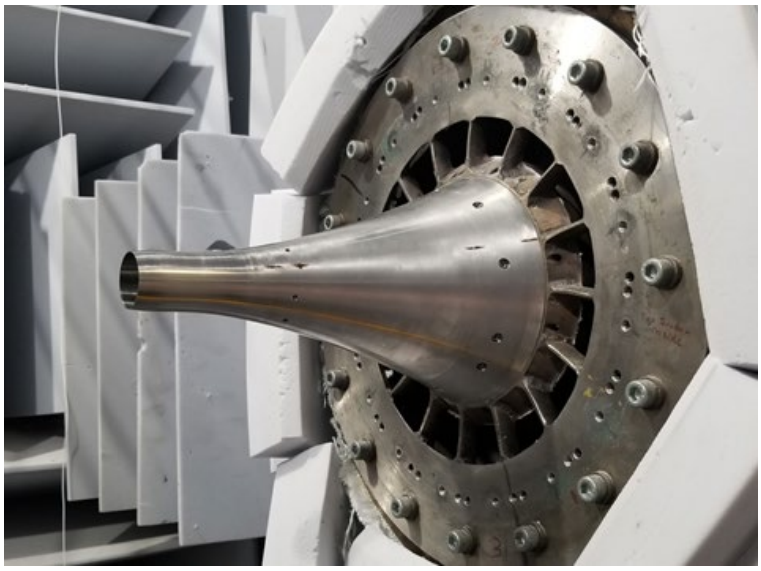

Figure 45. GAC primary nozzle with baseline axisymmetric nozzle (AXI) mixer installed in GTRI anechoic chamber.

(a) (b)

Figure 46. GAC nozzle assembly in GTRI static anechoic chamber with SUN internal mixer and bypass nozzle both (a) without exhaust nozzle and (b) with an exhaust nozzle of $L_e/D_e = 1.0$.

Single Stream Measurements

The acoustics and flowfields of jets issuing from lone lobed nozzles are complex in their own right even without the inclusion of secondary flow. In order to develop a more comprehensive understanding of the effects of lobed mixer nozzles on internally-mixed, dual-stream jets, it is important to first understand their behavior in isolation. As such, the same acoustic, PIV, schlieren, and source location measurements taken previously of dual-stream jets were acquired for each of the three core nozzles operated alone without any secondary nozzle or flow. The results discussed in the following sections highlight key characteristics of jets from the lobed nozzles that become important in dissecting their impact on the noise and flowfields of internally mixed jets. The facilities and methodologies by which these data were obtained are identical to those in previous sections and will not be repeated for the following sections.

Acoustic Measurements

Each of the three core nozzles – axisymmetric (AXI), SUN, and DAISY - were mounted in GTRI's anechoic chamber without the presence of the secondary duct (e.g., see Figure 45 showing the GAC23-AXI single stream configuration). Farfield acoustic measurements were taken along the same polar arcs as before with observation angles relative to the jet axis ranging from 30° to 110° in increments of 10°. During this testing, the jet Mach number M_j was varied from 0.5 to 1.0 in increments of 0.1 with the streams unheated ($T_{tj} \approx 60 - 70$°F). Figures 47 through 49 show the effect of both lobed nozzles on the noise produced by a single unheated jet at various observation angles. The effect of these mixers on the OASPL is shown in Figure 50. Data for the baseline, AXI nozzle is plotted in black, the SUN lobed nozzle is shown in blue, and the more aggressive DAISY lobed nozzle is shown in red. At the downstream polar observation angle $\theta = 30°$, the SUN mixer reduces jet noise at the peak frequency by approximately 5.5 dB while the DAISY mixer reduces it by about 10 dB relative to the AXI baseline. While more effective at reducing peak SPL, the DAISY mixer produces considerably more high-frequency noise. This is especially apparent at the sideline observation angle (Figure 49). This increase in high-frequency noise is less prevalent for the SUN mixer. A reduction in peak jet noise at the cost of enhanced higher frequency noise is to be expected of enhanced jet mixing devices. The callout at the bottom left of each figure is included to emphasize that the data are representative of the core nozzles operated in the single stream configuration. For reference, each core nozzle geometry is shown to the right of each figure with colored square boxes corresponding to the colors of their spectra on the plots.

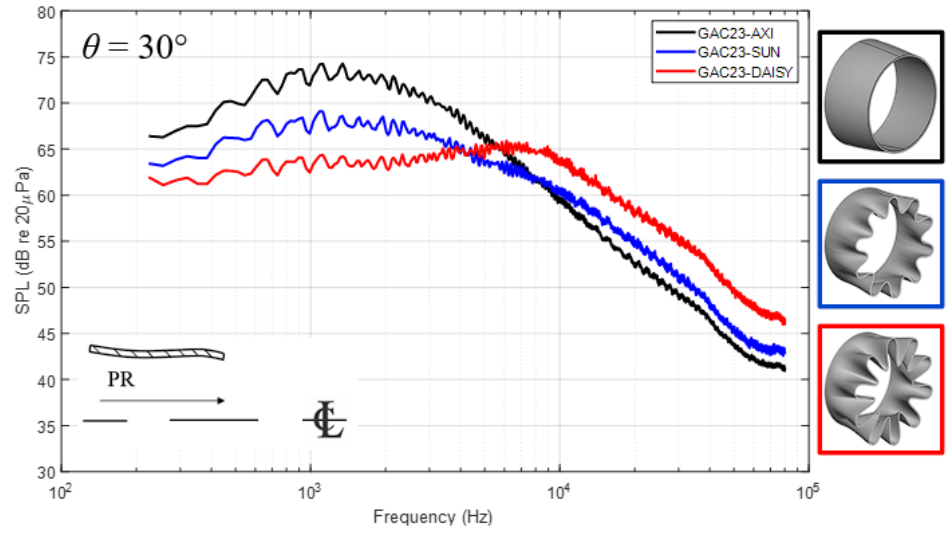

Figure 47. Effect of lobed nozzle on the noise from a single-stream jet. FAA GAC Project Model, D = 1.54 in. PR = 1.39 (M_j = 0.70), unheated, R = 12 ft, θ = 30°, Δf = 32 Hz, lossless.

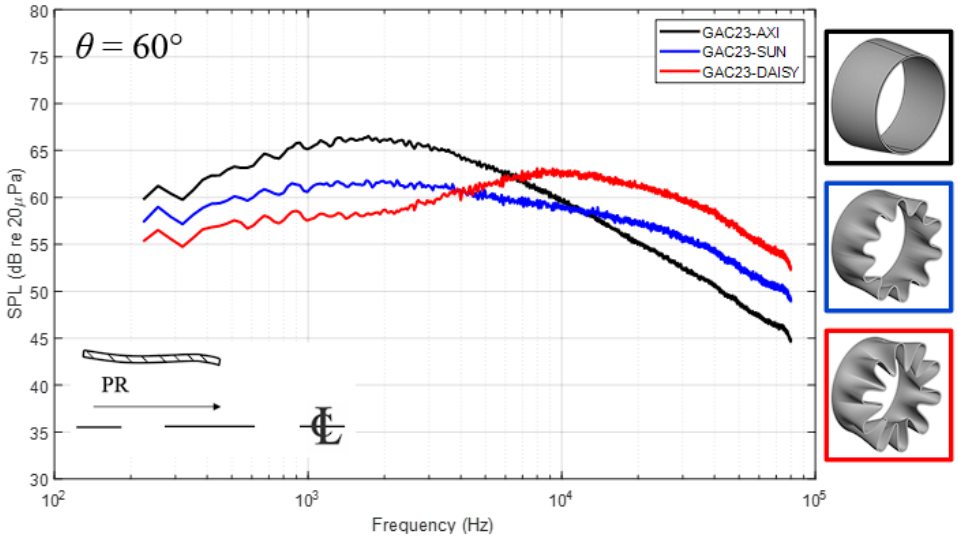

Figure 48. Effect of lobed nozzle on the noise from a single-stream jet. FAA GAC Project Model, D = 1.54 in. PR = 1.39 (M_j = 0.70), unheated, R = 12 ft, θ = 60°, Δf = 32 Hz, lossless.

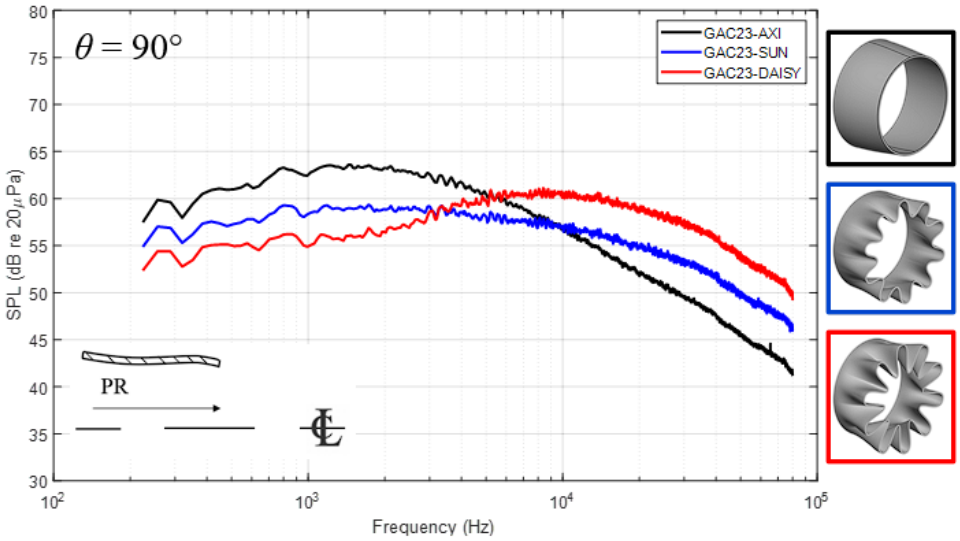

Figure 49. Effect of lobed nozzle on the noise from a single-stream jet. FAA GAC Project Model, D = 1.54 in. PR = 1.39 (M_j = 0.70), unheated, R = 12 ft, θ = 90°, Δf = 32 Hz, lossless.

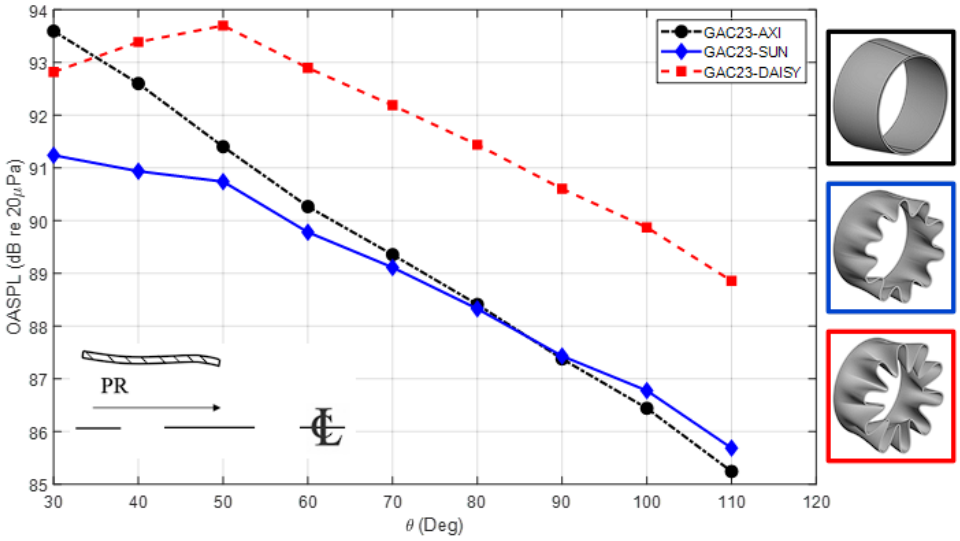

Figure 50. Effect of lobed nozzle on the overall noise from a single-stream jet. FAA GAC Project Model, D = 1.54 in. PR = 1.39 (M_j = 0.70), unheated, R = 12 ft, Δf = 32 Hz, lossless.

For the initial single stream testing with the lobed nozzles, all three polar arcs were employed to determine the directivity (if any) of jet noise produced by the lobed nozzles. Each arc was aligned differently relative to the orientations of the lobed as shown in Figure 51 which shows the alignment of the higher farfield (HF), middle farfield (MF) and lower farfield (LF) polar arcs relative to the lobes. Note that the lobed geometry shown is arbitrary and is not drawn to scale. As demonstrated in Figures 52 through 54 the farfield noise generated by these lobed nozzles at sideline angles is no more azimuthally dependent than that of the baseline AXI. This is also true for other polar observation angles.

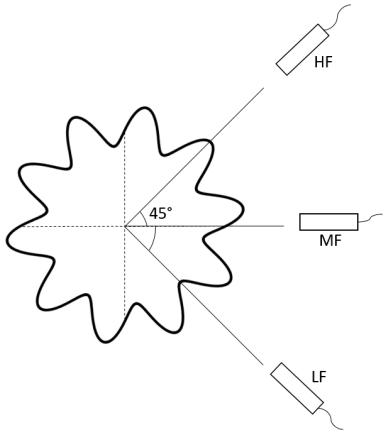

Figure 51. Microphone array orientation with respect to lobes.

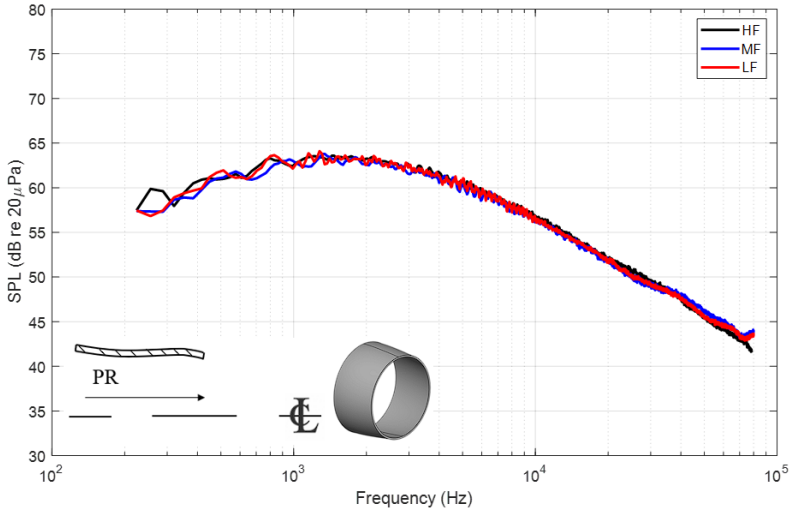

Figure 52. Azimuthal directivity of noise produced by axisymmetric (AXI) nozzle. FAA GAC Project Model, D = 1.54 in. PR = 1.39 (M_j = 0.70), unheated, R = 12 ft, θ = 90°, Δf = 32 Hz, lossless. HF: higher farfield, MF: middle farfield, LF: lower farfield, SPL: sound pressure level.

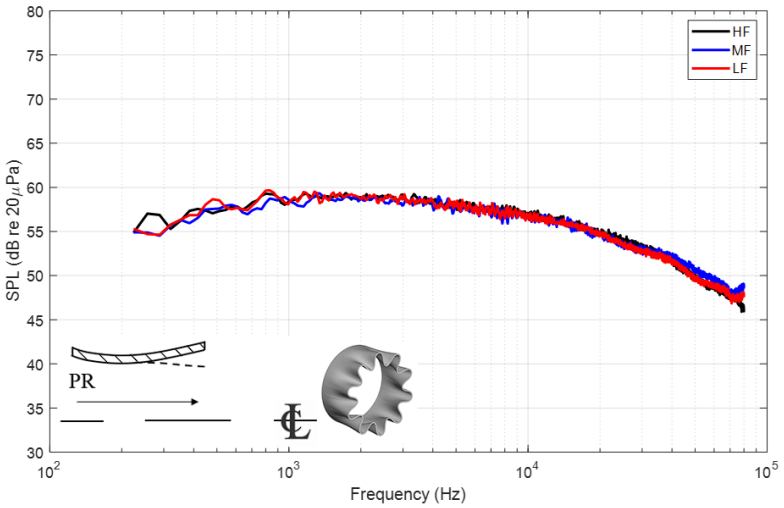

Figure 53. Azimuthal directivity of noise produced by SUN nozzle. FAA GAC Project Model, D = 1.54 in. PR = 1.39 (M_j = 0.70), unheated, R = 12 ft, θ = 90°, Δf = 32 Hz, lossless. HF: higher farfield, MF: middle farfield, LF: lower farfield, SPL: sound pressure level.

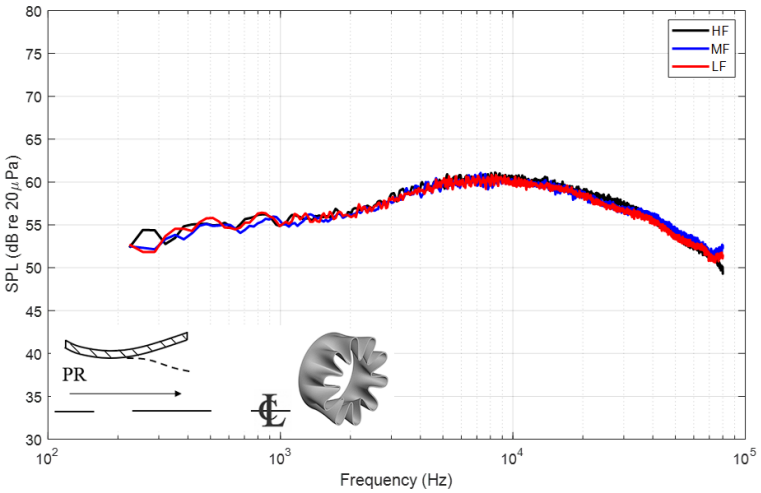

Figure 54. Azimuthal directivity of noise produced by DAISY nozzle. FAA GAC Project Model, D = 1.54 in. PR = 1.39 (M_j = 0.70), unheated, R = 12 ft, θ = 90°, Δf = 32 Hz, lossless. HF: higher farfield, MF: middle farfield, LF: lower farfield, SPL: sound pressure level.

The strong effect of the lobed mixers on jet noise observed at low polar angles (e.g., see Figure 47) suggests a stark difference in the nature of the large-scale turbulent structures between jets flowing from axisymmetric nozzles and those flowing from lobed mixer nozzles. This has become the focus of ongoing PhD student Larisch's thesis, which has revealed much about the nature of these lobed jets. One proposed model of jet noise given by the so-called two-source model by Tam et al. (1996, 2008) and Tam (2019) proposes that there are two distinct mechanisms by which jet noise is produced: one which pertains to large-scale turbulent structures (i.e., instability waves), which primarily radiates downstream to lower observation angles and one which pertains to fine-scale turbulent mixing, which radiates predominantly on the sideline. Tam et al. (1996, 2008) and Tam (2019) referred the source associated with the large-scale turbulence structures as the "F" spectrum and that associated with the fine-scale turbulence as the "G" spectrum. These labels are used in the following

figures also. The broadband noise produced by each component can be approximated using empirically-derived fits (Tam, 1996). Nance (2007), and Nance and Ahuja (2007, 2009) successfully showed that these two portions of jet noise can be isolated using a simple, coherence-based technique known as the three-microphone signal enhancement technique (Chung, 1977) by which the output power of a coherent signal at a given point may be separated from uncorrelated noise. An example of this decomposition is shown below in Figure 55 using the jet noise produced by the GAC23-AXI nozzle configuration at $PR = 1.69$ ($M_j = 0.90$), unheated at a polar observation angle of $\theta = 50°$. Here, the coherent portion of the jet noise spectrum is the component of noise associated with large-scale instability waves. A critical finding was made in that the jet noise spectra for the lobed mixer nozzles consist of a double-peaked coherent portion which can be closely approximated with two large-scale spectra as shown in Figure 56. The implications of this finding will become clearer in the following sections after we have presented the PIV and the source location data for the mixer nozzles.

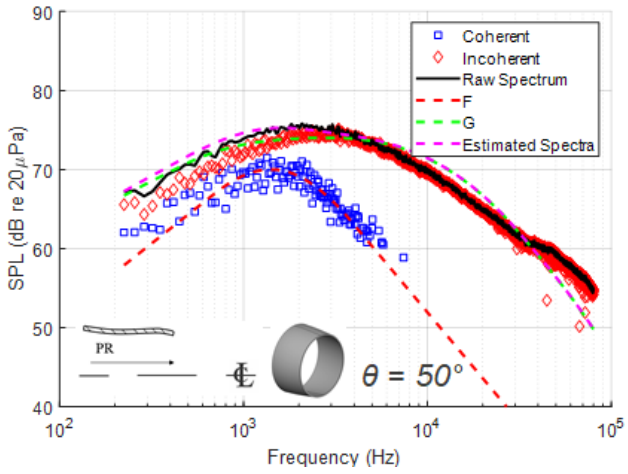

Figure 55. Estimated coherent and uncorrelated jet noise levels from axisymmetric nozzle measured at θ = 50° with fitted F and G similarity spectra. PR = 1.69, Tt ≈ 60°F, R = 12 ft, Δf = 32 Hz, lossless. SPL: sound pressure level.

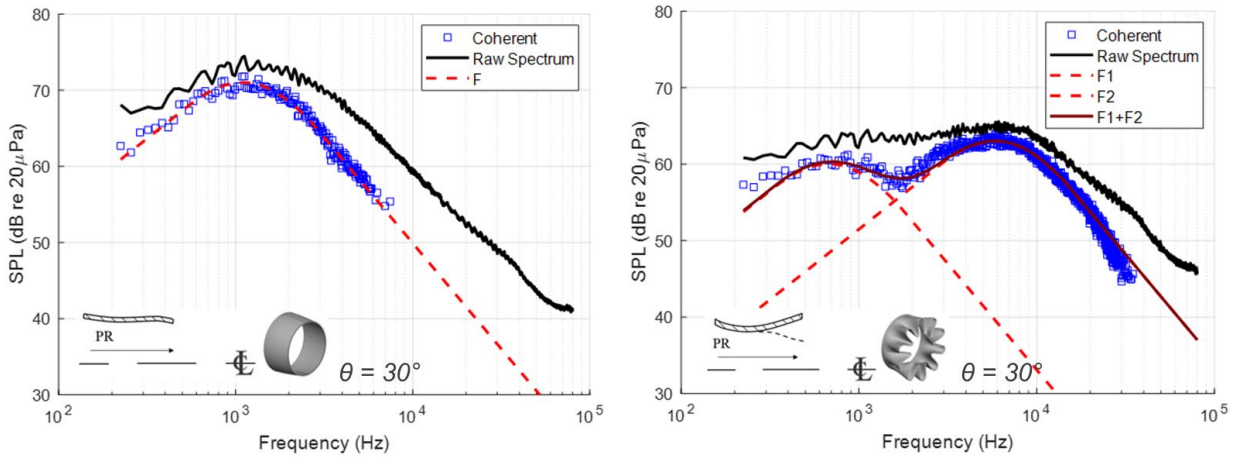

Figure 56. Estimated coherent jet noise levels from (a) axisymmetric and (b) lobed nozzles measured at θ = 30° with fitted *F* similarity spectra. PR = 1.39, $T_t \approx 60°F$, R = 12 ft, $\Delta f = 32$ Hz, lossless. SPL: sound pressure level.

PIV Measurements

PIV data were acquired in the same manner as before for each of the three primary nozzles at the same unheated conditions outlined in the previous section. A higher number of samples (N = 750) were acquired at two conditions - *PR* = 1.39 (M_j = 0.70) and *PR* = 1.69 (M_j = 0.90) – in order to accurately resolve turbulence statistics. Otherwise, a smaller sample size of N = 200 was sufficient to capture the mean flow. For the lobed nozzles, PIV data were acquired twice for each condition: once with the laser sheet aligned with lobes and once with the laser sheet aligned with gullies. As is to be expected from the differences seen in farfield noise, the flowfields of the lobed jets look wildly different from those of the axisymmetric nozzle. Figure 57 shows 2D plots of mean axial velocity, axial turbulence intensity, and radial turbulence intensity of the axisymmetric nozzle at *PR* = 1.69 and is not unlike those shown for the unity ER, unheated somewhat smaller axisymmetric jet in Figure 24a or Figure 24b.

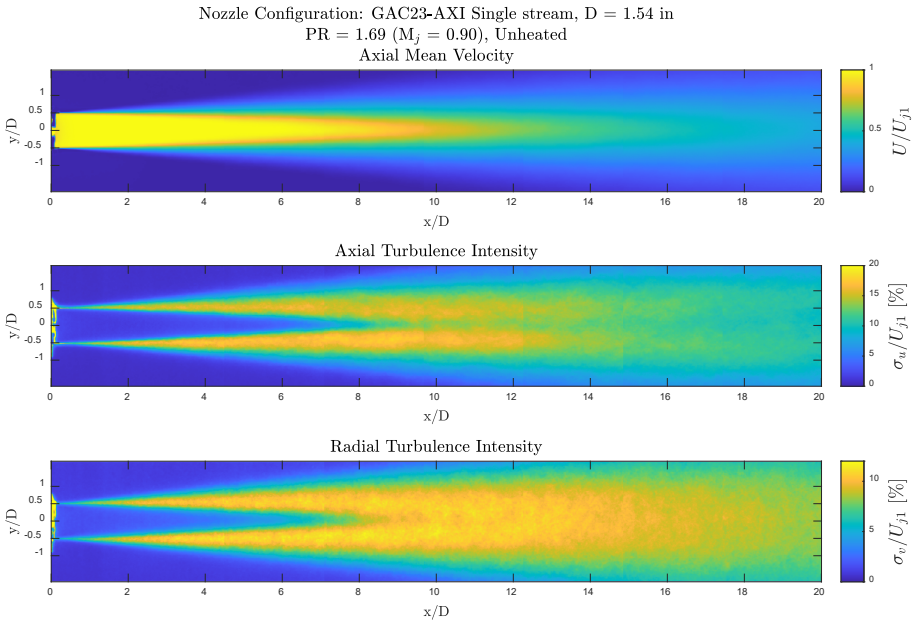

Figure 57. Two-dimensional mean velocity and turbulence intensity plots. GAC23-AXI configuration, *PR* = 1.69 (M_j = 0.90), unheated, N = 750 image pairs.

Figure 58 shows the same 2D plots but using the GAC23-DAISY configuration at *PR* = 1.39. Figure 58a shows measurements taken with the laser sheet aligned with lobes and Figure 58b shows those taken aligned with gullies. Very shortly downstream from the nozzle exit there exists a highly turbulent mixing region from an x/D of about 0.5 to 3. Beyond this region, the flowfield resembles that of a smaller, axisymmetric jet. A potential core still exists in the center as evidenced by the mean velocity plots but is shorter than that of the axisymmetric jet shown in Figure 57. A comparison of the centerline velocity distributions of the AXI and DAISY nozzles in Figure 59 reveals an approximately 40% reduction in the length of the potential core while the SUN mixer only slightly reduces the length of the potential core. After the mixing region, the centerline velocity of jets from both lobed nozzles decays following the distribution of the axisymmetric nozzle.

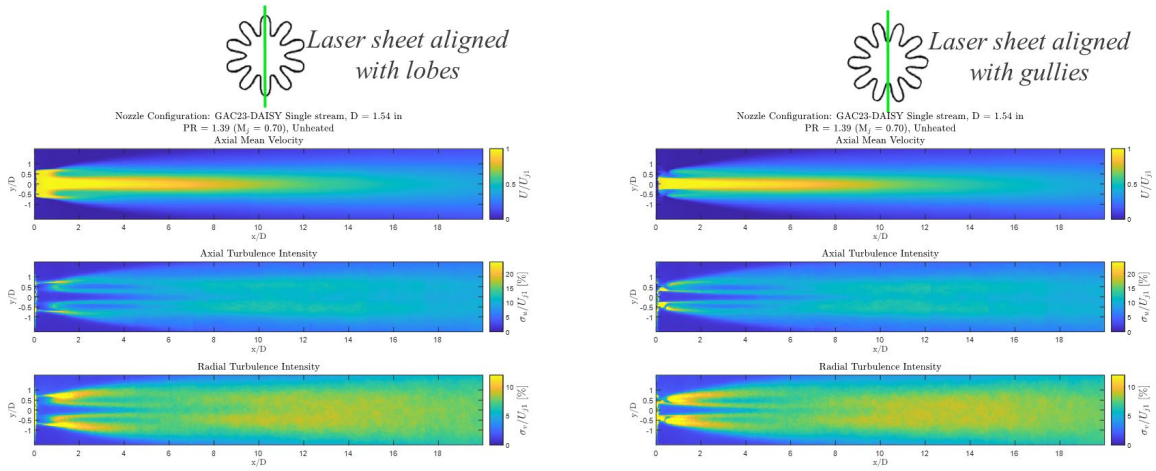

Figure 58. Two-dimensional mean velocity and turbulence intensity plots. GAC23-DAISY configuration (a) lobe aligned and (b) gully aligned. D = 1.54 in., *PR* = 1.39 (M_j = 0.70), unheated, N = 750 image pairs.

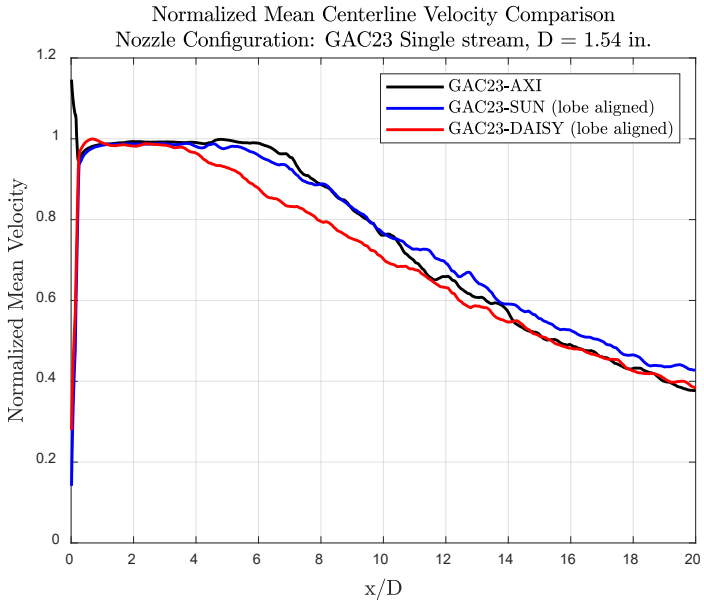

Figure 59. Centerline mean velocity distribution of jets from AXI, SUN, and DAISY nozzles. D = 1.54 in., *PR* = 1.53 (M_j = 0.80), unheated, N = 200 image pairs.

One remaining feature of note in the flowfield from the lobed nozzles is the existence of tiny potential cores issuing from the individual lobes. This can be observed upon close examination of the mean velocity field near the nozzle exit in Figure 58a wherein the laser sheet is aligned with the lobes. Just downstream of a lobe (at about y/D = 0.6 in the figure) one can see a streak of yellow which terminates around an axial position of x/D = 1.5. These tiny jets are better visualized in Figure 60, which shows profiles of mean axial velocity at various x/D near the nozzle. The curves in black are data taken with the laser sheet aligned with lobes while the curves in red are data taken with the laser sheet aligned with gullies. Outside the main potential core near the center of each profile there are peaks in axial velocity at about y/D = ±0.6 which

decay rapidly, disappearing into the shear layer about three diameters downstream from the nozzle exit. Interestingly, there are also local peaks in velocity at these same locations for the gully-aligned measurements. This may be due in part to entrainment of the flow downstream from a gully by adjacent flow issuing from lobes and may also be due to vortical flow from the lobes dumping axial momentum into the dead space downstream from a gully. This same observation is also made of the SUN nozzle.

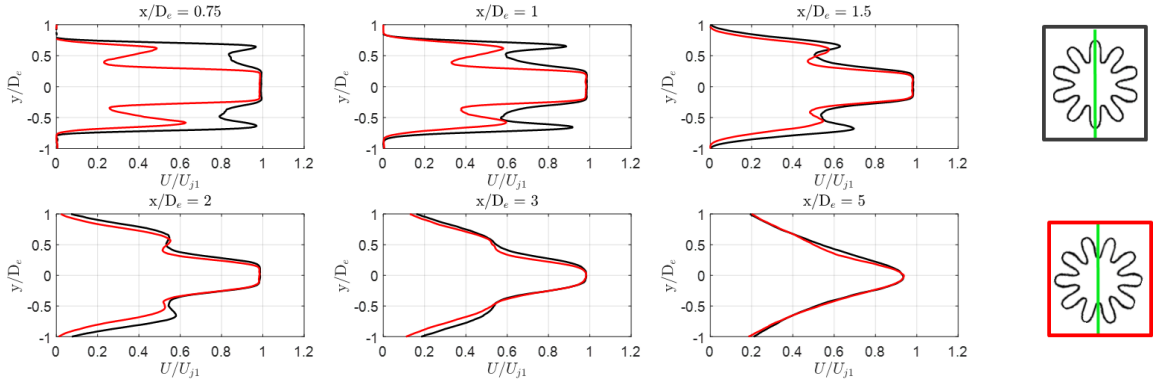

Figure 60. Profiles of mean axial velocity at various x/D. GAC23-DAISY configuration. Lobe aligned measurements shown in black and gully aligned measurements shown in red, D = 1.54 in., *PR* = 1.39 (M_j = 0.70), unheated, N = 750 image pairs.

Stereoscopic PIV measurements acquired as part of a separate research effort at GTRI capture this effect more clearly. The visualizations below are of flow from the SUN and DAISY nozzles captured in a plane perpendicular to the jet axis at an axial distance of x/D = 0.9. Note that the inclusion of these visualizations in the present context is mainly for illustrative purposes. There will be no quantitative treatment of these data in the present work. The key takeaway is the existence of 10 small jets – one for each lobe - which pinch off from the central flow. Knowledge of these features of the lobed nozzles is critical in discussion of their effects on jet noise and acoustic source distribution.

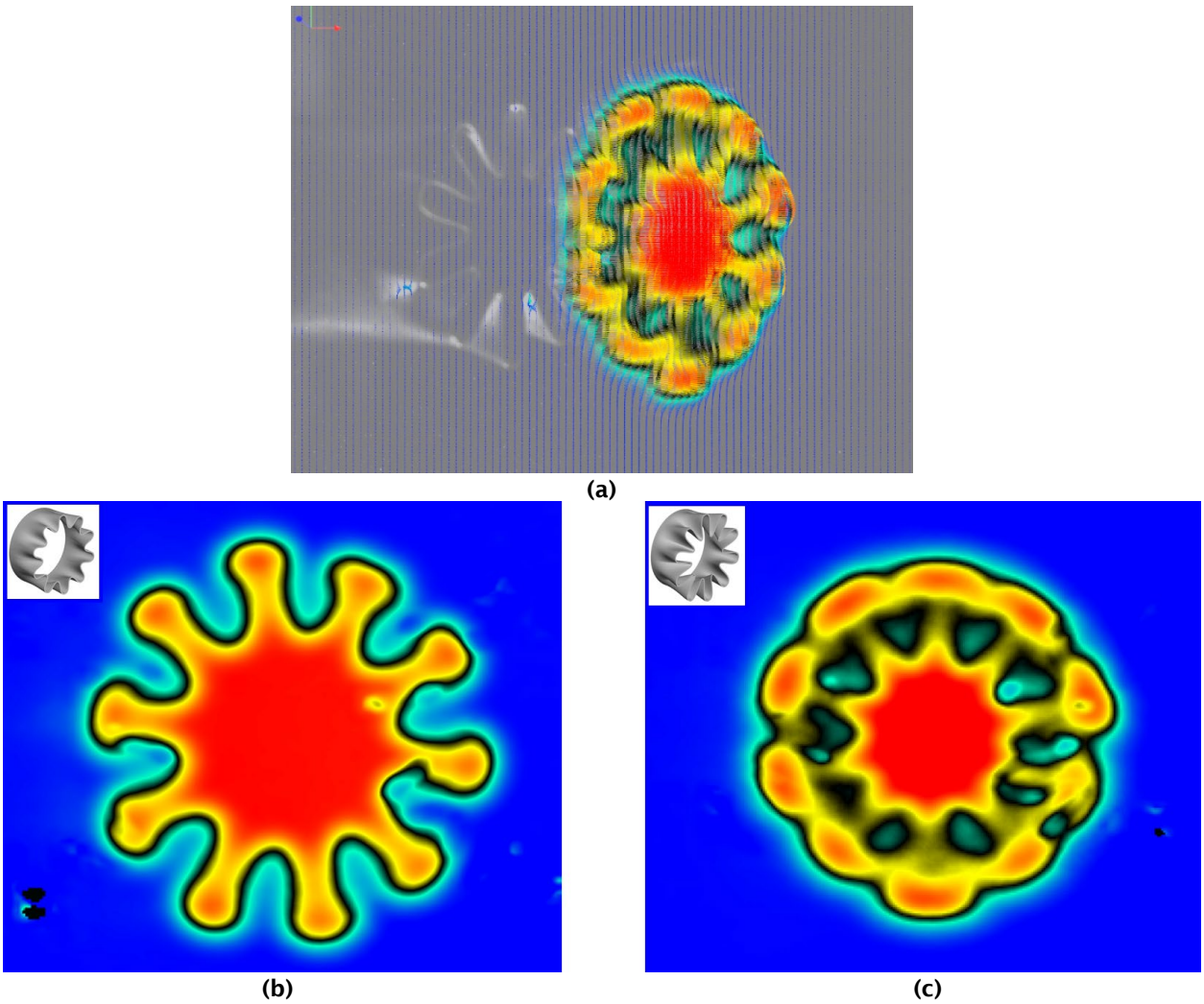

Figure 61. Example stereo-PIV visualizations showing the existence of jets from the lobes pinching off from the central flow, (a) image from one camera showing flow in relation to nozzle location, (b) flow from SUN nozzle and (c) flow from DAISY nozzle. M_j = 0.60, unheated. N = 750 image pairs.

Source Location Measurements

Source location data for each of the primary nozzle caps (AXI, SUN, and DAISY) were acquired without use of the secondary nozzle. For each primary nozzle, the jet was operated at a variety of unheated conditions with ideally-expanded jet Mach numbers (M_j) ranging from 0.5 to 1.0. The noise source distribution data from the AXI nozzle collapse based on a Strouhal number *St* formed using the exit diameter *D* (approximately 1.54 in.) and the fully-expanded jet velocity U_j as shown in Figure 62. Note that all source location data shown depict the locations of the peak noise source – as opposed to the centroid – for a given frequency. These data follow the typical pattern of a round nozzle and fit the empirical curve for the source distribution of a round jet found in jet noise literature (Breen & Ahuja, 2019).

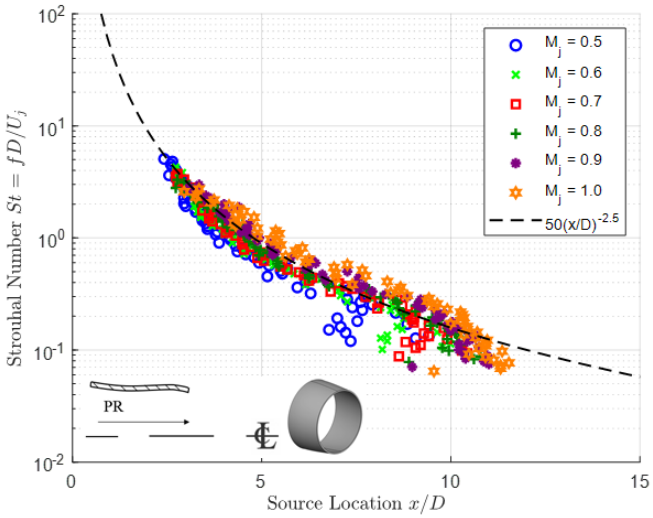

Figure 62. Source location of subsonic jet from AXI baseline nozzle. D = 1.54 in. Various M_j, unheated, one-twelfth octave band data.

The above experiment was then repeated using both lobed mixer nozzle designs, the results of which are shown in the Figures 63 and 64. It is observed that the rapid mixing region near the exit of the nozzle noted in the previous section produces a group of high-frequency noise sources, with the downstream portion (x/D from 7-15) of the noise source distribution loosely resembling that of an unmixed circular jet as shown above in Figure 62. As the jet Mach number is increased, these high-frequency sources seem to drift noticeably further downstream. These higher-frequency sources may in part be explained by the existence of the pinched jets found downstream of each lobe mentioned previously. These smaller jets would produce noise at much higher frequencies and terminate very rapidly which could explain the tight cluster of high-frequency noise sources seen in Figures 63 and 64.

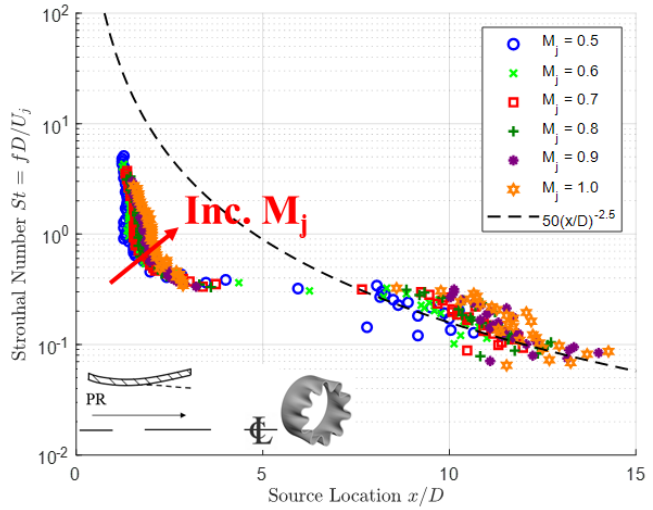

Figure 63. Source location of subsonic jet from SUN mixer nozzle. D = 1.54 in. Various M_j, unheated, one-twelfth octave.

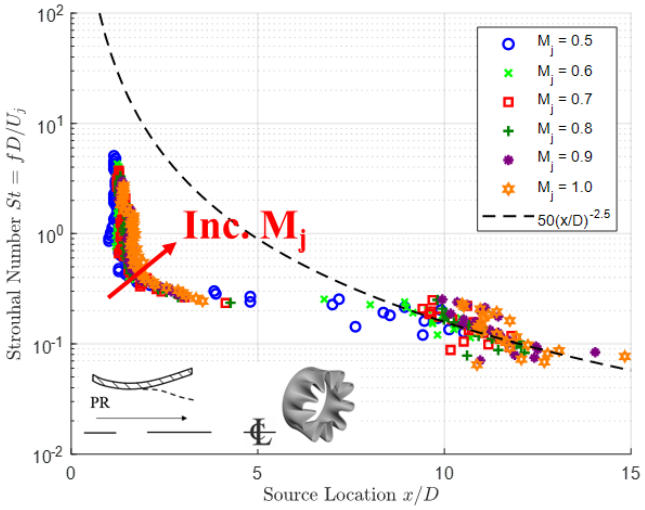

Figure 64. Source location of subsonic jet from DAISY mixer nozzle. D = 1.54 in. Various M_j, unheated, one-twelfth octave.

Now we can return to explain the double hump in Figure 56. Previous studies into jet noise reduction through mixing enhancement would suggest that fine-scale turbulent mixing is the dominant source of noise from a lobed jet, and that the noise produced by coherent large-scale structures is almost entirely suppressed. We have shown for the first time that for a forced lobed mixer nozzle this is not the case, and that there exists a second source of highly coherent, high-frequency noise not attributable to uncorrelated fine-scale turbulent mixing. Figure 56 shows the estimated coherent noise portions of the jet noise spectrum measured from a Mach 0.70 jet obtained through implementation of the three-microphone method for the round AXI and lobed SUN nozzles. Close to the jet axis the contribution to farfield noise from the coherent portion is substantial. Interestingly, we are able to recover two pronounced peaks in the coherent portion of jet noise measured from both lobed mixer nozzles. As evidenced by the dashed curves, the shape of this coherent noise spectrum may be precisely fit to the sum of two *F* spectra. These large-scale similarity spectra are each prescribed a peak amplitude *A* and frequency *f* such that their sum *F_1 + F_2* (obtained via dB addition) fits the estimated coherent noise portion via the method of least squares. To the authors' knowledge, this phenomenon has never been observed in existing jet noise literature and serves as the first concrete explanation for the increase in high-frequency jet noise produced by lobed jets.

Dual Stream Measurements

With the discussion of single stream measurements complete, the focus now changes to the discussion of results obtained using the Gulfstream models in dual stream configurations. All results presented from this point on involve the use of the secondary nozzle with bypass flow present. Testing was done with each of the three core nozzles and with two mixing-duct lengths: L_e/D_e = 1.0 and L_e/D_e = 3.0. It is again noted that while two exhaust nozzles were obtained from GAC – one with length L_e/D_e = 0.7 and one with length L_e/D_e = 1.0 – only the L_e/D_e = 1.0 nozzle with the less rapid convergent geometry was used.

Acoustic Measurements

Effect of lobed mixers: The conditions matrix for which dual stream measurements were taken with unheated and heated core flows are shown in Figures 65a and 65b, respectively.

Unheated (T_{t1} = ~60 °F)		Primary Mach					
		0.5	0.6	0.7	0.8	0.9	1
Secondary Mach	0.4	■					
	0.5	■					
	0.6	■	■				
	0.7			■	■	■	■
	0.8			■	■	■	■
	0.9			■	■	■	■
	1			■	■	■	■
ER	1.04			■		■	
	1.07			■		■	

(a)

Heated (Tt1 = 500 °F)		Primary Mach					
		0.5	0.6	0.7	0.8	0.9	1
Secondary Mach	0.4	■					
	0.5	■	■				
	0.6	■	■				
	0.7		■	■			
	0.8			■	■		
	0.9				■	■	
	1					■	■
ER	1.04			■		■	
	1.07			■		■	

(b)

Figure 65. Conditions matrices for (a) unheated and (b) heated core operating conditions. Green indicates an operating condition at which data was acquired.

The use of the forced mixers in conditions with an unheated primary stream fails to produce an appreciable reduction in jet noise, if any. Without a significant velocity and/or temperature difference between the core and bypass streams there is little-to-no internal mixing to take place that would reduce external jet noise. The spectra in Figure 66 show the jet noise measured at the ϑ = 90° sideline polar observation angle at the PR_1 = 1.39 (M_{j1} = 0.70), ER = 1.00, unheated operating condition. Similar to as was done previously, the jet noise spectrum corresponding to the dual stream configuration utilizing the axisymmetric core nozzle is shown as a black curve, while data taken using the SUN and DAISY nozzles are shown as blue and red curves respectively. The callout in the bottom left of the figure is meant to emphasize that the jet noise spectra shown are of a dual-stream, internally-mixed jet.

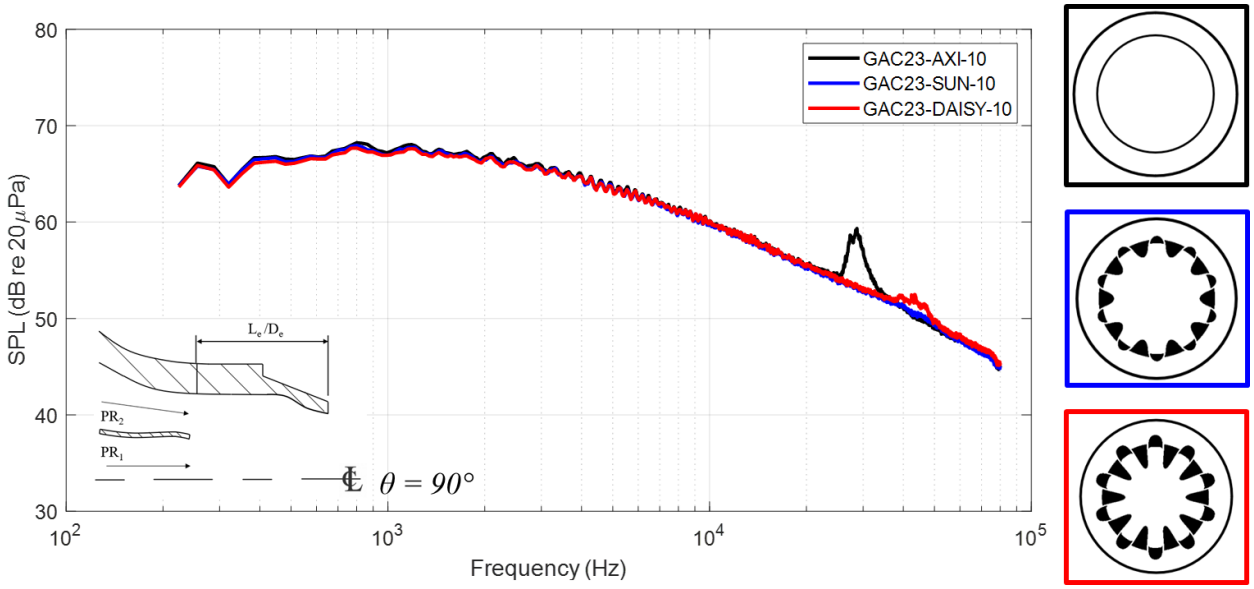

Figure 66. Noise generated from dual-stream, unheated jet from GAC project model at θ = 90° sideline polar observation angle. L_e/D_e = 1.0, PR_1 = 1.39, ER = 1.00, T_{t1} = 60°F, R = 12 ft, Δf = 32 Hz, lossless. SPL: sound pressure level.

While there is no change in the levels of external jet noise observed here, there is one noticeable difference in the spectra shown above. The high-frequency spectral hump observed in several jet noise spectra acquired thus far is hypothesized to be the acoustic signature of vortex shedding from the core nozzle lip, a phenomenon also observed in the Year-1 academic baseline nozzles. The Strouhal number, calculated from the velocity of the core nozzle exit obtained from isentropic relations, the core nozzle trailing edge thickness, and the peak frequency, aligns closely with the *St* = 0.2 trend observed in vortex shedding literature (Ramsey et al., 2022a). The cause of this shedding in dual-stream, model-scale nozzles and its associated noise is the subject of ongoing academic study by PhD student Larisch and recent PhD graduate Ramsey. At additional industry-relevant extraction ratios just above unity (e.g., ER = 1.04, 1.07) the farfield spectra are also nearly identical across the various mixers.

In order to observe any noticeable differences in the jet noise produced using the various nozzle caps for an unheated core stream, there must be a significant velocity difference between the two streams. The spectra in Figure 67 are taken from the most extreme unheated condition evaluated, namely, PR_1 = 1.89 (M_{j1} = 1.00), PR_2 = 1.39 (M_{j2} = 0.70), T_{t1} = ~60°F. Comparing the AXIS and SUN mixers, a decrease in peak jet noise of approximately 1.3 dB is observed at low polar angles (θ = 30°) and 0.7 dB at the sideline (θ = 90°). Likewise, comparing the AXIS and DAISY mixers yield similar results, with a decrease in peak jet noise of about 2.7 dB at low polar angles and 1.5 dB at the sideline. It is observed that the SUN mixer reduces the overall noise level by at most nearly 1.3 dB despite the increase in high-frequency noise at lower polar angles while the DAISY mixer shows a 2.2 dB reduction. The high-frequency, coherent noise sources observed in lobed jets are being investigated as part of PhD student Larisch's thesis to contribute to the understanding of noise suppression using forced mixers. As the observation angle shifts upstream, the noted decreases in peak jet noise are overtaken by the heightened levels of high-frequency noise due to enhanced mixing levels.

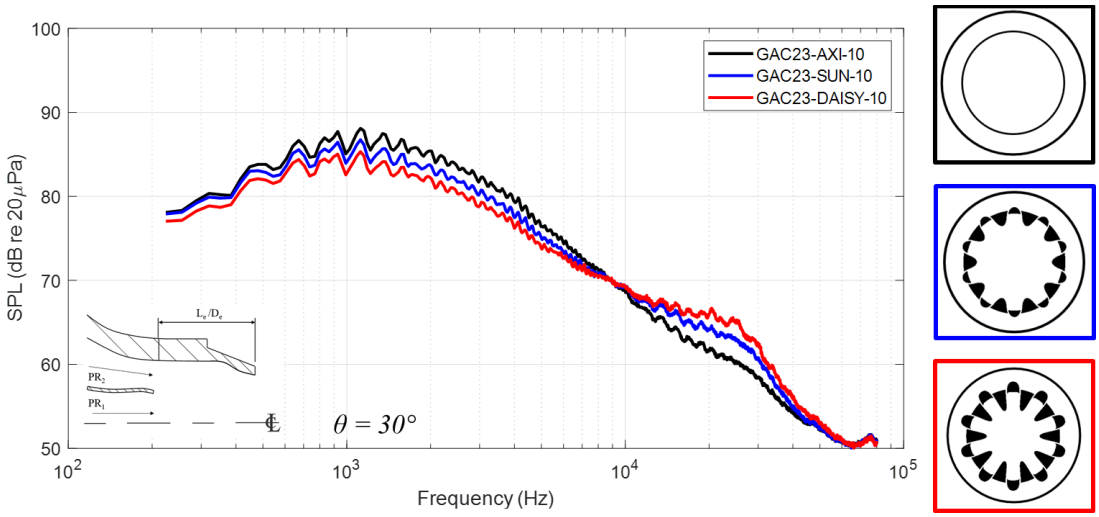
GAC23-AXI-10
GAC23-SUN-10
GAC23-DAISY-10
SPL (dB re 20 μPa)
Frequency (Hz)
θ = 30°
PR2
PR1

(a)

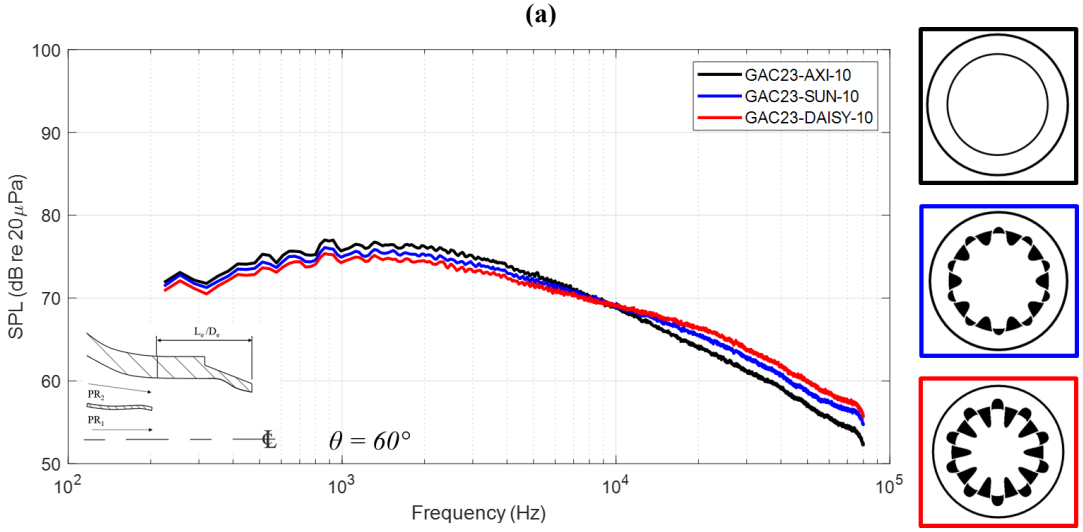
GAC23-AXI-10
GAC23-SUN-10
GAC23-DAISY-10
SPL (dB re 20 μPa)
Frequency (Hz)
θ = 60°
PR2
PR1

(b)

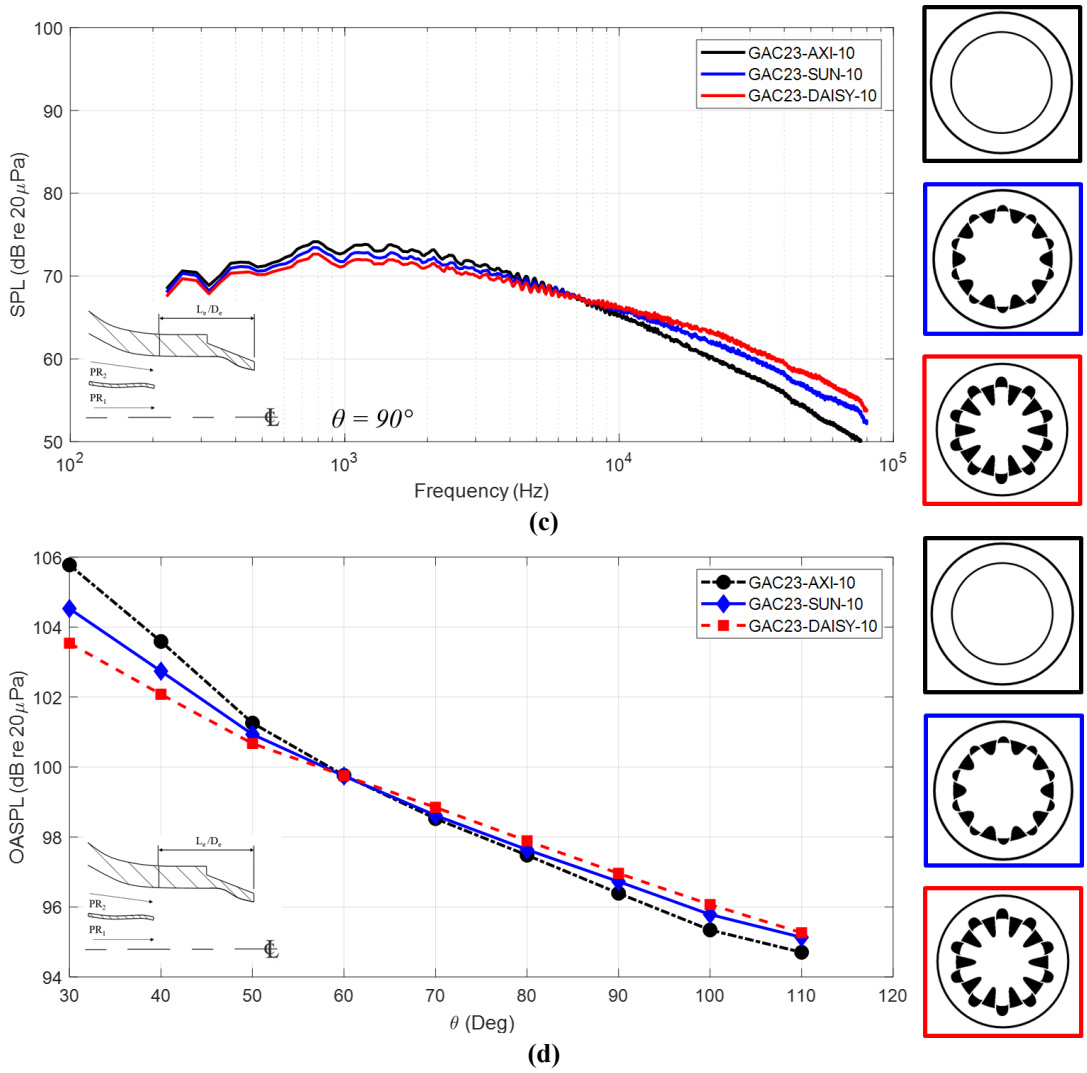

Figure 67. Noise generated from dual-stream, unheated jet from GAC project model at θ = (a) 30°, (b) 60°, and (c) 90° polar observation angles and (d) overall sound pressure level (OASPL). L_e/D_e = 1.0, PR_1 = 1.89, PR_2 = 1.39, T_{t1} = 60°F, R = 12 ft, Δf = 32 Hz, lossless. SPL: sound pressure level.

Shown in the figures below are representative jet noise spectra showing the effects of each of the lobed mixers on the noise from an internally mixed, dual-stream jet with a heated core stream. A consistent mixing-duct length of L_e/D_e = 1.0 is used to compare the jet noise of mixer nozzles with that of the axisymmetric nozzle. At the aft-most observation angle – the spectra for which are shown in Figure 68a - where the lobed mixers have the most impact, the SUN mixer reduces the level of jet noise at the peak frequency by approximately 2.6 dB relative to the baseline AXI for the condition shown (PR_1 = PR_2 = 1.39, M_{j1} = M_{j2} = 0.70). The more intense DAISY lobed mixer has deeper lobes and gullies and reduces the peak SPL by 3.7 dB. The sideline observation spectra shown in Figure 68c reveals a decrease in peak SPL of about 1.2 dB for each of the lobed mixers. A frequent characteristic of mixing-enhancement devices for dual-stream jets is a decrease in peak SPL at the cost of an increase in high-frequency noise. While the DAISY mixer performs better at decreasing jet noise at the peak frequency – especially at aft polar observation angles – there is a noticeable increase in high-frequency noise beyond about 8 kHz or so. However, the SUN mixer which provides similar noise reduction benefits at higher polar angles does not produce an increase in high-frequency jet noise relative to the axisymmetric baseline primary nozzle.

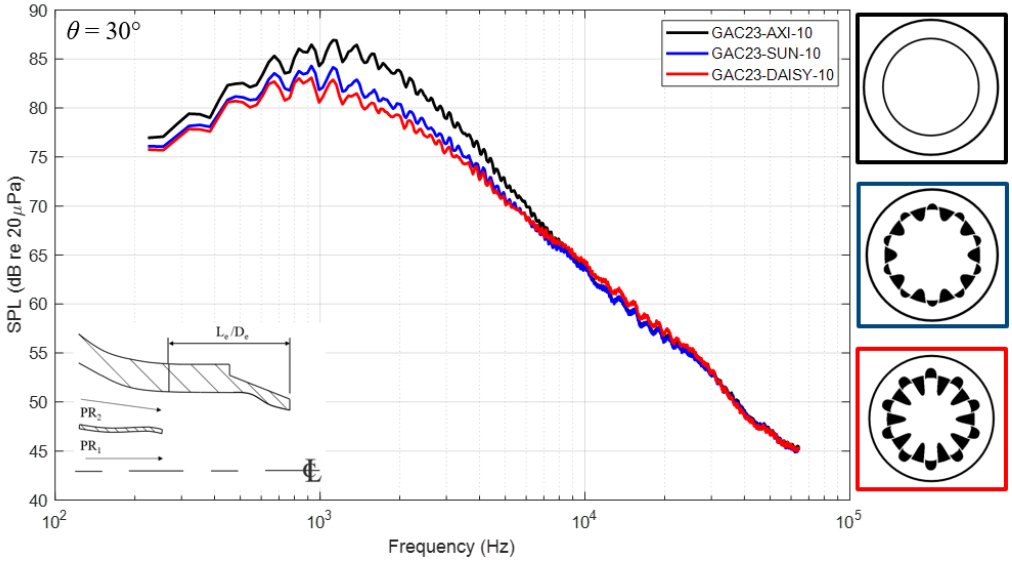
θ = 30°
GAC23-AXI-10
GAC23-SUN-10
GAC23-DAISY-10
SPL (dB re 20 μPa)
Frequency (Hz)
L_e/D_e
PR_2
PR_1

(a)

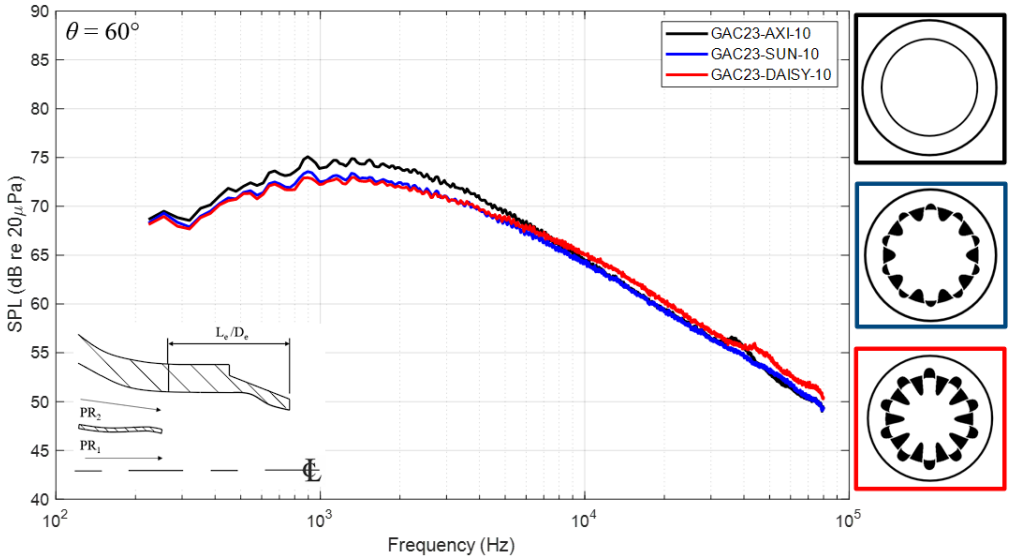
θ = 60°
GAC23-AXI-10
GAC23-SUN-10
GAC23-DAISY-10
SPL (dB re 20 μPa)
Frequency (Hz)
L_e/D_e
PR_2
PR_1

(b)

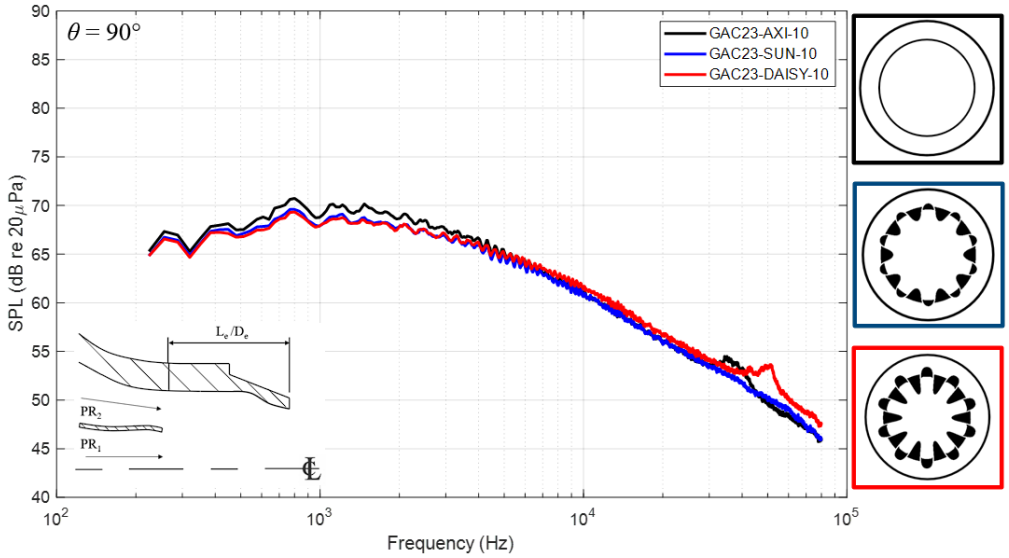

(c)

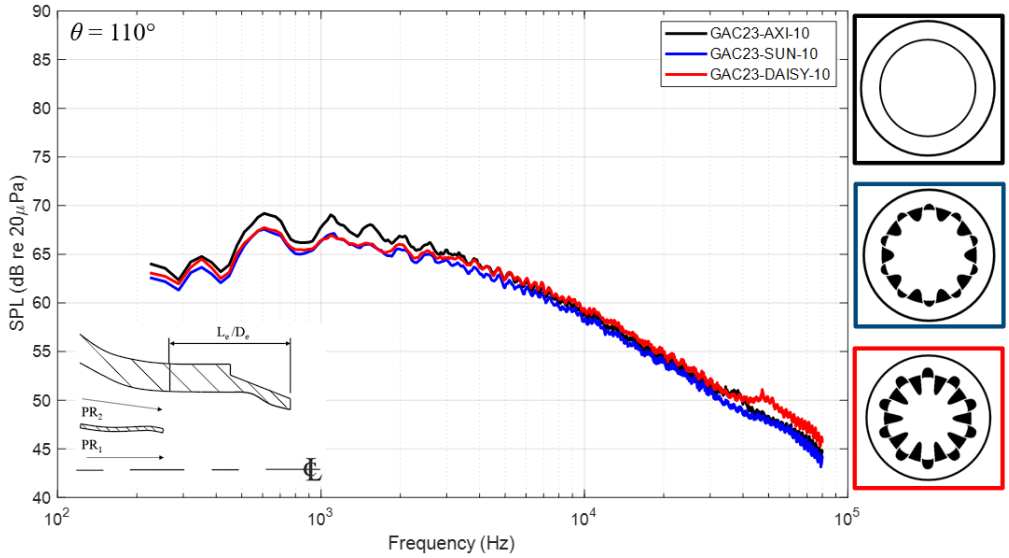

(d)

Figure 68. Effect of lobed nozzle on the noise from an internally mixed, dual-stream jet. FAA GAC Project Model, D_e = 2.20 in. L_e/D_e = 1.0, PR_1 = 1.39 (M_{j1} = 0.70), PR_2 = 1.39 (M_{j2} = 0.70), T_{t1} = 500°F, R = 12 ft, θ = a) 30°, b) 60°, c) 90°, d) 110°, Δf = 32 Hz, lossless. SPL: sound pressure level.

Overall noise level measurements (Figure 69) show the enhanced effect of the DAISY mixer at lower polar angles compared to the less-aggressive SUN mixer. For the lower pressure-ratio case shown in Figure 69a both mixers reduce or equate the overall noise level across all polar observation angles relative to the AXI baseline. At higher pressure-ratios (e.g., Figure 69b) it is observed that the SUN mixer maintains a decrease in overall noise everywhere but the excess high-frequency noise produced by the DAISY mixer leads to a slight increase in overall noise at sideline and upstream polar angles.

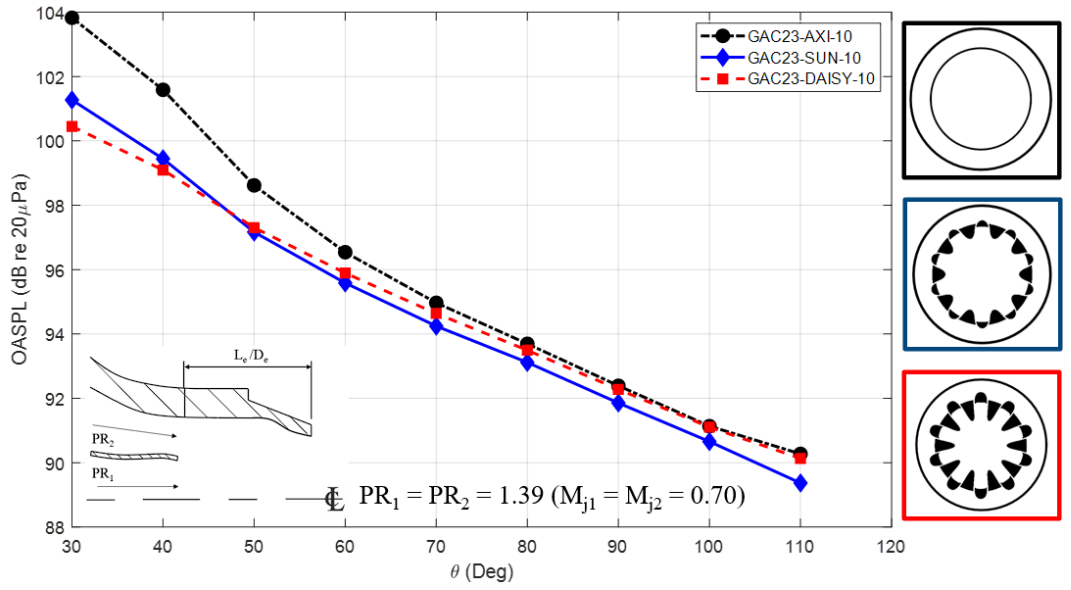

(a)

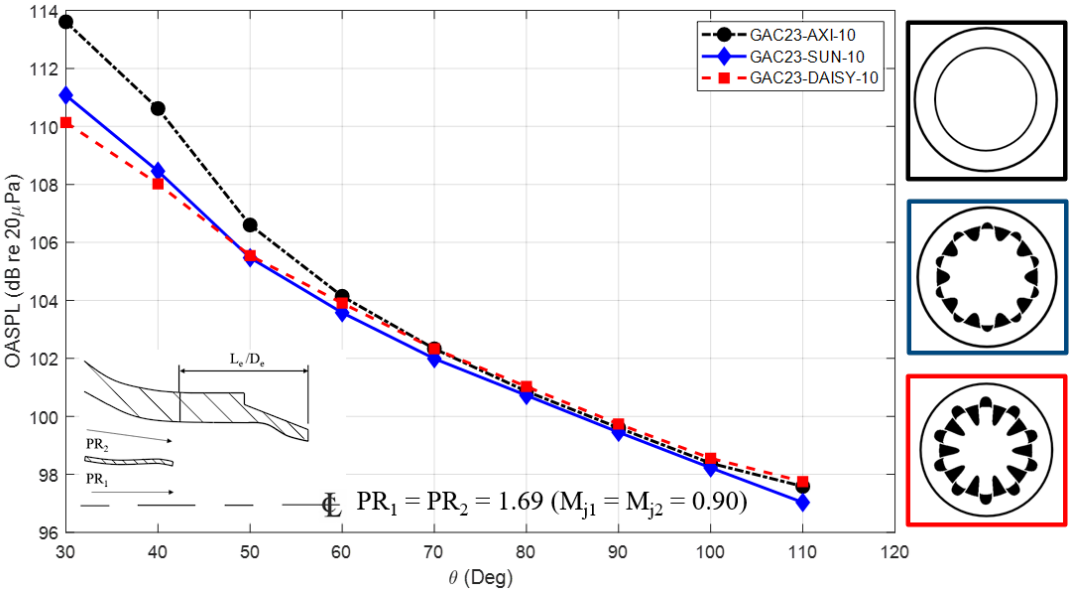

(b)

Figure 69. Effect of lobed nozzle on the overall noise from an internally mixed, dual-stream jet. FAA GAC Project Model, D_e = 2.20 in. L_e/D_e = 1.0, a) PR_1 = 1.39 (M_{j1} = 0.70), PR_2 = 1.39 (M_{j2} = 0.70) and b) PR_1 = 1.69 (M_{j1} = 0.90), PR_2 = 1.69 (M_{j2} = 0.90), T_{t1} = 500°F, R = 12 ft, Δf = 32 Hz, lossless. OASPL: overall sound pressure level.

Effect of increasing the mixing-duct length: The data shown above was restricted to $L_e/D_e = 1.0$. the effect of increasing the mixing duct length will now be discussed. Also, as there is little to no effect by the mixer nozzles on the noise produced by the dual stream jet with an unheated core, and since the effect of mixing-duct length on jet noise for an unheated core is treated in the discussion of the results from the Year-1 academic nozzle, only heated core results are presented and discussed here. The set of figures below show the effects of increasing the mixing-duct length for PR_1 = 1.39 (M_{j1} = 0.70), PR_2 = 1.39 (M_{j2} = 0.70), T_{t1} = 500°F condition. This, thus, refers to an extraction ratio of unity. The primary nozzle and polar

observation angle associated with each of the spectra are shown in the bottom left for reference. The black curves are representative of jet noise spectra taken from use of the shorter L_e/D_e = 1.0 mixing-duct length while the blue curves correspond to use of the longer, L_e/D_e = 3.0 mixing-duct length. Figure 70 shows a slight increase in noise at higher frequencies when using the AXI which is possibly representative of increased internal mixing. However, Figure 71 and Figure 72 show that this increase is not present when using the forced mixers SUN and DAISY. Previously it was observed that use of the SUN mixer nozzle reduced the overall noise level across all polar observation angles relative to the AXI baseline nozzle while the DAISY mixer produced approximately equal levels of overall noise at sideline and upstream polar angles due to the excess high-frequency noise resulting from enhanced mixing. However, through use of the longer mixing-duct length, both forced mixers decrease overall noise at all polar observation angles relative to the baseline core nozzle, an example of which is included below in Figure 73.

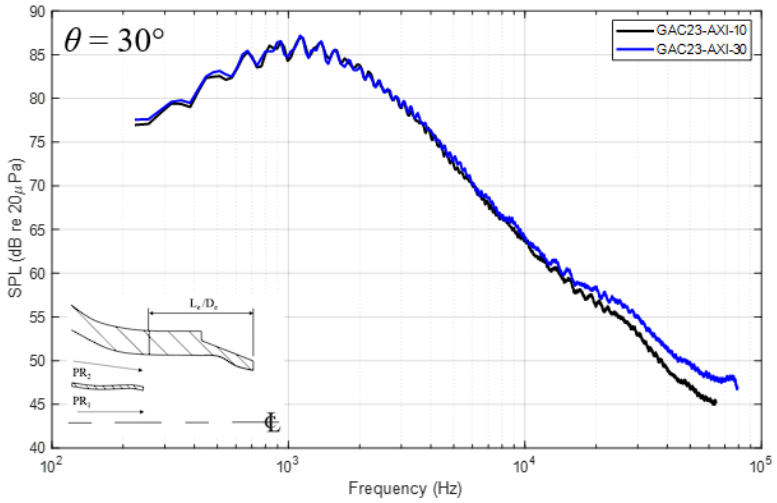

(a)

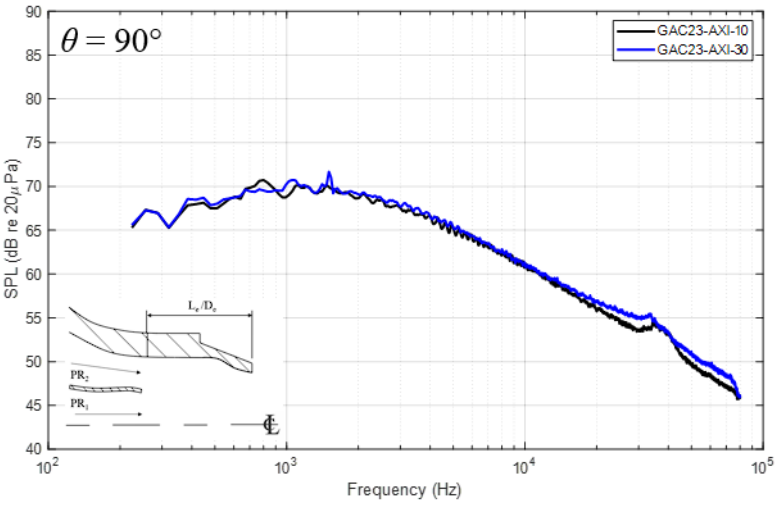

(b)

Figure 70. Effect of mixing-duct length on noise from an internally mixed, dual-stream jet with AXI mixer. FAA GAC Project Model, D_e = 2.20 in. PR_1 = 1.39 (M_{j1} = 0.70), PR_2 = 1.39 (M_{j2} = 0.70), T_{t1} = 500°F, R = 12 ft, θ = a) 30° and b) 90°, Δf = 32 Hz, lossless. SPL: sound pressure level.

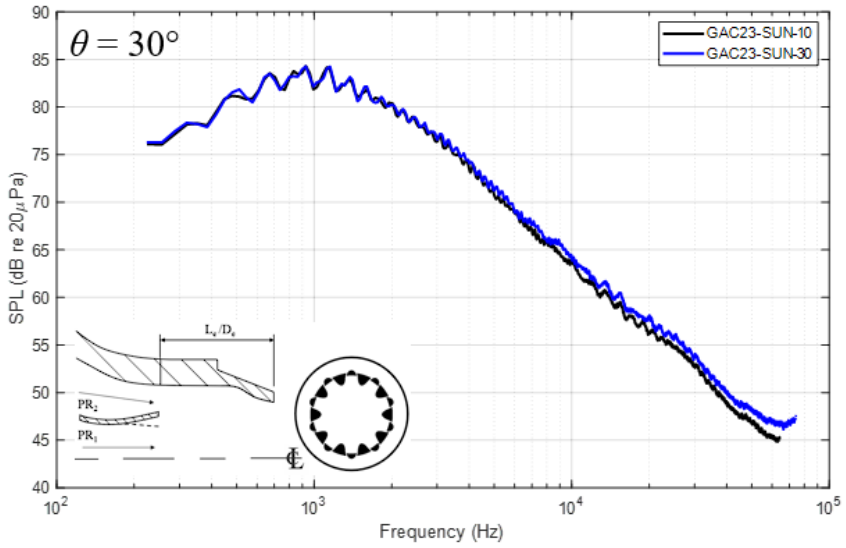

(a)

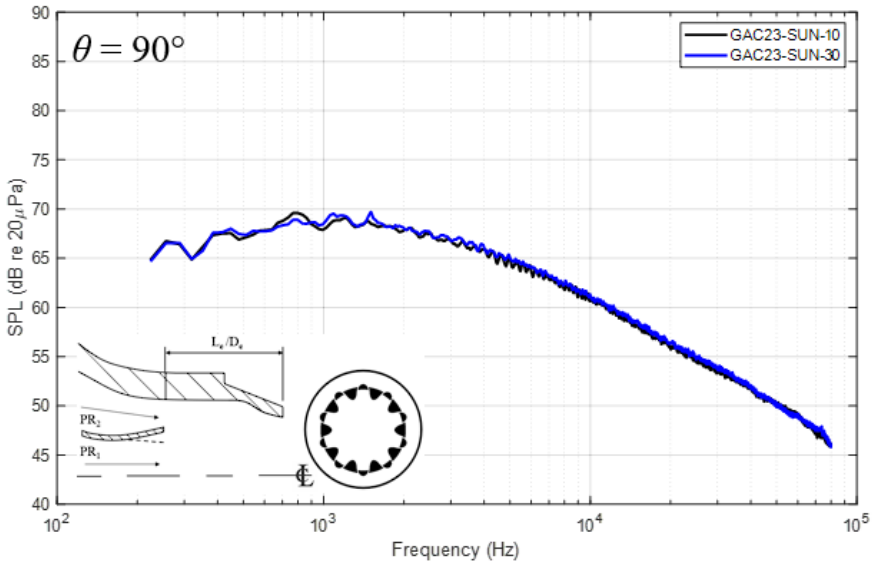

(b)

Figure 71. Effect of mixing-duct length on noise from an internally mixed, dual-stream jet with SUN mixer. FAA GAC Project Model, D_e = 2.20 in. PR_1 = 1.39 (M_{j1} = 0.70), PR_2 = 1.39 (M_{j2} = 0.70), T_{t1} = 500°F, R = 12 ft, θ = a) 30° and b) 90°, Δf = 32 Hz, lossless. SPL: sound pressure level.

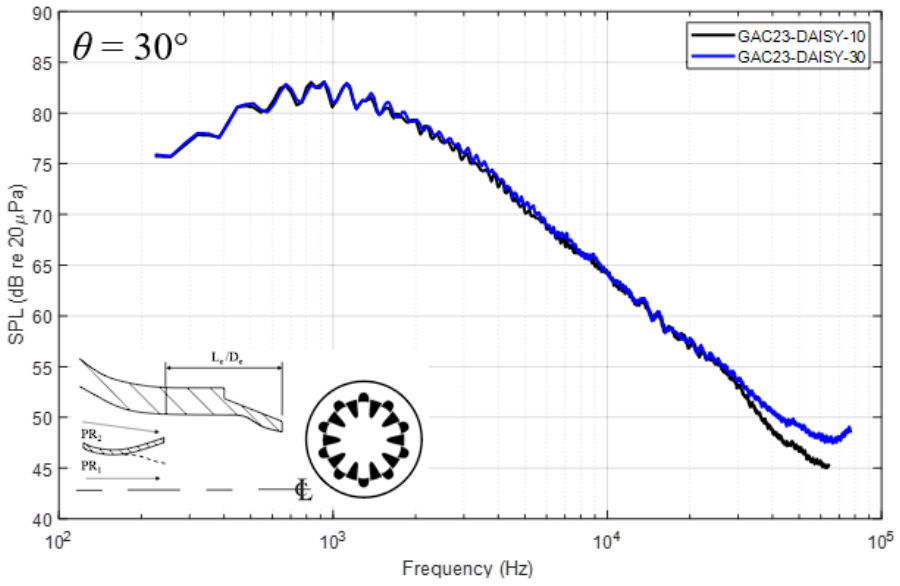

(a)

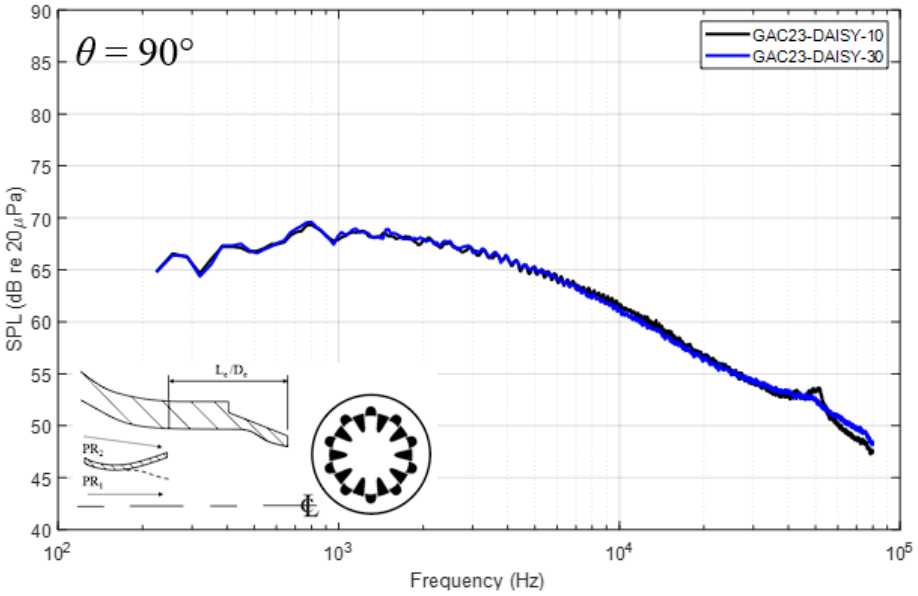

(b)

Figure 72. Effect of mixing-duct length on noise from an internally mixed, dual-stream jet with DAISY mixer. FAA GAC Project Model, D_e = 2.20 in. PR_1 = 1.39 (M_{j1} = 0.70), PR_2 = 1.39 (M_{j2} = 0.70), T_{t1} = 500°F, R = 12 ft, θ = a) 30° and b) 90°, Δf = 32 Hz, lossless. SPL: sound pressure level.

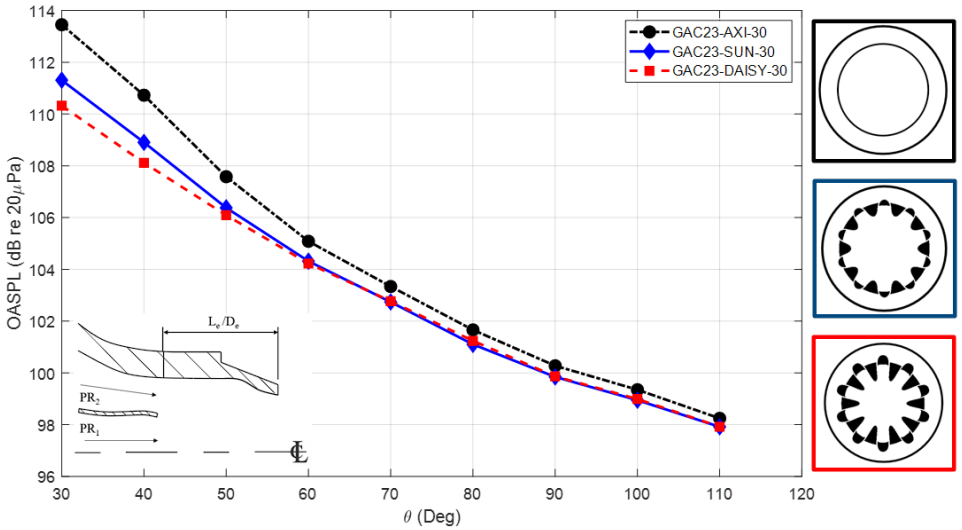

Figure 73. Effect of mixer nozzle on overall noise from an internally mixed, dual-stream jet. FAA GAC Project Model, D_e = 2.20 in. PR_1 = 1.69 (M_{j1} = 0.90), PR_2 = 1.69 (M_{j2} = 0.90), T_{t1} = 500°F, R = 12 ft, Δf = 32 Hz, lossless. SPL: sound pressure level.

PIV Measurements

Due to the intensely time-consuming process that goes into acquiring quality PIV data and large number of nozzle configurations, only a limited batch of dual stream PIV data were acquired with the most important conditions prioritized. High-resolution (i.e., N = 750 samples in order to properly resolve turbulence statistics) PIV measurements were taken for the GAC23-AXI-10 and GAC23-DAISY-10 configurations at each of the following operating conditions with both unheated and heated (T_{t1} = 500°F) core streams:

- PR_1 = 1.39 (M_{j1} = 0.70), PR_2 = 1.39 (M_{j2} = 0.70)
- PR_1 = 1.39 (M_{j1} = 0.70), ER = 1.07
- PR_1 = 1.69 (M_{j1} = 0.90), PR_2 = 1.69 (M_{j2} = 0.90)
- PR_1 = 1.69 (M_{j1} = 0.70), ER = 1.07

PIV data at some of these conditions has been collected for the GAC23-SUN-10 configuration. This data will continue to be taken independently in service of PhD student Larisch's individual research and may be revisited and supplied to modelers at a later date. Again, as there is little-to-no internal mixing was observed for an unheated core stream, only the results for the heated core stream will be presented and discussed. Shown below are various results taken from PIV measurements made of the GAC23-AXI-10 configuration at the PR_1 = 1.69 (M_{j1} = 0.90), PR_2 = 1.69 (M_{j2} = 0.90), T_{t1} = 500°F operating condition. Figure 74 shows the familiar 2D plots of mean axial velocity, axial turbulence intensity, and radial turbulence intensity. Note the much more visible bypass stream visible in the mean axial velocity plot as compared to the previous Year-1 academic nozzle (see Figure 27). One key difference between the Gulfstream models and the previous models is the heightened bypass ratio. This makes visualizations of the bypass stream in comparison to the core stream much easier, especially in schlieren visualizations which will be reviewed in the coming sections. Figure 75 shows profiles of axial velocity and turbulence intensities at various axial locations downstream from the final nozzle exit. Figure 76 shows centerline velocity and turbulence intensity distributions. These results are quite similar to those obtained for the Year-1 nozzle shown in Figure 28 and Figure 29.

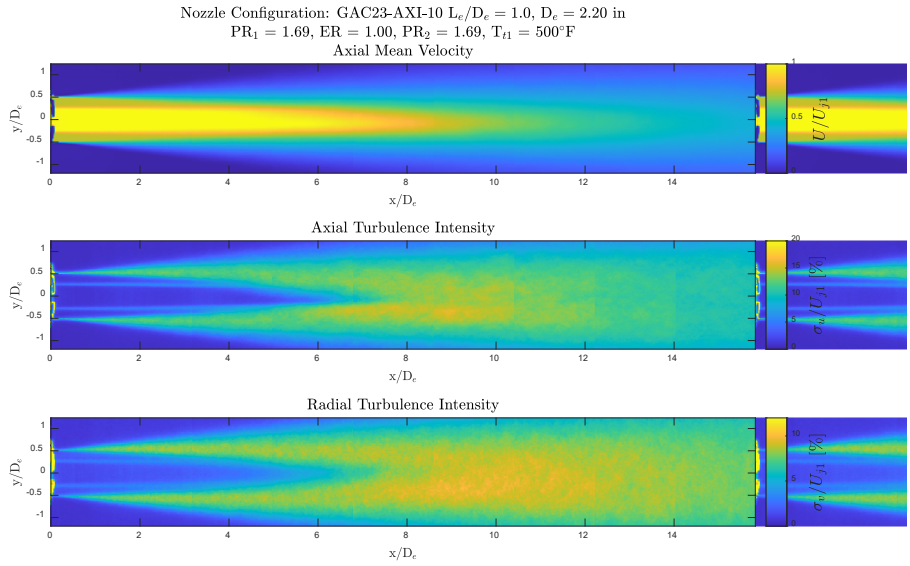

Figure 74. Two-dimensional mean and turbulence intensity plots. GAC23-AXI-10 configuration. PR_1 = 1.69, PR_2 = 1.69, T_{t1} = 500°F, L_e/D_e = 1.0, N = 750 image pairs.

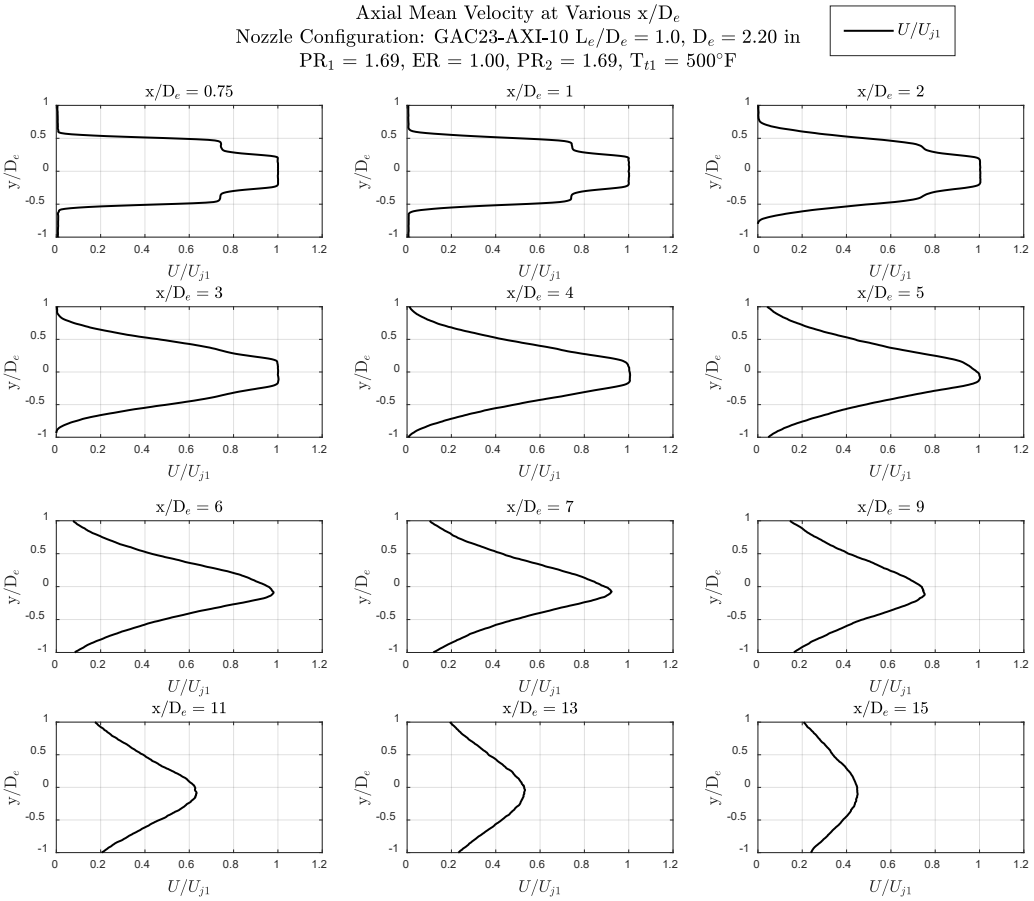
Axial Mean Velocity at Various x/D$_e$
Nozzle Configuration: GAC23-AXI-10 L$_e$/D$_e$ = 1.0, D$_e$ = 2.20 in
PR$_1$ = 1.69, ER = 1.00, PR$_2$ = 1.69, T$_{t1}$ = 500°F
U/U_{j1}
x/D$_e$ = 0.75
x/D$_e$ = 1
x/D$_e$ = 2
x/D$_e$ = 3
x/D$_e$ = 4
x/D$_e$ = 5
x/D$_e$ = 6
x/D$_e$ = 7
x/D$_e$ = 9
x/D$_e$ = 11
x/D$_e$ = 13
x/D$_e$ = 15
y/D$_e$
U/U_{j1}

(a)

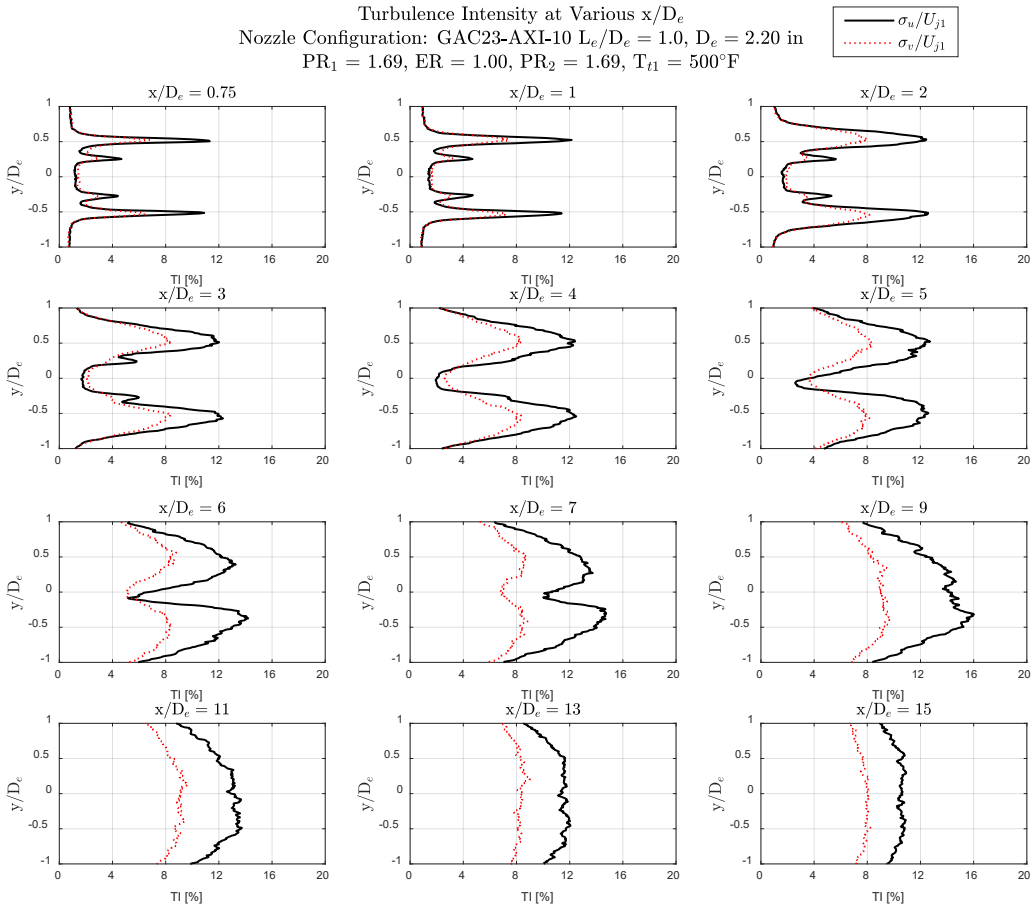

(b)

Figure 75. Profiles of (a) mean axial velocity and (b) turbulence intensities at various x/D$_e$. GAC23-AXI-10 configuration. PR_1 = 1.69, PR_2 = 1.69, T_{t1} = 500°F, L_e/D_e = 1.0, N = 750 image pairs.

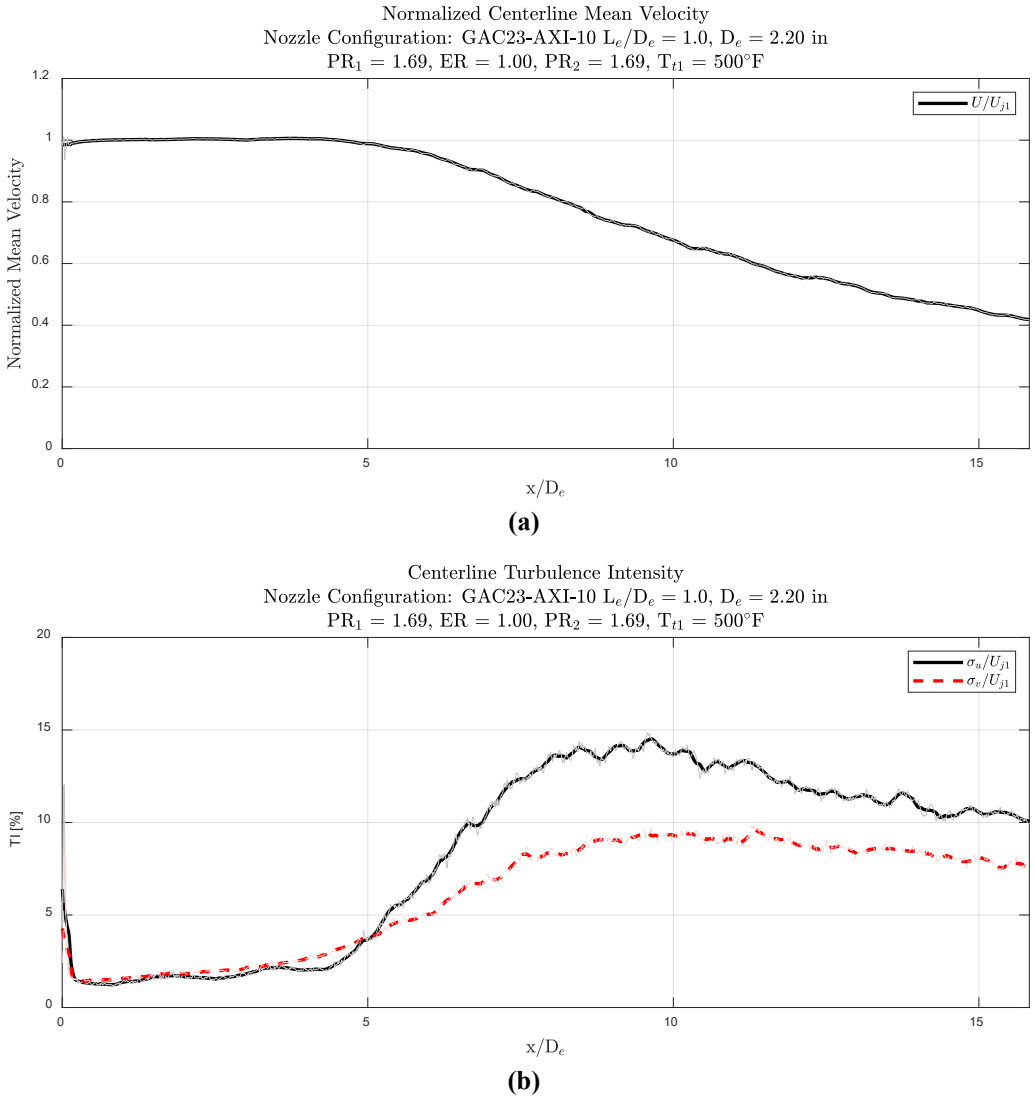

Figure 76. Plots of centerline (a) axial velocity and (b) turbulence intensities (TI). GAC23-AXI-10 configuration. PR_1 = 1.69, PR_2 = 1.69, T_{t1} = 500°F, L_e/D_e = 1.0, N = 750 image pairs.

Below in Figure 77 are 2D plots of mean axial velocity and turbulence intensities at the same operating condition PR_1 = 1.69 (M_{j1} = 0.90), PR_2 = 1.69 (M_{j2} = 0.90), T_{t1} = 500°F with the DAISY internal lobed mixer (i.e., the GAC23-DAISY-10 configuration). Although the lobed nozzle is now buried within the secondary duct, it is still important to note that the laser sheet is aligned vertically with lobes (e.g., as in Figure 58a). Because of this, one can observe bright streaks of partially-mixed core flow just downstream from the nozzle exit near y/D_e = ±0.4 in the axial velocity plot. The width of the remaining core jet is visibly much smaller than that from the GAC23-AXI-10 configuration shown in Figure 74 and the potential core seems to terminate quicker. Indeed, comparing the centerline velocity distributions between the two configurations shown in Figure 78, one can see an approximate 50% reduction in potential core length compared to the axisymmetric baseline.

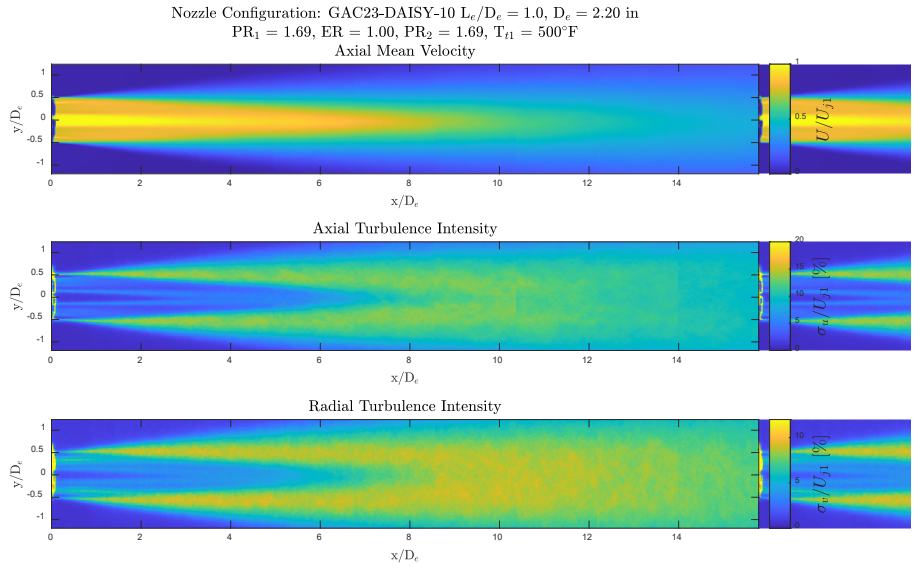

Figure 77. Two-dimensional mean and turbulence intensity plots. GAC23-AXI-10 configuration. PR_1 = 1.69, PR_2 = 1.69, T_{t1} = 500°F, L_e/D_e = 1.0, N = 750 image pairs.

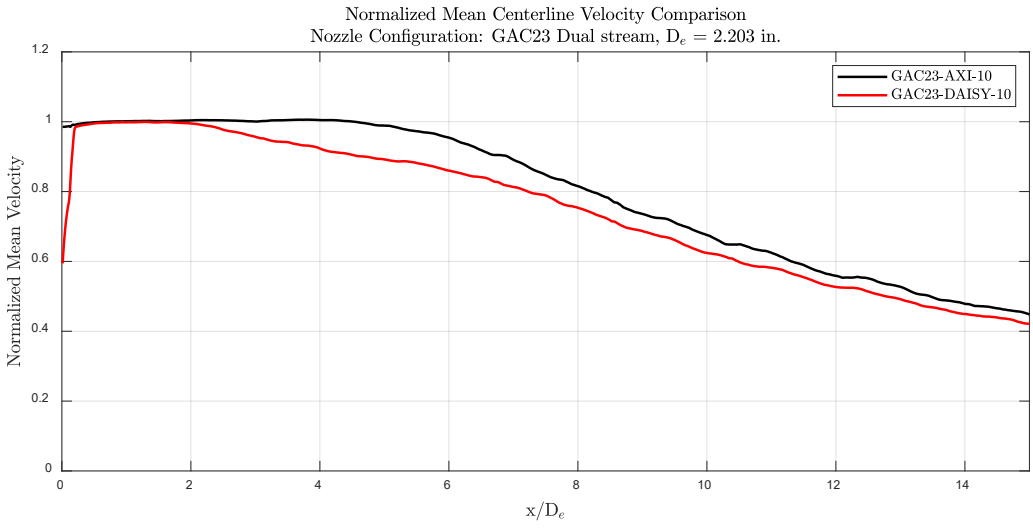

Figure 78. Comparison of centerline axial velocity distribution. GAC23-AXI-10 (black) and GAC23-DAISY-10 (red) configurations. PR_1 = 1.69, PR_2 = 1.69, T_{t1} = 500°F, L_e/D_e = 1.0, N = 750 image pairs.

To show a more direct comparison of the flowfields between the two configurations, mean velocity profiles at various axial stations for both the GAC23-AXI-10 and GAC23-DAISY-10 configurations are overlaid and shown in Figure 79.

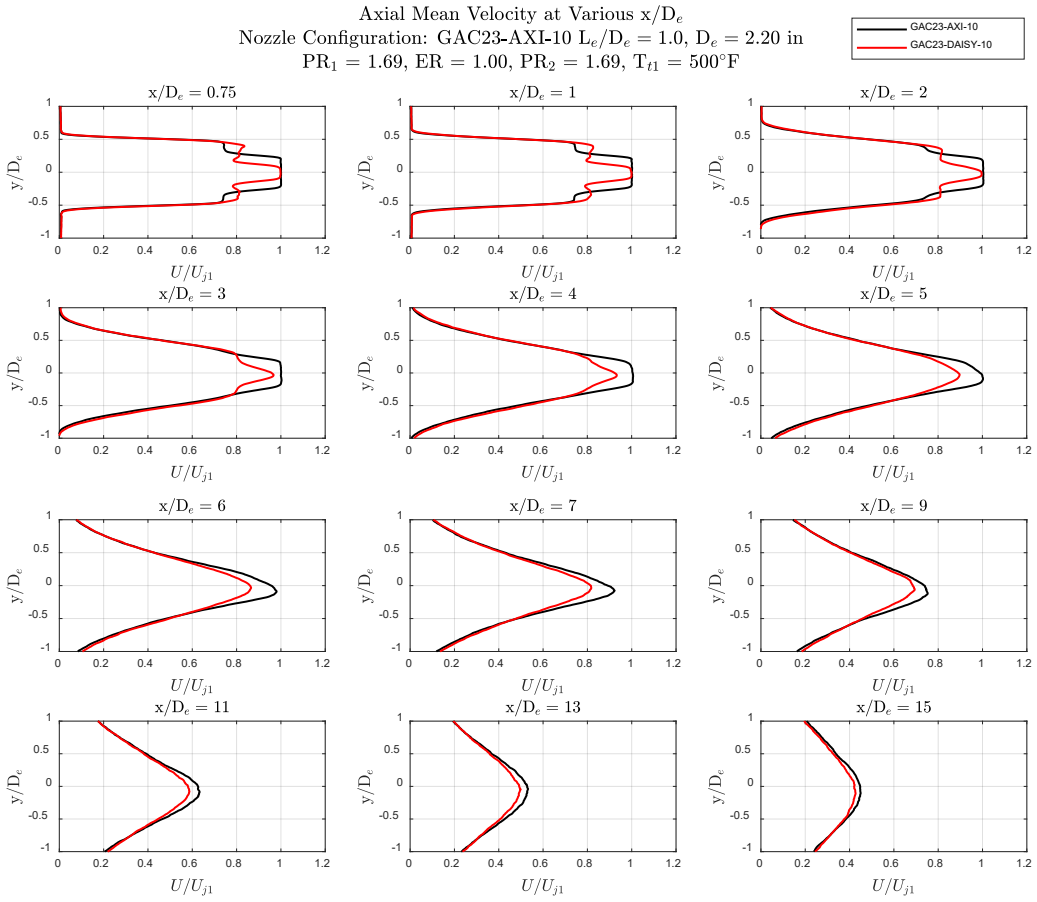

Figure 79. Profiles of mean axial velocity at various x/D_e. GAC23-AXI-10 (black) and GAC23-DAISY-10 (red) configurations. PR_1 = 1.69, PR_2 = 1.69, T_{t1} = 500°F, L_e/D_e = 1.0, N = 750 image pairs.

Schlieren Visualizations

High-speed schlieren flow visualizations were acquired simultaneously alongside acoustic source location measurements using the Z-type schlieren system in the GTRI Flow Diagnostics Facility at the set of heated core operated conditions shown in the matrix in Figure 65b. Schlieren and source location data was only acquired for heated core conditions due to the lack off effect by the lobed internal mixers on the farfield noise of the unheated jet. If it is desired, these unheated conditions could be revisited at a later date as part of extended work. All representative images shown visualize transverse density gradients in the flow ($\partial\rho/\partial y$). Time-resolved schlieren visualizations were captured at a rate of f_s = 51,000 frames per second. The qualitative results of these dynamic measurements are difficult to capture through single still images and as such sample results are included here with little discussion. Short, 200 frame videos will be made available to modeling teams with longer, 2,500-frame videos available upon request.

The set of images in Figure 80 show the effects of each primary nozzle cap (AXI, SUN, DAISY read from left to right) on the flow from a dual-stream jet operated at M_{j1} = 0.70, M_{j2} = 0.70, T_{t1} = 500°F with a common mixing-duct length of L_e/D_e = 1.0. The digits at the end of the nozzle configuration name above each image denote the mixing-duct length in tenths of L_e/D_e and are highlighted in red to assist in differentiating the figure from Figure 81 which shows the same results but for the longer mixing-duct length of L_e/D_e = 3.0. Orderly wave-like structures are still apparent in the flow downstream from the initial mixing region. These structures are somewhat visible in the right half of each image included in Figure 80, yet are much more easily discernible in the complete, time-resolved visualizations. Future experimental work may involve

attempting to reduce the presence of this instability by disrupting the boundary layers present on and inside the core nozzle – including when operating with the lobed mixers.

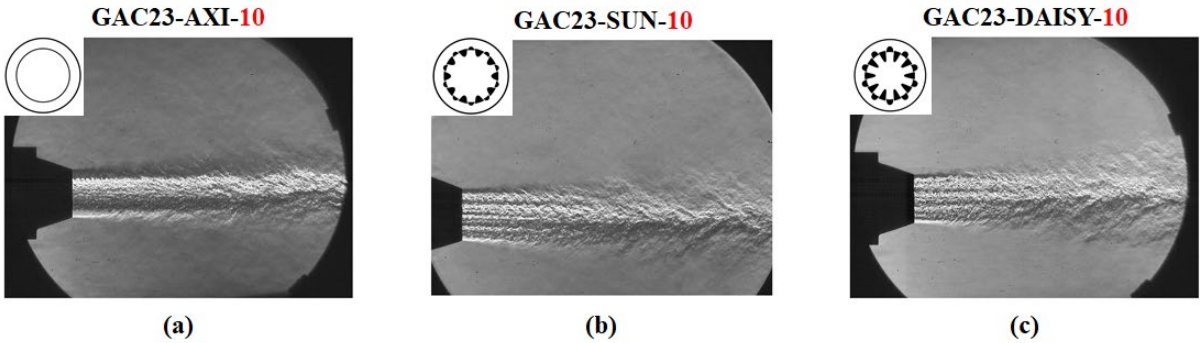

Figure 80. Instantaneous schlieren flow visualizations of dual-stream jet utilizing (a) AXI, (b) SUN, and (c) DAISY internal mixers. M_{j1} = 0.70, M_{j2} = 0.70, T_{t1} = 500°F. L_e/D_e = 1.0, D_e = 2.20 in. Sample rate f_s = 51,000 fps, 1.5 µs exposure.

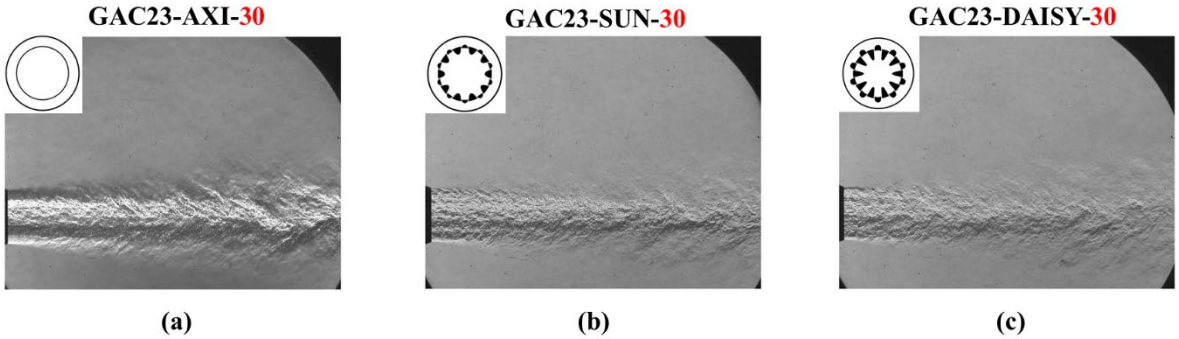

Figure 81. Instantaneous schlieren flow visualizations of dual-stream jet utilizing (a) AXI, (b) SUN, and (c) DAISY internal mixers. M_{j1} = 0.70, M_{j2} = 0.70, T_{t1} = 500°F. L_e/D_e = 3.0, D_e = 2.20 in. Sample rate f_s = 51,000 fps, 1.5 µs exposure.

Source Location Analysis

The effects of the different internal mixers on the distribution of noise sources of the dual stream are discussed first. Unless otherwise indicated, all source location data shown correspond to the location of peak noise for a given frequency; this is in contrast to that of some jet noise source location literature, which reports the centroid location of each frequency instead (Breen & Ahuja, 2020). Figure 82 and Figure 83 below show the effects of the lobed mixer nozzles on the source distribution of an internally-mixed, heated-core jet with a common mixing-duct length of L_e/D_e = 1.0 operated at an extraction ratio ER of unity. The origin of the x-axis is taken to be the exit of the final, exhaust nozzle. For reference, an empirical source distribution for a theoretically fully-mixed jet, with exit velocity U_{mix} (obtained using isentropic relations and enthalpy conservation) and diameter D_e, is provided as a dotted curve. The Strouhal number distribution for this reference curve is converted to frequency using the scale factor U_{mix}/D_e. The authors of this report decided against collapsing the measured data using a similar method as the proper characteristic length and velocity scales for these partially-mixed jets are not known. As such the source location data are displayed without normalization of the frequency axis. As observed in Figure 82 and Figure 83, there is a slight upstream shift in the distribution of higher-frequency noise sources (e.g., in Figure 82 greater than about 4 kHz) going from the axisymmetric internal mixer to each of the lobed mixers. Generally, the peak noise source distribution when using the AXI mixer (denoted in Figure 82 and Figure 83 as data markers with blue circles) is divided among two distinct regions. As the mixing of the dual-stream jet is enhanced through use of the lobed nozzles, the peak source location appears to follow a more uniform distribution. When comparing the two extremes – data taken from the AXI internal mixer in blue circles versus those of the DAISY mixer in red squares – the shape of the distribution when using the DAISY mixer approaches that of the empirical curve. The results are similar for both M_{j1} = 0.70, M_{j2} = 0.70, T_{t1} = 500°F (see Figure 82) and M_{j1} = 0.90, M_{j2} = 0.90, T_{t1} = 500°F (see Figure 83).

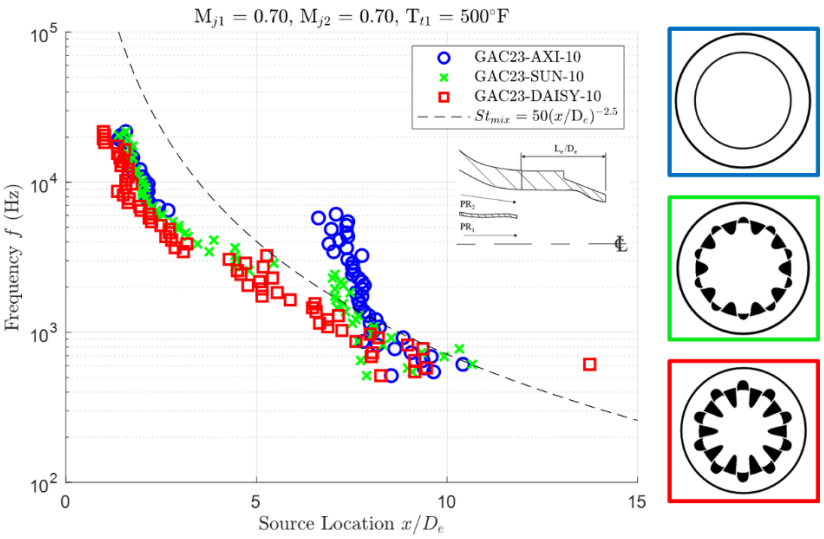

Figure 82. Effect of forced mixers on source location of dual-stream jet. L_e/D_e = 1.0, D_e = 2.20 in. M_{j1} = 0.70, M_{j2} = 0.70, T_{t1} = 500°F, one-twelfth octave.

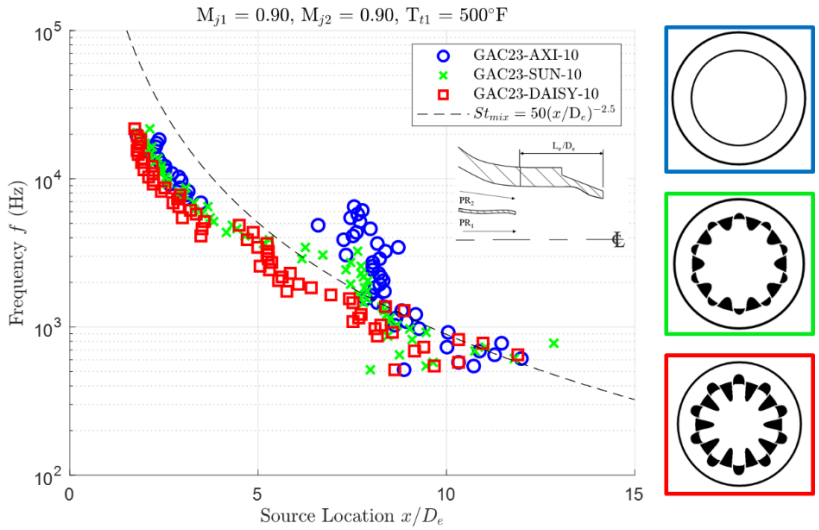

Figure 83. Effect of forced mixers on source location of dual-stream jet. L_e/D_e = 1.0, D_e = 2.20 in. M_{j1} = 0.90, M_{j2} = 0.90, T_{t1} = 500°F, one-twelfth octave.

Similar to Figure 82 and Figure 83, Figure 84 and Figure 85 show the effects of the internal mixers on the source distribution of the dual-stream jet but now with the longer mixing-duct length of L_e/D_e = 3.0. Once again, the dashed curve included in each figure represents the empirical source distribution of a fully-mixed jet. Unlike the shorter mixing-duct length data for L_e/D_e = 1.0 shown in Figure 82 and Figure 83, wherein use of the more aggressive DAISY mixer over the relatively mild SUN mixer yielded a slight upstream shift in the distribution of higher-frequency sources, Figure 84 and Figure 85 show next to no difference in the source distribution between configurations using the SUN versus DAISY internal mixers. The two distinct source location regions that occur for the AXI mixer for the L_e/D_e = 1.0 mixing-duct

lengths still occur for L_e/D_e = 3.0. For both mixing duct lengths, a cluster of many noise sources of frequencies in the range of 1000 – 7000 Hz seems to originate from a distance, x, of about $7D_e$ to $8D_e$. This effect is most prominent for the asymmetrical nozzle and appears to be located just downstream of the potential core of the final nozzle, which is typically about 6 diameters long. The extent of this effect reduces as additional mixing is introduced. For the SUN mixer, this effect is still present, although to a lesser extent. This effect is not as prominent for the DAISY mixer, which is expected to provide the most mixing. The precise reason for this clustering of sources still needs to be understood.

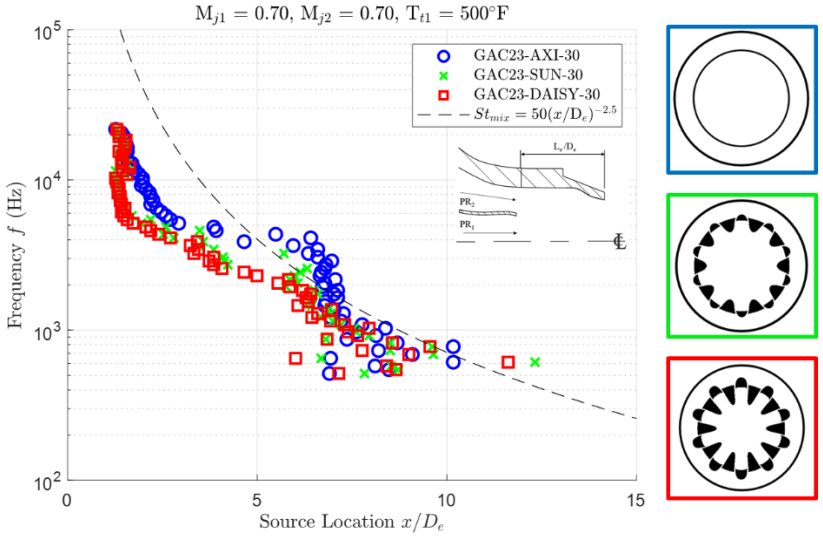

Figure 84. Effect of forced mixers on source location of dual-stream jet. L_e/D_e = 3.0, D_e = 2.20 in. M_{j1} = 0.70, M_{j2} = 0.70, T_{t1} = 500°F, one-twelfth octave.

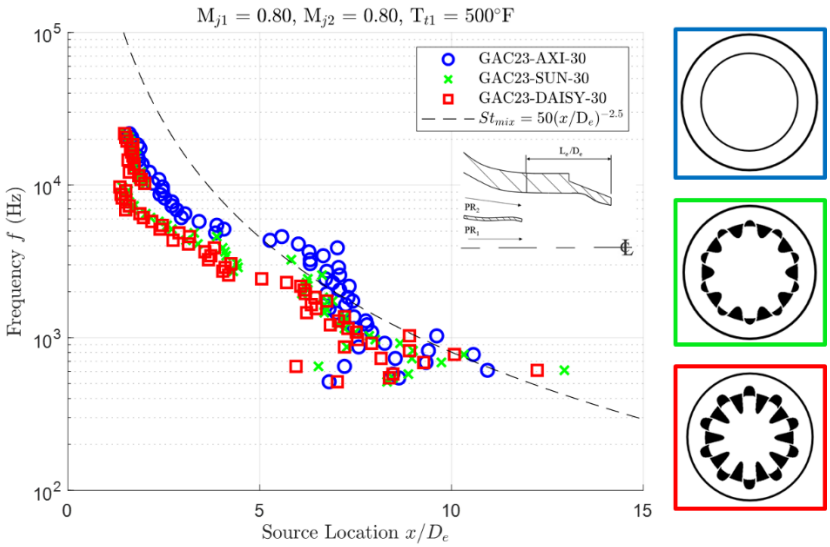

Figure 85. Effect of forced mixers on source location of dual-stream jet. L_e/D_e = 3.0, D_e = 2.20 in. M_{j1} = 0.80, M_{j2} = 0.80, T_{t1} = 500°F, one-twelfth octave.

Previously reported farfield acoustic data showed that increasing the mixing-duct length from L_e/D_e = 1.0 to 3.0 had little to no effect on the jet noise measured using the SUN and DAISY internal mixers. Similarly, this same increase in mixing-duct length has little to no effect on the source distribution of dual-stream jets using the SUN and DAISY internal mixers; however, there is a noticeable effect when using the axisymmetric baseline core nozzle. Figure 86 compares the peak noise source distribution between the two mixing-duct lengths for each of the three mixers. When using the SUN mixer (Figure 86b) there is a slight upstream movement in source distribution which is most apparent at mid-range (about 1 to 9 kHz) frequencies when comparing the shortest and longest mixing-duct lengths. This trend is not observable for the DAISY mixer (Figure 86c) where the data lay nearly on top of one another. This is not to say that the mixing-duct length of an internally-mixed jet using lobed mixers is a nonfactor. Rather, the nozzle length can have considerable effects on farfield noise measurements given the potentially substantial levels of mixing noise introduced by lobed internal mixers (see Mengle et al. [1997], Mengle [1999, 2000]). Future tests involving additional mixing-duct lengths and mixer designs may yield more thought-provoking results. When utilizing the baseline AXI mixer, increasing the mixing-duct length did have a consistent, observable effect on the source distribution.

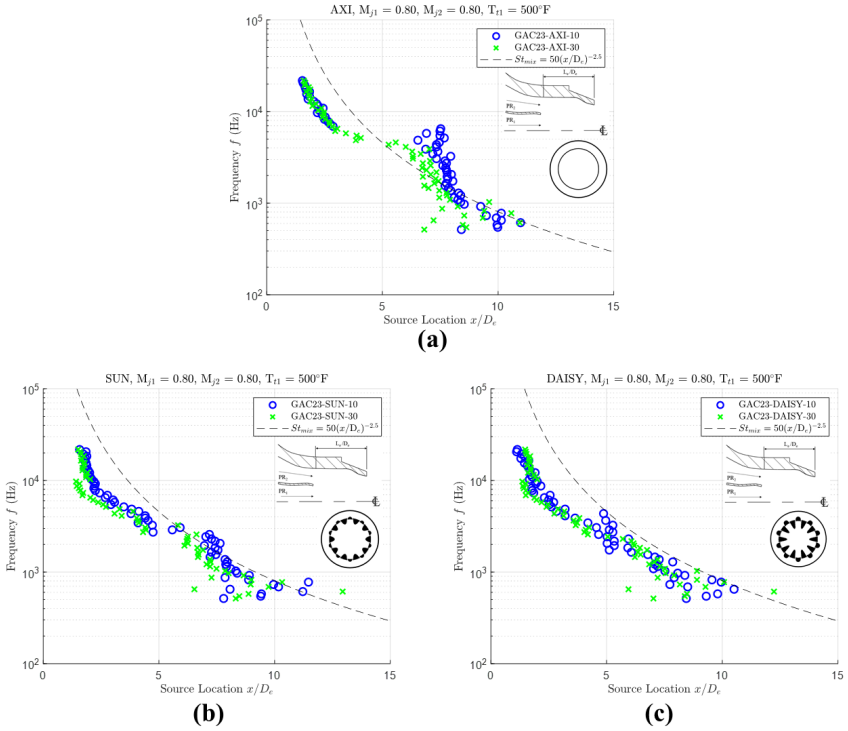

Figure 86. Effect of mixing-duct length on source location of dual-stream jet using (a) AXI (b) SUN and (c) DAISY internal mixers. D_e = 2.20 in. M_{j1} = 0.80, M_{j2} = 0.80, T_{t1} = 500°F, one-twelfth octave. (Blue circles: L_e/D_e = 1.0, Green crosses: L_e/D_e =3.0).

Increasing from the shortest to longest mixing-duct length has the most prominent effect on peak source distribution when using the axisymmetric internal mixer (Figure 86a) in which there is a substantial shift in the location of low-to-mid frequency noise sources toward the nozzle exit. In order to develop empirical relations for the source distribution of an internally-mixed, dual-stream jet, some initial attempts have been made to collapse the source location data across various operating conditions for a given nozzle geometry. Figure 87 shows the complete set of source location data for both GAC23-AXI-10 and GAC23-AXI-30 configurations collapsed using a Strouhal number based on the core-jet exit velocity U_{j1} and the exhaust nozzle exit diameter D_e – a normalization which had been shown in a past report to collapse the data from the GAC23-AXI-10 configuration reasonably well. We observe that the higher frequency content in the region close to the nozzle exit (x/D_e < 6) behaves generally the same between mixing-duct lengths, while the lower frequencies farther

downstream ($x/D_e > 6$) have shifted approximately one diameter upstream relative to the shorter mixing-duct length configuration.

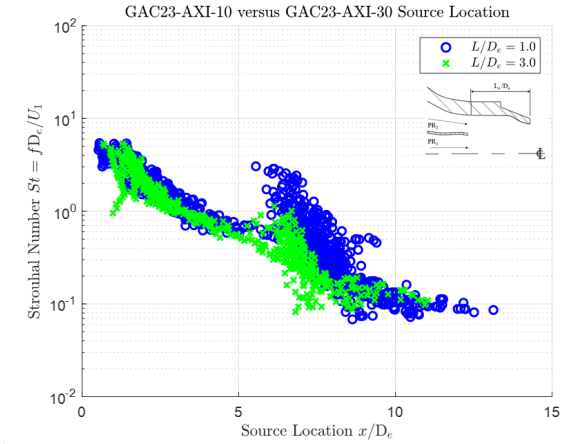

Figure 87. Effect of mixing-duct length on source location of dual-stream jet using AXI internal mixers. D_e = 2.20 in. Various M_{j1} and M_{j2}, T_{t1} = 500°F, one-twelfth octave.

Conclusions

The primary goal of the project was to conduct cost-effective SST jet noise experiments to support the development of low-, medium-, and high-fidelity jet noise prediction methods. This effort involved designing the experimental approach in collaboration with industry partners and federal agencies—including NASA, DOD, FAA, and FAA-funded modelers—to reduce uncertainty and inform the design of quieter supersonic jet engines. Working with GAC, Georgia Tech identified a representative baseline nozzle configuration for testing. The resulting dataset included far-field noise measurements, high-speed flow visualization, source localization, and detailed mean and unsteady flow measurements. GAC provided model-scale lobed mixer nozzles for testing unheated and heated flows at the same facility.

The experimental data from Georgia Tech was disseminated to key stakeholders and computational teams funded by FAA, validating semi-empirical and computational jet noise predictions.

Data were collected for both nozzles under various operating conditions and extraction ratios, including acoustic spectra, flow data, PIV, flow visualization, and acoustic source locations. This data was provided to aeroacoustics modelers for further analysis and model development.

Baseline Nozzle

- A substantial amount of far-field jet noise, PIV, schlieren, and source location data for various nozzle configurations was collected and analyzed.
- The experiments examined the effects of mixing-duct length, extraction ratio, and core temperature on noise and flow of jets from low-bypass annular confluent nozzle.
- For unheated jets, increased extraction ratio raised noise due to heightened bypass stream velocity.
- Short mixing-duct lengths produced this increase at higher frequencies.
- Long mixing-duct lengths distributed this increase across frequencies.
- Confluent nozzles experienced intense howling due to:
  - Impingement of the core-jet shear layer on the final nozzle exit when PR1 is greater than PR2.
  - Feedback loop created by periodic shock-induced boundary layer separation near the final nozzle exit at high subsonic secondary pressure ratios.
- Mitigation of howling was achievable with appropriate boundary layer trips.
- Mixing-duct length had minimal effect on far-field noise; however, dual-stream, heated-core confluent jets showed an upstream shift in low-frequency noise source distributions and a shortening of the potential core.

Forced Mixer Nozzle

- Lobed internal mixer nozzles had little impact on the far-field noise of unheated confluent jets.
- For unheated core streams and near-unity extraction ratios, minimal mixing was observed, resulting in little acoustic advantage.
- Effects on unheated jets occurred only with unrealistic pressure ratios, involving significant velocity differences between the two streams.
- For heated core streams, lobed internal mixers reduced noise at peak frequencies but increased noise at higher frequencies.
- These reductions were more pronounced closer to the jet axis.
- Increasing lobe penetration further reduced low-frequency noise but increased high-frequency noise.
- Lobed internal mixers decreased OASPL across all observation angles at industry-relevant conditions.
- PIV and schlieren measurements showed that internal mixer nozzles led to a rapid collapse of the jet potential core and thickening of the core-bypass mixing layer.
- Increased lobe penetration resulted in a more uniformly mixed jet at the exit of the mixing duct.
- Noise source distribution from dual-stream jets with lobed mixers resembled that of a theoretically "fully-mixed" jet.

PhD Student Jackson Larisch's Research Funded by This Project

- Investigated the effects of lobed nozzles on subsonic jet noise.
- Focused on lobed jets without bypass flow to isolate features of the lobed core flow.
- The highly vortical flow downstream from the lobed nozzle exit formed small 'jetlets.'
- Collapse of jetlets led to a dense distribution of high-frequency noise sources close to the nozzle exit.
- Jetlets acted as a new source of coherent, high-frequency noise, with a spectral shape similar to the large-scale universal similarity spectrum proposed by Tam et al.
- Reductions in low-frequency jet noise were attributed to the rapid collapse of the lobed jet potential core and shear layer thickening, which stabilized dominant instability waves and altered frequencies and growth rates of large-scale structures

References

Ahuja, K. (2003). Designing clean jet-noise facilities and making accurate jet-noise measurements. *International Journal of Aeroacoustics, 2*(3), 371-412. https://doi.org/10.1260/147547203322986188

Ahuja, K. K., Lepicovsky, J., Tam, C. K. W., Morris, P. J., & Burrin, R. H. (1982). *Tone-Excited Jet: Theory and Experiments* (NASA CR-3538). National Aeronautics and Space Administration. https://ntrs.nasa.gov/citations/19830004698

Breen, N. (2019). *Source Location of Subsonic and Supersonic Jets of Various Geometries via Acoustic Beamforming* [Doctoral dissertation, Georgia Institute of Technology].

Breen, N. P., & Ahuja, K. K. (2019, January). *Subsonic jet noise source location as a function of nozzle geometry* (AIAA 2019-0250). AIAA SciTech 2019 Forum. https://doi.org/10.2514/6.2019-0250

Breen, N. P., & Ahuja, K. K. (2020, June). *Limitations of acoustic beamforming for accurate jet noise source location* (AIAA 2020-2603). AIAA AVIATION 2020 FORUM. https://doi.org/10.2514/6.2020-2603

Bridges, J., & Wernet, M. P. (2011). *The NASA subsonic jet particle image velocimetry (PIV) dataset* (NASA TM-2011-216807). National Aeronautics and Space Administration. https://ntrs.nasa.gov/citations/20110023688

Burrin, R. H., Dean, P. D., & Tanna, H. K. (1974). A new anechoic facility for supersonic hot jet noise research at Lockheed-Georgia. *The Journal of the Acoustical Society of America, 55*(2), 400. https://doi.org/10.1121/1.3437223

Burrin, R., & Tanna, H. (1979). The Lockheed-Georgia coannular jet research facility. *The Journal of the Acoustical Society of America, 65*(S1), S44-S44. https://doi.org/10.1121/1.2017259

Christensen, K. T. (2004). The influence of peak-locking errors on turbulence statistics computed from PIV ensembles. *Experiments in Fluids, 36*(3), 484-497. https://doi.org/10.1007/s00348-003-0754-2

Chung, J. Y. (1977). Rejection of flow noise using a coherence function method. *Journal of the Acoustical Society of America*, 62(2), 388, 395. https://doi.org/10.1121/1.381537

Clemens, A. J., & Gavin, J. R. (2024). ASCENT 59: Aerodynamic Design of Nozzles and Mixers. *AIAA AVIATION Forum and ASCEND 2024*.

Karon, A. Z., & Ahuja, K. K. (2016). *Potential factors responsible for discrepancies in jet noise measurements of different studies* [Doctoral dissertation, Georgia Institute of Technology].

Mengle, V. (1999, May). Anomalous effect of nozzle length reduction on jet noise of forced mixers (AIAA 1999-1968). *5th AIAA/CEAS Aeroacoustics Conference and Exhibit*. https://doi.org/10.2514/6.1999-1968

Mengle, V. (2000, June). Optimization of lobe mixer geometry and nozzle length for minimum jet noise (AIAA 2000-1963). *6th Aeroacoustics Conference and Exhibit*. https://doi.org/10.2514/6.2000-1963

Mengle, V., Dalton, W., Bridges, J., & Boyd, K. (1997, May). Noise reduction with lobed mixers - Nozzle-length and free-jet speed effects (AIAA 1997-1682). *3rd AIAA/CEAS Aeroacoustics Conference*. https://doi.org/10.2514/6.1997-1682

Morris, P. J., & Zaman, K. B. M. Q. Z. (2010). Velocity Measurements in Jets with Application to Noise Source Modeling. *Journal of Sound and Vibration, 329*(4), 394 – 414. https://doi.org/10.1016/j.jsv.2009.09.024

Nance, D. K. (2007). *Separating contributions of small-scale turbulence, large-scale turbulence, and core noise from far-field exhaust noise measurements* [Doctoral dissertation, Georgia Institute of Technology].

Nance, D. K., & Ahuja, K. K. (2007, January). Limitations of the three-microphone signal enhancement technique," 45th AIAA Aerospace Sciences Meeting and Exhibit (AIAA 2007-441). *45th AIAA Aerospace Sciences Meeting and Exhibit*. https://doi.org/10.2514/6.2007-441

Nance, D. K., & Ahuja, K. K. (2009, May). Experimentally separating jet noise contribution of large-scale turbulence from that of small-scale turbulence (AIAA 2009-3213). *15th AIAA/CEAS Aeroacoustics Conference (30th AIAA Aeroacoustics Conference)*. https://doi.org/10.2514/6.2009-3213

Pope, S. B. (2000). *Turbulent flows*. Cambridge University Press. https://doi.org/10.1017/CBO9781316179475

Raffel, M., Willert, C. E., & Kompenhans, J. (2018). *Particle Image Velocimetry: A Practical Guide* (3rd Ed.). Springer International Publishing. https://doi.org/10.1007/978-3-319-68852-7

Ramsey, D. N. (2024). *Understanding and Preventing the Howling of a Model-Scale Internally Mixed Jet* [Doctoral dissertation, Georgia Institute of Technology]

Ramsey, D. N., Mayo, R., & Ahuja, K. (2023a, June). Howling in a Model-Scale Internally Mixed Confluent Nozzle Related to Excited Core-Jet Instability (AIAA 2023-3932). *AIAA AVIATION 2023 Forum*. https://doi.org/10.2514/6.2023-3932

Ramsey, D. N., Ahuja, K., & Gavin, J. (2023b, June). Howling in a Model-Scale Nozzle Related to Shock-Induced Boundary-Layer Separation at the Nozzle Exit (AIAA 2023-3933). *AIAA AVIATION 2023 Forum*. https://doi.org/10.2514/6.2023-3933

Ramsey, D. N., Karon, A. Z., Funk, R., & Ahuja, K. K. (2022a). Noise from Low-Bypass Confluent Nozzles: Mixing Length, Extraction Ratio, and Core Temperature Effects. *28th AIAA/CEAS Aeroacoustics 2022 Conference*.

Ramsey, D. N., Karon, A. Z., Funk, R., & Ahuja, K. K. (2022b). Self-Excited Jet from a Low-Bypass Confluent Nozzle at Unity Extraction Ratio. *28th AIAA/CEAS Aeroacoustics 2022 Conference*. https://doi.org/10.2514/6.2022-2864

Tam, C. K. W. (2019). A phenomenological approach to jet noise: The two-source model. *Philosophical Transactions of the Royal Society A: Mathematical, Physical and Engineering Sciences, 377*(2159). https://doi.org/10.1098/rsta.2019.0078

Tam, C. K. W., Golebiowski, M., & Seiner, J. M. (1996). On the two components of turbulent mixing noise from supersonic jets. *Proceedings of the 2nd AIAA/CEAS Aeroacoustics Conference*. https://doi.org/10.2514/6.1996-1716

Tam, C. K. W., Viswanathan, K., Ahuja, K. K., & Panda, J. (2008). The sources of jet noise: Experimental evidence. *Journal of Fluid Mechanics, 615*, 253 – 292. https://doi.org/10.1017/S0022112008003704

Witze, P. O. (1974). Centerline Velocity Decay of Compressible Free Jets. *AIAA Journal, 12*(4), 417 – 418. https://doi.org/10.2514/3.49262